Mesoscopic and continuous photoresist development simulation

von Diplom-Physiker Alexander Philippou aus Hamburg

der Fakultät II - Mathematik und Naturwissenschaften der Technischen Universität Berlin zur Erlangung des akademischen Grades

Doktor der Naturwissenschaften, Doctor rerum naturalium

genehmigte Dissertation

Promotionsausschuss:

Vorsitzender:	Prof. Dr. M. Kneissl
Berichter/Gutachter:	Prof. Dr. E. Schöll, Ph.D.
Berichter/Gutachter:	Prof. Dr. T. Brandes

Tag der wissenschaftlichen Aussprache: 19.12.2007

Berlin 2008
D 83

Sperrvermerk:

Diese Arbeit ist bis zum 1.12.2008 gesperrt. In dieser Zeit ist die Veröffentlichung, Vervielfältigung und Weitergabe der vorliegenden Arbeit oder der darin enthaltenen Informationen nur mit ausdrücklicher Genehmigung der Qimonda Dresden GmbH & Co. OHG gestattet. Die inhaltlichen Ergebnisse der Arbeit können jedoch ohne Einschränkung für Tätigkeiten der Lehre und Forschung an der Technischen Universität Berlin verwendet werden, sofern kein Bezug zur Qimonda Dresden GmbH & Co. OHG hergestellt wird. Nach Ablauf der Sperrfrist entfallen alle Auflagen.

Contents

Abstract

Optical lithography has been the standard technique for decades in semiconductor industry to print chip layouts onto the wafer. While the lithography process is under continuous improvement the increasing complexity by shrinking feature sizes require the development of sophisticated simulators. With this simulation software it is possible to predict the printing of different layouts and thereby reduce the number of experiments necessary for introducing the next chip generation. In simulation, the limitations of lithography can be related to two major research fields. The first is based on accurate calculation of the aerial image on top of the wafer where illumination settings and source shape, numerical aperture of the lenses, the mask used and the refractive index of the media between mask and wafer must be considered. The second important field is the photoresist simulation which includes the post-exposure bake (PEB) and the development in an aqueous base solution. This work is mainly concerned with the second field.

As part of this work, the roughness effects in photoresists were investigated. Especially for decreasing critical dimensions line edge roughness (LER) increases and seems to be a main problem for future device performance. Therefore a mesoscopic resist simulation software was developed built on an already existing mesoscopic PEB algorithm which combines several effects known to contribute to LER. This software allows for simulation on a mesoscopic scale in the PEB module as well as during the photoresist development where polymer size is taken explicitly into account. With the help of this software a better and more fundamental understanding of roughness formation in resists was possible.

For further verification purposes a front propagation algorithm based on a fast marching approach was developed for simulating the macroscopic resist dissolution. While this algorithm has been known since 1996 it completes an in-house software for macroscopic lithography simulation. The flexibility of the new software leads to a possible new double patterning processes utilizing the reaction-diffusion effects in chemically amplified photoresist where a feasibility study based on simulation is presented for the first time here.

Finally, a detailed mesoscopic simulation including polymer effects is restricted to resolve the polymer repeat units of the resist. The high resolution therefore implies to simulate with a large number of cells to cover the whole simulation region. This consumes a substantial amount of computation time. Thus a faster model was developed working

at arbitrary resolutions where polymer effects are neglected. For this purpose the mesoscopic inhibitor concentration as obtained from the post-exposure bake step was combined with the previously developed fast marching algorithm and compared to a full mesoscopic simulation. Additionally a narrow-band level-set algorithm was developed. Although this algorithm has existed since 1988 for front propagation purposes a curvature term is here for the first time identified with a developer surface tension. The new term was here directly linked to a particle exchange at the resist-developer interface where its applicability is discussed. The resulting profiles were compared to scanning electron microscopy data where the fast marching algorithm showed the best overall performance.

List of acronyms

AFM:	Atomic Force Microsope
BARC:	Bottom Anti-Reflective Coating
CAR:	Chemically Amplified Resist
CD:	Critical Dimension
CoG:	Chrome on Glass
CPU:	Central Processing Unit
DDR:	Double Data Rate
DNQ:	Diazide NapthaQuinone, an early non-chemically amplified resist
DRAM:	Dynamic Random Access Memory
DUV:	Deep Ultra-Violet
EUV:	Extreme Ultra-Violet
KMC:	Kinetic Monte Carlo
LER:	Line Edge Roughness
MD:	Molecular Dynamics
MEMS:	Micro-Electro-Mechanical-System
MOEMS:	Micro-Opto-Electro-Mechanical-System
MOSFET:	Metal Oxide Semiconductor Field Effect Transistor
NA:	Numerical Aperture
PAB:	Pre-Apply Bake
PAG:	Photoacid generator
PBOCST:	poly(4-tert-butoxycarbonyloxystyrene), one of the first chemically amplified resist
PC:	Personal Computer
PEB:	Post-Exposure Bake
PSM:	Phase-shifting mask
r.u.:	Repeat unit (of a polymer)
SDRAM:	Synchronous Dynamic Random Access Memory
SEM:	Scanning Electron Microscope
TARC:	Top Anti-Reflective Coating
TMAH:	Tri-methyl ammonium hydroxide, a common developer used in lithography
TPST:	Triphenyl Sulfonium Triflate, a photoacid generator.

1. Introduction to memory technology

Today every personal computer (PC) is already provided with hundreds of megabytes of fast accessible Dynamic Random Access Memory (DRAM) which is found in a variety of products ranging from graphic cards and servers over consumer PC's to mobile phones. While a single DRAM chip is build up of billions of transistors further increase in memory storage capacity is achieved by shrinking the gate length of each transistor. Current productive feature sizes are already down to 70 nm. By the resulting decreased size more functionality can be added to the same chip thus reducing production cost per bit. Also a lower power consumption for decreasing critical dimensions are achieved. This relation follows a double logarithmic plot called *Moore's Law* [1] which was valid for the last forty years. It states that the number of transistors on a chip doubles approximately every two years. This relation is shown in Fig. 1.1 where the number of transistors, here in a microprocessor as published by *Intel* for their different central processing units (CPUs), were plotted over their year of appearance. The scale on the y-axis corresponds to log_2. But as feature sizes approach the atomic length scale this trend for the case of DRAM may become invalid [2]. Already today more and more physical effects on a mesoscopic scale start to affect the final device performance. Especially the roughness effects in current photoresists seem to be a major limiting factor when feature sizes are below 40 nm. To better understand the impact of roughness on the final device performance a short review on the operation and production principle of current DRAM will be given.

1.1. Dynamic random access memory

A simple schematic describing the basic operation principle of DRAM is shown in Fig. 1.2. Here the metal oxide semiconductor field effect transistor (MOSFET) acts as a switch. By applying a voltage on the word line a conduction channel can be created which allows for a current to flow from the bit line to the capacitor or vice versa. By this the capacitor can be charged or discharged. Also a transferred charge can be stored for a certain time inside the capacitor. Then a filled capacitor corresponds to a bit set to 1, and an empty capacitor to a bit set to 0 whereas the word line allows for setting or reading out a single bit. As the change in voltage at the bit line is small when data is written or read out a sense amp is connected to each line. It amplifies a given voltage change. In order to store the information over longer periods of time the stored charge inside the capacitor

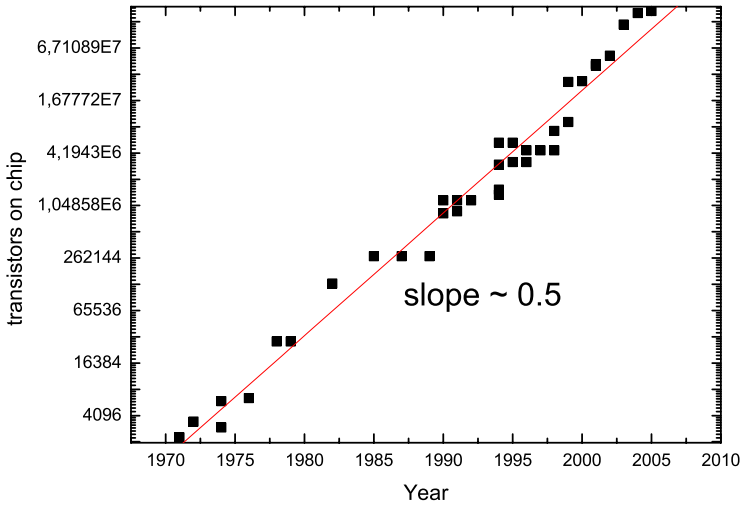

Figure 1.1.: Moores law

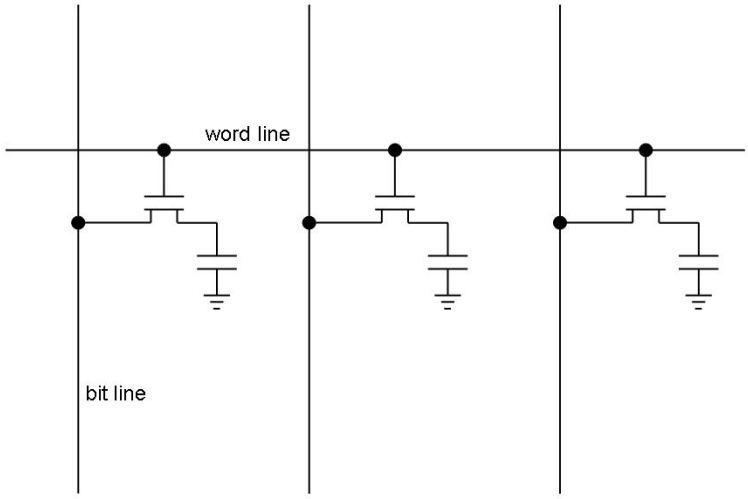

Figure 1.2.: Basic DRAM circuit showing three memory cells

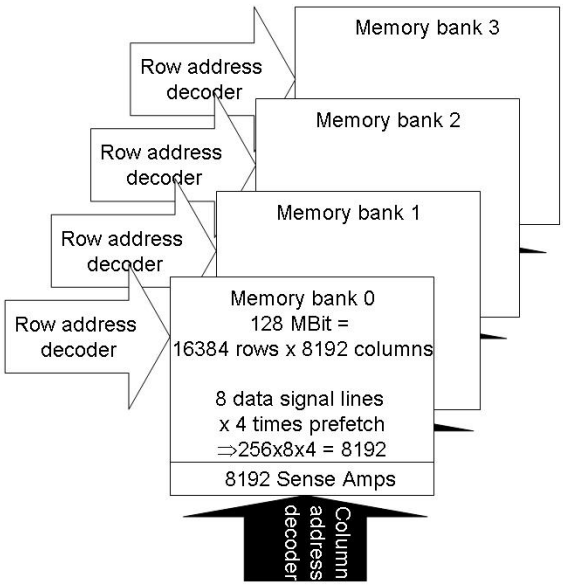

Figure 1.3.: Higher level organization of current SDRAMs

needs to be refreshed on a timescale of ms. As a read or write operation is in the order of ns over a million read or write operations can be made before a refresh occurs. These operations are today synchronized with the CPUs front side bus, reducing possible delay times, therefore speaking of synchronous DRAM (SDRAM). According to [3] the shown basic SDRAM cells are organized in banks, where two, four or eight banks (depending on the current SDRAM type) sum up to a memory cell array. Each cell array is connected to a data signal line which can be addressed via a row address decoder for the word line, or a column address decoder for the bit line. The reason for this hierarchical organization is that each bank can work partly independent from the other banks which allows to accelerate DRAM operation. A further acceleration can be achieved by prefetching data during one read out cycle. This prefetch is expressed in terms of a double data rate (DDR) with an added number. Thus e.g. DDR2 means that during each read operation not one bit but four bits are read out. Accordingly DDR3 allows for eight bits to be read out simultaneously. An example is shown in Fig. 1.3 for a 512 MBit DDR2-SDRAM consisting of 8 data lines and 4 banks, also written as 64×8 DDR2-SDRAM to show the number of data lines. Each bank then allocates 128 Mbit, and is thus addressed by $128Mbit = 16384\ rows \times 8192\ columns$. Note how the four times prefetch leads to an organization of the columns in groups of $8192 = 256 \times 8 \times 4$.

Currently there are two major approaches for building DRAM which differ by the placement of the capacitor. The capacitor plates can either be wrapped on top of the gate and the bit line, known as a stacked capacitor, or can be drilled deep inside the silicon creating a narrow hole known as a deep trench. Both methods aim at an increased area

of the capacitor plates which is directly proportional to an increase in capacity. Here only the deep trench method will be considered further. A schematic of a current real deep trench memory cell stack is shown in Fig. 1.4 together with a scanning electron microscope (SEM) picture in Fig. 1.5. To build these stacks efficiently hundreds of process steps are necessary which can be grouped e.g. into crystal growth via chemical vapour deposition, transfer of chip layouts on the wafer via optical lithography, dry and wet etch, and chemical mechanical polishing to name a few. This work is mainly concerned with lithography, and here especially with the line edge roughness (LER) formation in photoresists. The definition of LER and why it is so important for building DRAM will be explained in the following.

1.2. Line edge roughness

When looking on top of the MOSFET at the gate the resulting line including LER is displayed in Fig. 1.6. An ideal straight line is not printed but fluctuations in line width occur. When looking at a single edge these deviations from an ideal line are in general described by the standard deviation. Denoting by x_i the current position of the edge, and by x_m the mean value of the edge position averaged along its length, and N being the number of sample points, the standard deviation 3σ or LER is defined as

$$3\sigma = 3\sqrt{\frac{\sum_N (x_i - x_m)^2}{N-1}} \tag{1.1}$$

The terminology in terms of three times the standard deviation arised from process stability considerations. When considering only values of $\pm\sigma$ around the mean only 68% of possible edge values are captured if a gaussian distribution is assumed. A more comprehensive characterization is obtained when values of $\pm 3\sigma$ around the mean are considered. These include more than 99% of possible fluctuations in gate length which may be crucial when modelling device performance. To understand how LER affects MOSFET device performance a closer look on the MOSFET working principle will be taken as shown in Fig. 1.7. When a voltage V_{th} above a threshold level is applied to the gate a depletion region inside the p-type substrate will be formed such that a current can flow via an n-channel from the source to the drain if the bit line is high (meaning that a positive voltage is applied to the source). Typical values are $V_{th} \approx 1.8\ V$. However, if the capacitor connected to the drain is charged and $V_{th} = 0$ a leakage current I_{off} will occur such that the cell needs to be refreshed after some ms. If now a line edge roughness arises during optical lithography and is transferred via an etch process to the later forming gate, two major fluctuations increase after [6]. They reported an increase of I_{off} variations as critical dimension (CD) of the gate decreases. While the impact of LER on I_{off} variations was low for large gate CDs it increased for decreasing CDs. The same was true for V_{th}. This is important as depending on the magnitude of fluctuations a severe increase in power

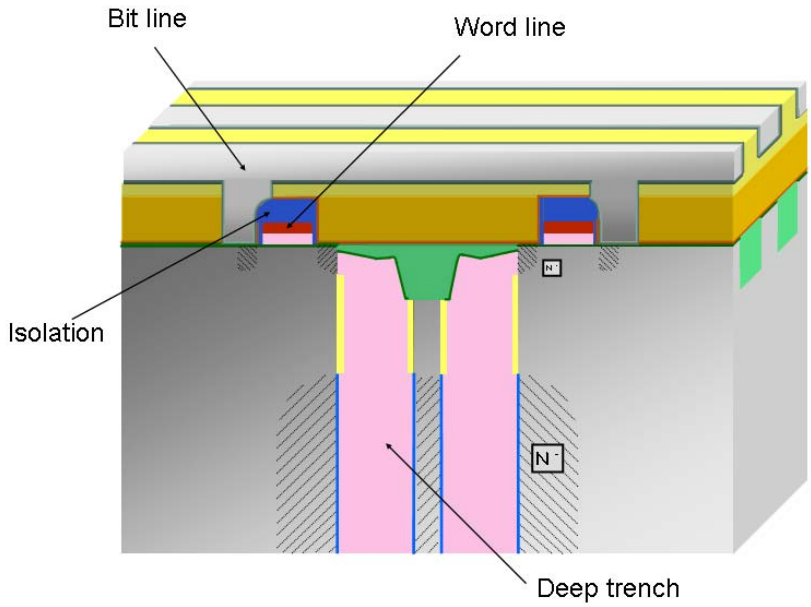

Figure 1.4.: Schematic of a memory cell on a silicon wafer. The word and bit lines are shown as well as the deep trench capacitor in which the charge is stored. Taken from [4].

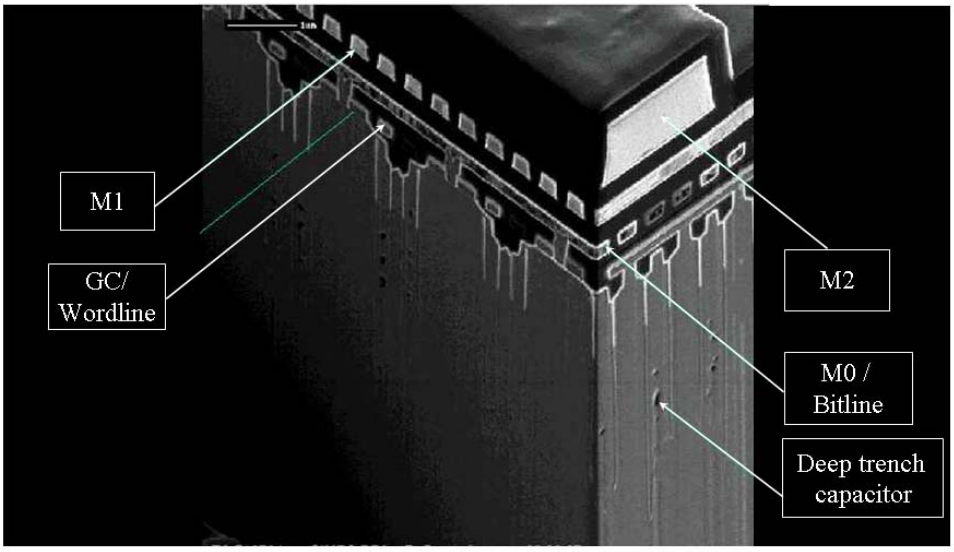

Figure 1.5.: Scanning electron microscope picture of a final DRAM. Above the bit line further contacts have been added to achieve the previously mentioned grouping in terms of banks and data lines. Taken from [4]

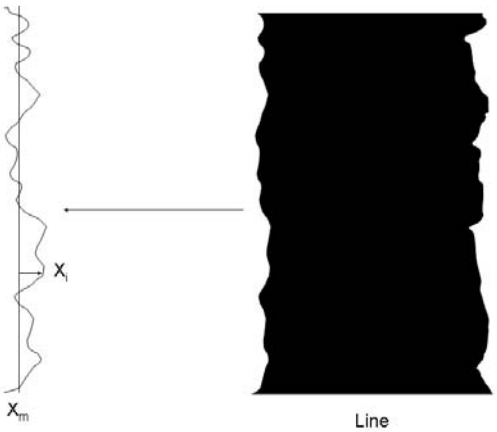

Figure 1.6.: Top view on a MOSFET gate where line edge roughness is displayed.

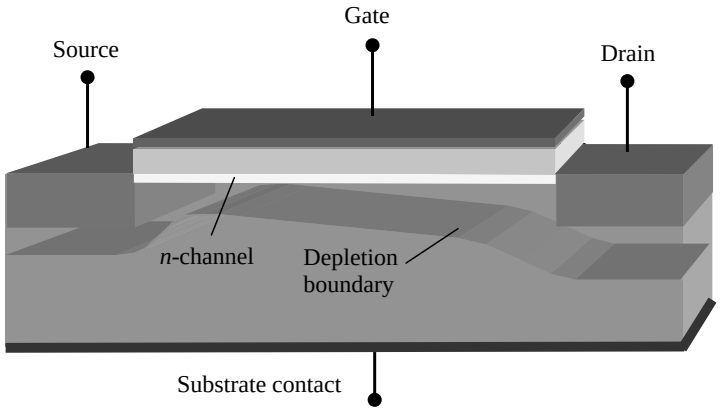

Figure 1.7.: A n-type MOSFET where besides the source, gate and drain contacts the silicon oxide below the gate is shown. The substrate is p-type. The depletion region together with the n-channel formed when the gate voltage is above a certain threshold voltage is shown. Taken from [5].

consumption of DRAMs can occur. They conclude with LER effects to be considered for gate CDs below $85nm$. The increased variations can be understood in terms of enhanced scattering effects at the source-gate and gate-drain interface and were modelled by several groups, e.g. [7]. But after [6] they seem to be not as large in experiment as predicted in simulation. As in general a large LER created during lithography will be transferred by the subsequent etch step to the gate a first obvious choice is to reduce LER already during lithography. This leads to a major research field, the optical lithography.

2. Introduction to optical lithography

The main processes of optical lithography are displayed in Fig. 2.1. First the wafer is coated with a properly designed chemically amplified resist. This is achieved by rotating, or spinning, the wafer at several thousand rounds per minute while pouring the liquid photoresist on its center. By the acting centrifugal forces a thin resist film is created where its thickness can be controlled by adjusting the spinning velocity. As a second step the spin-coated wafer is moved to a baking plate where a pre-apply bake (PAB) is made during which the solvent content of the photoresist is reduced. Then the wafer is moved to the stepper where it is exposed to UV light. Afterwards a post-exposure bake (PEB) step on the previous described baking plate follows. During PEB photogenerated acid diffuses through the polymer matrix. Close to light exposed regions the polymers that form the resist are "deprotected" in an acid- catalyzed reaction. The deprotection process consists of a chemical conversion of "blocking groups" which are attached to the polymers. These blocking groups prevent dissolution of the resist polymers in the subsequent development step. After development a hard bake follows to dry the resist for further processing. The pattern transfer into the wafer is realized by an additional etch step where the resist protects the underlying layers. Then material removal only occurs in regions where resist has been dissolved. After etching remaining parts of the resist are stripped e.g. by an additional etch step where now only resist is dissolved. For modelling purposes regarding lithography these processes can be simplified into simulating only the exposure, PEB and development steps. In the following a short description on current modelling approaches for each of these fields will be given starting with the important field of optical imaging.

2.1. Optical imaging

In Fig. 2.2 a) a simplified picture of an optical system is shown. A source is placed in the focal plane of a condenser lens. This leads to a parallel beam such that the photomask, also called reticle, behind the condenser is uniformly illuminated. After passing through a projection optic which demagnifies the image typically by a reduction factor of 4 a final photomask image is created on the wafer. This schematic is depicted in Fig. 2.2 a). Real optical systems may consist of up to 40 lenses and may weigh more than 6 tons, an example of a real projection optics is shown in Fig. 2.2 b). This picture also reveals the approximation made when modelling the aerial image in lithography, where the whole

projection lens system can be simulated by only considering one projection lens with an effective numerical aperture. Additional aberration effects can be modelled by including Zernike polynomials while polarization effects can be modelled within the theory of Jones pupils [8, 9]. The basic imaging equations describing the optical system are based on the solution of the Maxwell equations. As the resulting wave equation is already well known [11] a brief summary following the derivation in [12] can be found in the appendix A concluding that diffraction in the far field can be effectively modelled via a Fourier transform. Now the basic limiting factors for printable CD in terms of the aerial image will be derived together with some common resolution enhancement techniques before the chemical reactions inside the illuminated photoresist will be considered.

2.2. Aerial image

For the case of a periodic pattern with periodicity or pitch $2d$ coherent illumination will lead to a set of discrete diffraction orders as shown in Fig. 2.4 for on and off-axis illumination where only the zero and first orders are shown. Here also the influence of an off-axis illumination is visible which simply shifts the position of the diffraction orders. The relation between the angles Θ and Θ_i is given by

$$\sin\Theta_m - \sin\Theta_i = \frac{m\lambda}{2d}\ ,\ m = 0, \pm1, \pm2, ... \tag{2.1}$$

The amount of diffraction orders used for imaging is limited by the opening angle α of the projection lens such that the condition $\sin\Theta < \sin\alpha$ must be fulfilled. A more rigorous derivation can be found in the appendix, see B. This will lead to a set of waves $e^{i\vec{k}\vec{x}}$ with discrete wave vectors interfering to produce a final intensity pattern where $\vec{k}\vec{x} = k(\sin\Theta_m - \sin\Theta_i) = m\pi/d$ and $k = 2\pi/\lambda$. Thus by defining the numerical aperture of the projection lens by $NA = \sin\alpha$ an important resolution limit for the case of on-axis illumination ($\sin\Theta_i = 0$) for line and spaces is obtained

$$\lambda/2d < NA \tag{2.2}$$

$$\rightarrow d > 0.5\ \frac{\lambda}{NA} \tag{2.3}$$

For off-axis illumination this can be reduced to the theoretically resolvable limit for $\sin\Theta_i = 0.5NA$ of

$$d > 0.25\ \frac{\lambda}{NA} \tag{2.4}$$

This relation is often stated in the form

$$d > k_1\ \frac{\lambda}{NA} \tag{2.5}$$

Here k_1 is always ≥ 0.25 and can take further impacts of the current lithographic technology node into account such as the photoresist. As off-axis illumination lowers k_1 it is one

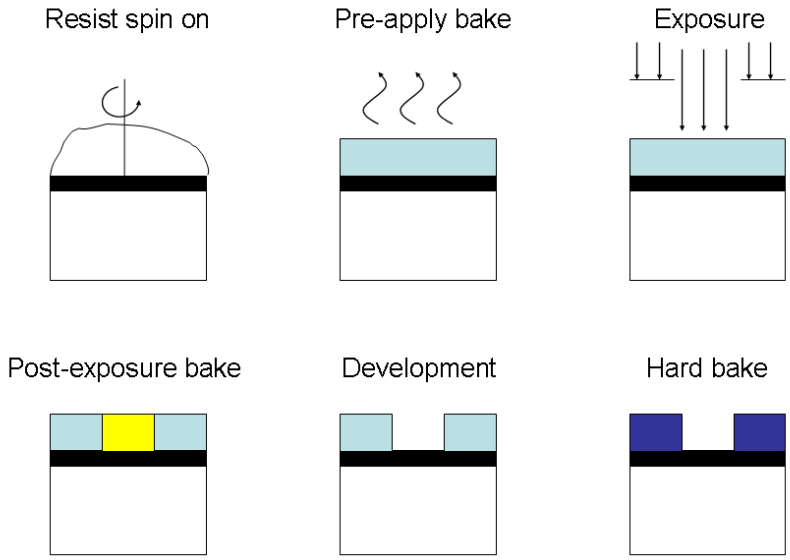

Figure 2.1.: Overview of the lithographic processes.

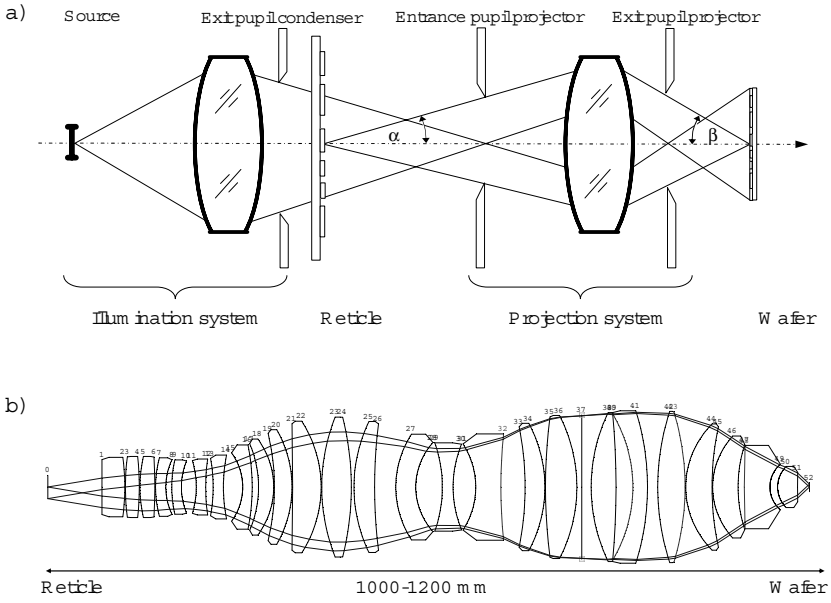

Figure 2.2.: a) Schematic of the optical imaging system in lithography. Light from e.g. an ArF laser passes through a condenser and uniformly illuminates the reticle. The pattern image is created on the wafer by a projection optic, typically demagnifying by a factor of 4. b) A real projection system as taken from [10].

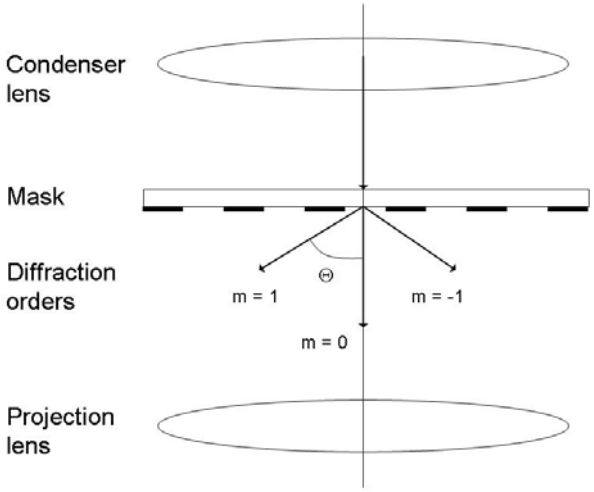

Figure 2.3.: Diffraction at a periodic mask for on-axis illumination

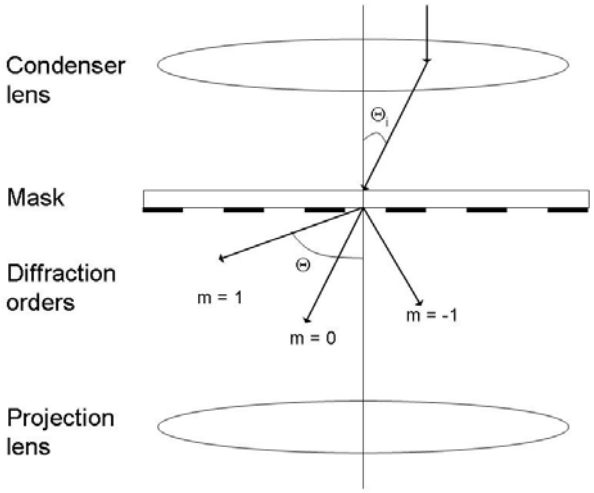

Figure 2.4.: Diffraction at a periodic mask for off-axis illumination

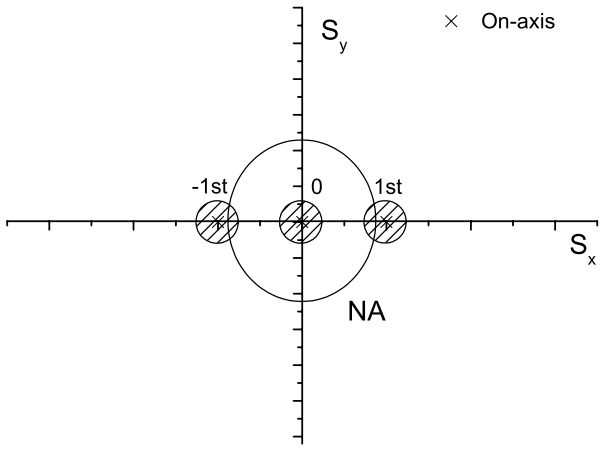

Figure 2.5.: Partial coherent illumination leads to broadening of the discrete frequencies in the object plane.

of the commonly used resolution enhancement techniques. Another important technique is the partial coherent illumination.

2.2.1. Partial coherent illumination

The previous discussion was based on a single coherent source point, but also partial coherent illumination is possible where coherence here is referred to as spatial coherence. This can be achieved by describing a cone of light emerging from the source where the amount of coherence is described by the partial coherence factor

$$\sigma = NA_c/NA_p \tag{2.6}$$

where NA_c denotes the NA of the condenser lens and NA_p the NA of the projection lens. $\sigma = 0$ then corresponds to coherent illumination while $\sigma = \infty$ for incoherent illumination. Practical values for σ lie between $0.3 - 0.8$. Going into the object plane where S_x and S_y are the corresponding normalized wave vectors along the x and y direction as defined in appendix B this leads to a pupil filling as shown in Fig. 2.5. Besides reducing aberration and laser speckle effects partial coherent illumination allows for resolution enhancement as e.g. first orders which otherwise would lie outside the NA can still contribute to the final image. However, contrast is lost for features which would be resolvable with coherent illumination. Depending now on the pattern to be imaged several off-axis illuminations are possible with different degrees of coherence. The most commonly used source shapes are displayed in Fig. 2.6. E.g. dipole illumination is useful for lines and spaces as the first order diffraction peaks are shifted towards the centre of the lens as previous discussed. For most of the simulations done here circular illumination will be sufficient.

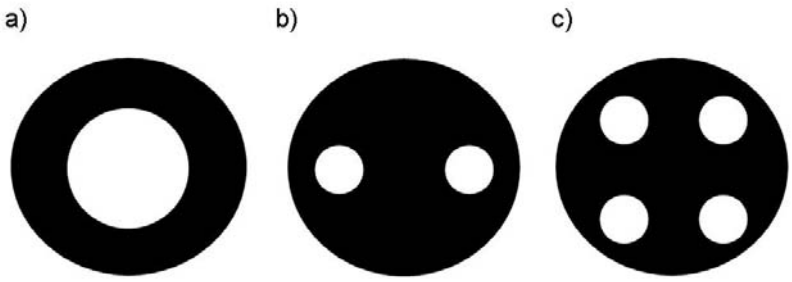

Figure 2.6.: Different source shapes commonly used in lithography. a) Circular illumination. b) Dipole illumination. c) Quadrupole illumination

2.3. Photomasks

So far one of the most important optical imaging elements, the mask, has not been discussed. In general up to now a simple binary mask was assumed. These are usually fabricated by putting some chrome on top of SiO_2, leading to zero transmission as shown in Fig. 2.7 a) for the chrome on glass (CoG) mask. To further improve image quality various other types of mask can be used. These are phase-shifting masks, first proposed in [13]. The alternating phase-shifting mask for example leads to a 180 degree phase shift between neighbouring bright regions, thus enhancing contrast as shown in Fig. 2.7 b). But due to the mask fabrication process being more expensive for alternating phase-shifting masks and possible conflicting patterns arising in non-periodic layout structures where bright features of opposite phase meet they are only sparsely applied [14]. Therefore in most of the simulations in this thesis an attenuated phase shift mask is used as shown in Fig. 2.7 c). Here a 180 degree phase shift is introduced into the dark regions by e.g. MoSi, where still a portion of light is transmitted, typically between 6% to 8%. By this the zero order of the transmitted light is reduced. This lowers the constant intensity background for three or more interfering orders and allows for a better balancing between zero and first order. Thus contrast is enhanced.

2.4. Photoresists

The photoresist is the critical layer which transforms the intensity distribution of the aerial image into a desired pattern. A good overview on the history of photoresists can be

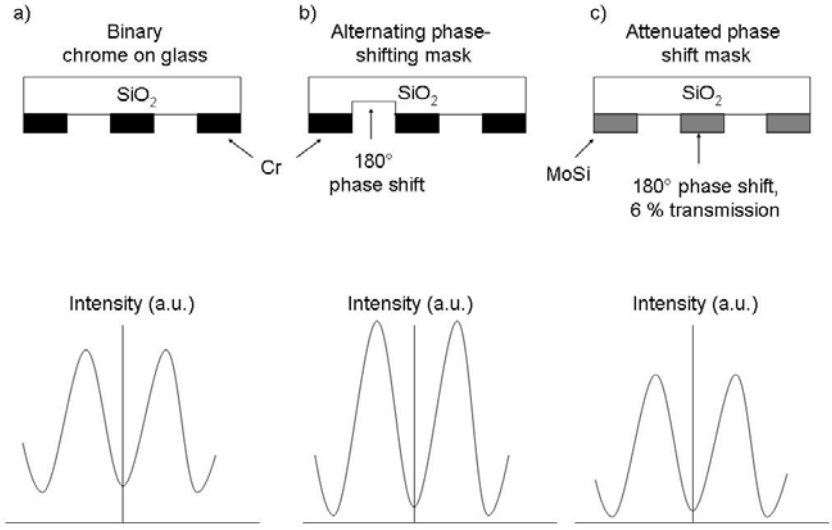

Figure 2.7.: Three different commonly used masks

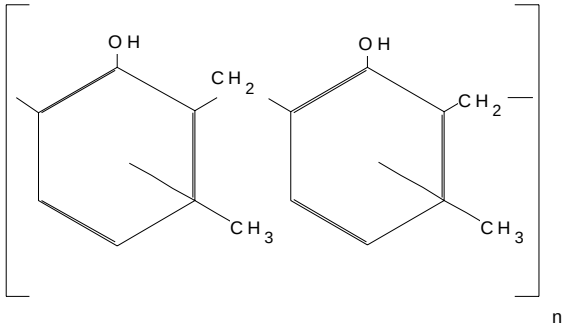

Figure 2.8.: Novolak resin shown in the ortho-ortho coupling configuration

found in [15], here only their basic properties regarding simulation will be introduced with chemical details given for a famous early deep UV (DUV) resist. In general the resists can be divided into two groups, the positive (p-type) and negative (n-type) photoresists. Whereas the positive resist becomes soluble in light exposed regions, the negative resist turns insoluble due to cross-linking reactions. The resists are then usually dissolved with an aqueous base developer, such as NaOH, KOH, or the widely used tetramethylammonium hydroxide $[(CH_3)_4NOH]$. For this work only positive resists have been considered, therefore a closer look into their design will be taken. During early lithography where exposure wavelength was determined by the g- (436nm) and i-line (365nm) of the used mercury lamp photoresists were not chemically amplified. The standard resist used consisted of a novolak resin shown in Fig. 2.8 mixed with a photoacid compound, typically diazide napthaquinone (DNQ). Upon exposure this compound turned into a keto-carbene which after reacting with water transformed to a carboxylic acid. The aqueous base de-

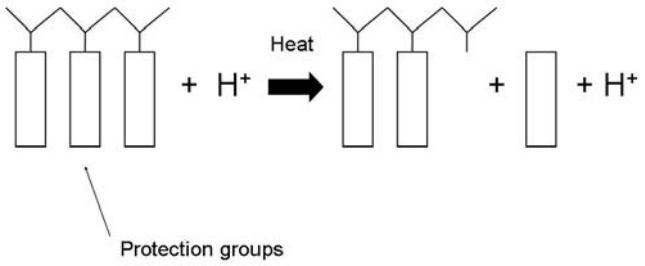

Figure 2.9.: Principle of chemical amplification

veloper solution now experienced an improved dissolution rate in regions where enough carboxylic acid has been created.

2.4.1. Deep UV resists

As lithography reached smaller structure sizes illumination wavelength changed to 248nm in the DUV [16]. Compared to the g- and i-lines now much less intensity was available which demanded a resist with higher sensitivity. This problem was solved by a new major invention in resist technology, the chemically amplified resists [17], which are still in use today. The basic principle is shown in Fig. 2.9. Here the polymer backbone is surrounded by protection groups which prevent dissolution during development. These groups can be removed from the backbone via an acid-catalyzed reaction. The acid is produced by photoacid generators upon exposure. They consist of a chromophores and a counterion, an example for triphenyl sulfonium triflate (TPST) is shown in Fig. 2.10. As a single acid molecule can take part in various deprotection reaction an increased sensitivity is obtained when compared to the novolak-DNQ resist. As this deprotection occurs at high temperatures, typically around 130° C, the acid molecule additionally diffuses through the resist matrix thus deprotecting larger regions. Typical diffusion lengths range from 20nm to 30nm. The first chemically amplified resist was polyhydroxystyrene with tertiary-butoxycarbonyl (PBOCST) as a protection group, introduced by IBM. It described for the first time a standard design for chemically amplified resists. The polymer is build up by attaching an etch barrier to the polymer backbone together with an acidic group which can be ionized during development with an aqueous base. Attached to the acidic group is a protection group which can be removed by the acid catalyzed reaction during post-exposure bake. The schematic of a model type resist together with the chemical structure of PBOCST is shown in Fig. 2.11 a) and b). Today lithography is performed

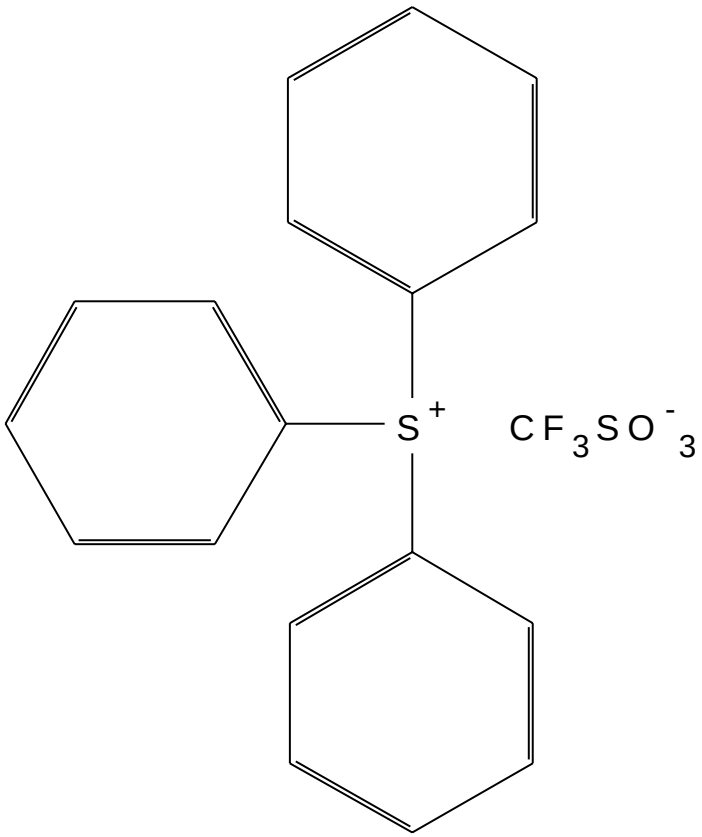

Figure 2.10.: The photoacid generator (PAG) triphenyl sulfonium triflate (TPST)

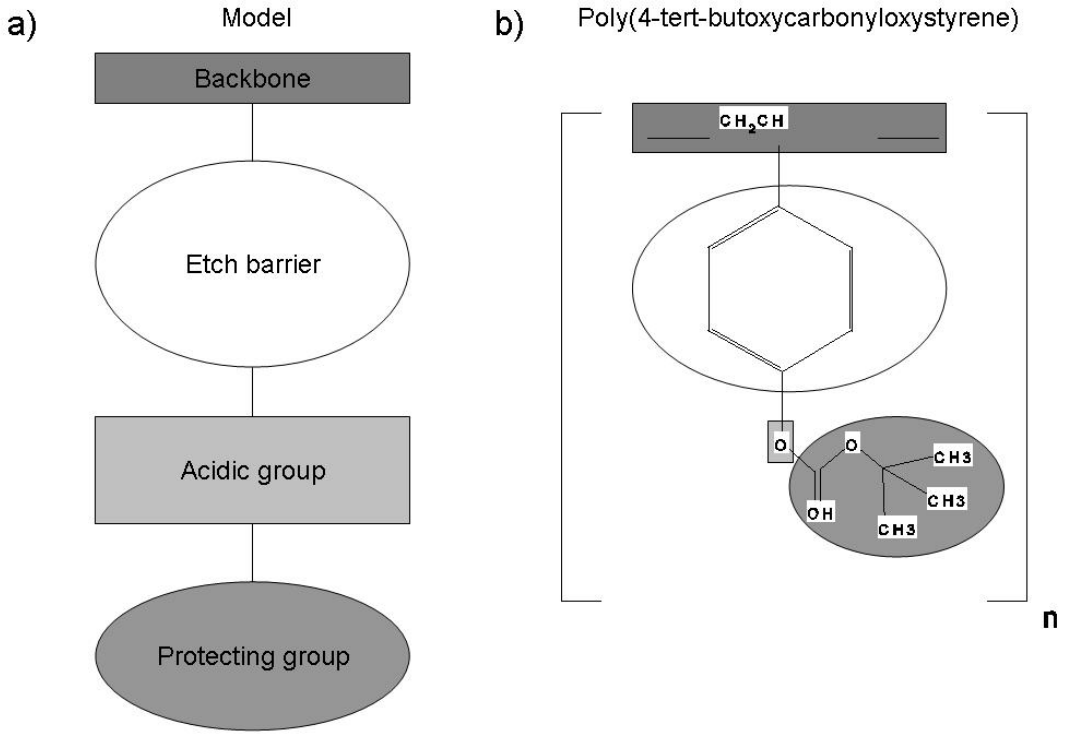

Figure 2.11.: a) Design of a chemically amplified resist with the corresponding functional groups. b) Chemical structure of poly(4-tert-butoxycarbonyloxystyrene) (PBOCST) with the functional groups made visible. After [15].

at an illumination wavelength of 193 nm resulting from excimer lasers [18]. Although the illumination wavelength changed the 193 nm resists are based on the same concept of functional groups where the detailed chemical structure differs[1]. Before coming to the details regarding the development also a fourth important component inside the resist needs to be discussed. Besides the polymers with their dissolution inhibitors, photoacid generator (PAG) and acid molecules also base is present inside the resist. While part of the bases inside the resist are unwanted poisoning effects from the surrounding environment it is also used on purpose to control acid diffusion and enhance inhibitor contrast after PEB. In general a constant amount of base is added to current resists, typically in the range of $5\% - 10\%$ *wt.* in terms of PAG. Inhibitor contrast is improved as in the darker regions where the line is going to be formed unwanted acid molecules are neutralized, while in the bright regions still enough acid remains.

[1] Especially the benzole ring shows a strong absorption at 193 nm which is mainly due to the double-bonding between the carbon atoms. Therefore the overall polymer changed from an aromatic to an aliphatic structure (e.g. cyclopentane) where only single bonds between carbon atoms occur. For details on 193 nm resists see e.g. [19].

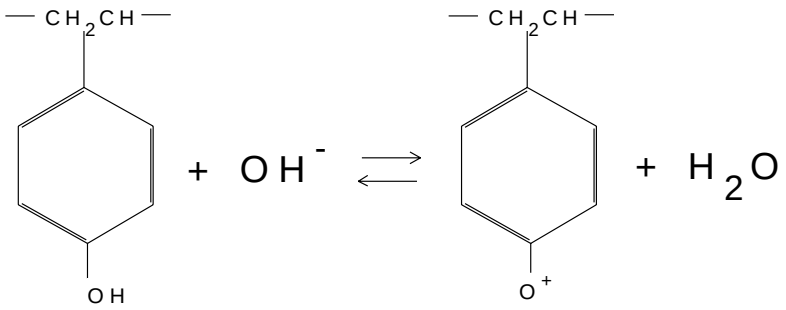

Figure 2.12.: Ionization reaction during development at the unprotected polymer site

2.5. Developers

As already mentioned previously the photoresists are developed in an aqueous base developer solution. While $NaOH$ and KOH developers are possible they are unsuitable for integrated circuit design as their cations are alkali metals and thus reduce gate oxide integrity [20]. Therefore trimethylammonium hydroxide (TMAH) became the standard developer used in most fabrication processes. The ionization reaction is shown in Fig. 2.12 where the hydroxide anion of TMAH ionizes the unprotected polymer repeat unit. It needs to be pointed out that the TMAH cation is approximately twice as large as the K^+ cation of KOH. This results in a strong dependence of the development rate on temperature. Here in general an increased temperature leads to a decrease in dissolution rate. The developer is provided in a dilute concentration measured in terms of normality in an industry standard of 0.26N TMAH. This standardization arised more in terms of a reduced developer cost than due to actual physical reasons. While resist dissolution can lead to considerable swelling and foaming additional surfactants are added to the developer reducing its surface tension and enhancing its wettability. These defoaming agents can also modify the developers dissolution rate as was found in [21] where in general an enhanced wettability (and thus lower surface tension) seems to increase the dissolution rate of the unexposed resist. After having described now the major physics of current resists and developers a closer look on process characterization methods will be taken.

2.6. Lithographic process characterization

A very important issue for the practical lithographer is a proper process characterization. As variations in dose or focus values commonly occur a process needs to be found where the resulting CD is mostly unaffected by smaller changes in either of them. The focus variations are a common problem as the wafer is not flat but depending on the strain exerted by temperature non-uniformity or the previous produced layers may show bulges which lead to a shift of the structures from best focus into defocus by up to $\approx 100nm$.

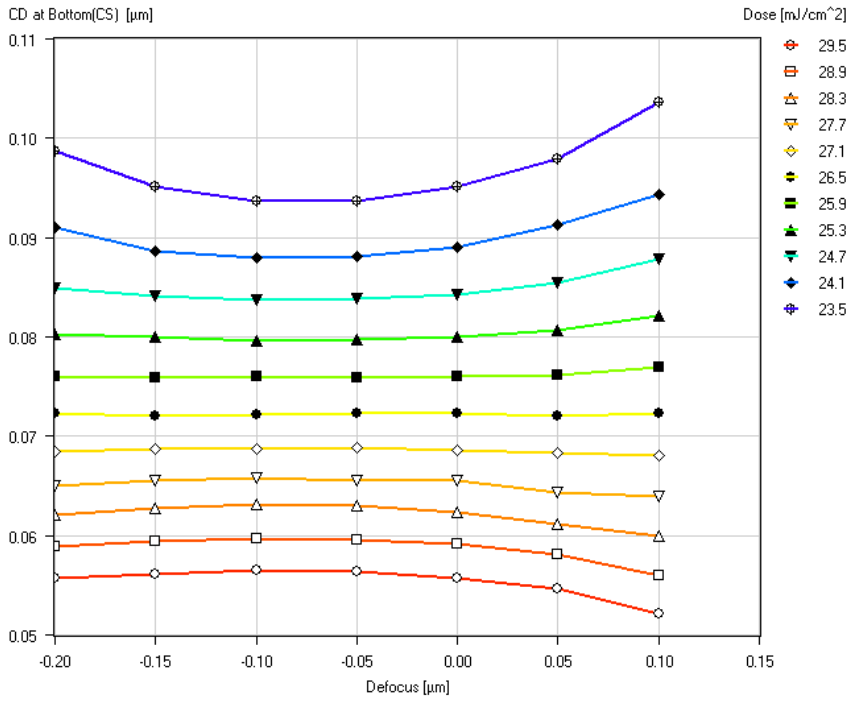

Figure 2.13.: Bossung plot for a line space grating with pitch 150 nm and line width 70 nm. Created with [22].

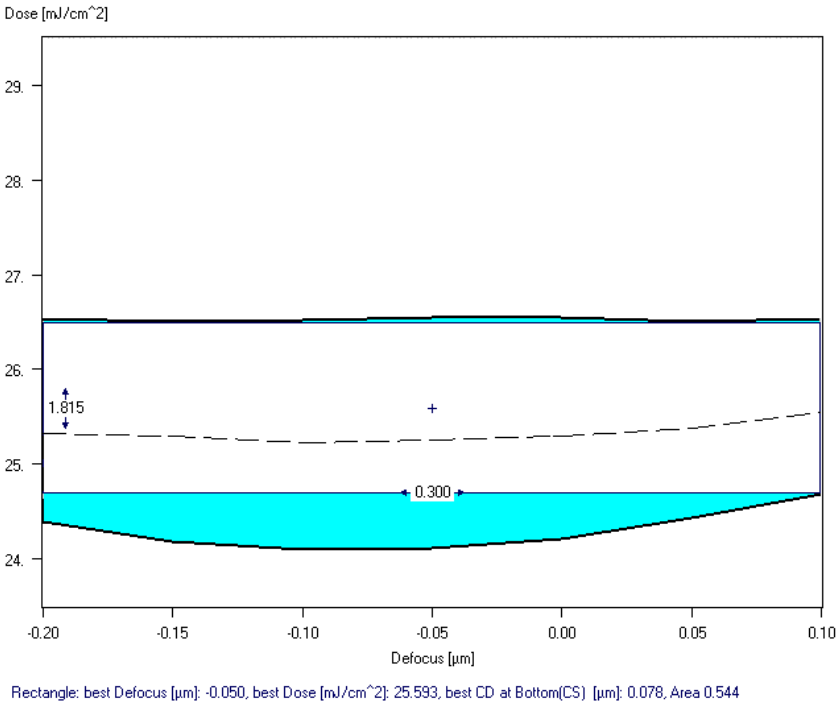

Figure 2.14.: Process window for $CD = 80nm \pm 8nm$. Created with [22].

A common plot to visualize the impact of changes in dose or defocus on the final CD is the bossung plot as shown in Fig. 2.13. Note the isofocal point in the bossung plot at approximately $CD = 70\ nm$ where the resulting CD is almost independent of defocus. If now a process is defined with e.g. a target value of $CD = 80\ nm \pm 8\ nm$ a process window from the bossung plot can be calculated as shown in Fig. 2.14. Of special interest is here the rectangular process window as it determines the best working point of the process, with e.g. here a depth of focus (DoF) of 0.30 μm and a dose lattitude of 1.8 mJ/cm^2 with the working point at a dose value of 25.6 mJ/cm^2 and a defocus value of $-0.05\ \mu m$.

3. Theory

After describing the main principles of lithography the focus will now lie on the basic methods applied for simulating the resist, and especially the resist development, on a continuous, mesoscopic and molecular level. The continuous or macroscopic approach neglects any fluctuations arising from the discrete numbers of PAG, acid and base molecules during PEB and the discrete nature of the photoresist which consists of many polymers during development. On the other side, a mesoscopic approach includes all these information up to a level of describing different acid molecules and polymer repeat units. This allows for simulation regions of several hundred nm within a reasonable computation time and describes the formation of LER. Finally a molecular dynamics approach models single atoms interacting via force fields and is the most accurate simulation method. But as resolution is on a microscopic scale in the order of Å only simulation regions of several nm can be simulated with time steps in the order of fs. As all these techniques were applied in this thesis they will be shortly discussed. First, the continuous theory for PEB and development will be derived where the current state of research will be summarized. A closer look will be taken on front propagation algorithms where as part of this thesis level set and fast marching methods were applied to solve the continuous resist development. Then stochastic simulation techniques based on Dynamic Monte Carlo methods will be introduced. This will lead to Kinetic Monte Carlo (KMC) methods [23] used in the field of physics for crystal growth. In this thesis a similar technique based on the Gillespie algorithm [24] used in computational chemistry to model the time evolution of complex chemical reactions was applied to model PEB and development on a mesoscopic level. The differences will be explained. Finally, to describe the polymers of the resist on a more fundamental level, also Molecular Dynamics simulation were studied to obtain a different polymer matrix to be used for PEB and development. The fundamentals of Molecular Dynamics will therefore be shortly discussed. This section will close with an introduction on current mesoscopic models and experimental results obtained in the field of LER simulation and characterization.

3.1. Macroscopic modelling of post-exposure bake

The modelling of the post-exposure bake on a *macroscopic* deterministic level is based on the solution of coupled partial differential equations and allows for simulation regions up

to the scale of several μm. These are based on two sets of equation. The first determines the acid concentration before starting the PEB

$$\frac{d[PAG]}{dt} = -C\ I(\vec{r})\ [PAG](\vec{r},t) \tag{3.1}$$
$$[A](\vec{r},t) = [PAG](\vec{r},0) - [PAG](\vec{r},t) \tag{3.2}$$

Here $[PAG](\vec{r},t)$ is the normalized PAG concentration at $\vec{r}$, $I(\vec{r})$ is the light distribution inside the photoresist, and C describes the conversion efficiency of the PAG as it determines how much initial acid is generated. C is also called the Dill C value of the resist. Accordingly the acid concentration after exposure $A(\vec{r},t)$ is simply calculated by subtracting the remaining PAG concentration after exposure from the initial PAG concentration. This initial acid concentration is used to calculate the deprotection and diffusion reactions taking place inside the resist by solving

$$\frac{d[M]}{dt} = -k_1[M]^p[A]^q - k_2[M] \tag{3.3}$$
$$\frac{d[A]}{dt} = -k_3[A]^r - k_4[A][B] + \nabla(D_A\nabla[A]) \tag{3.4}$$
$$\frac{d[B]}{dt} = -k_4[B][A] - k_5[B]^s + \nabla(D_B\nabla[B]) \tag{3.5}$$

where $[M]$ is the normalized inhibitor concentration and $[B]$ the normalized base concentration. D_A and D_B are the corresponding diffusion coefficients. The rate constants $k_1...k_5$ describes the various processes taking place during PEB. k_1 is the acid-catalyzed deprotection, k_2 is spontaneous loss of inhibitor, k_3 is spontaneous acid loss, k_4 is acid-base neutralization, k_5 is spontaneous base loss [25]. The exponents p, q, r, s control the order of the reactions taking place. Most of the time $p, q, r, s = 1$ while Fickian diffusion is assumed such that

$$\frac{d[M]}{dt} = -k_1[M][A] - k_2[M] \tag{3.6}$$
$$\frac{d[A]}{dt} = -k_3[A] - k_4[A][B] + D_A\Delta[A] \tag{3.7}$$
$$\frac{d[B]}{dt} = -k_4[B][A] - k_5[B] + D_B\Delta[B] \tag{3.8}$$

where Δ is the Laplace operator. This equation can be solved by an explicit or implicit integration in time. The method used in the PEB module in this thesis is based on an alternating direction implicit approach [26] where acid, base and inhibitor concentrations are staggered in time. The coupled system of reaction-diffusion equations is then solved simultaneously where less time steps are needed for convergence than compared to an explicit method. This comes at the cost of solving a set of linear equations at each time step, typically arranged in the form of a tridiagonal matrix. An example of a modelling of the exposure and post-exposure bake is shown in Fig. 3.1, 3.2 and 3.3. In Fig. 3.1 the mask used for illuminating the resist is displayed. The mask itself describes a contact hole array which is needed to e.g. produce the carbon hardmask later used for etching the

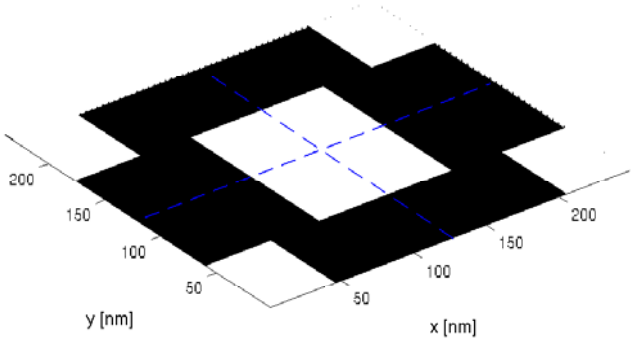

Figure 3.1.: The 2D mask as input for the aerial image simulation. The dashed lines denote the intersection planes along z at $x = 124\ nm$ and $y = 116\ nm$.

deep trench capacitor. In Fig. 3.2 the obtained intensity distribution inside the resist is shown. The resulting inhibitor concentration after PEB is displayed in Fig. 3.3.

3.2. Macroscopic modelling of development

The development is modelled by transforming the inhibitor concentrations into corresponding development rates. These development rates are usually very low as long as the inhibitor concentration is above a certain threshold and then suddenly increase by several orders in magnitude. To explain this behaviour a phenomenological fit function is applied to describe the dependance of development rates on inhibitor concentration. A common model used is shown in Fig. 3.4. Here the development rates were calculated by using the *Mack*4 [27] model

$$a = (n+1)/(n-1)\ (1-m_{th})^n \tag{3.9}$$

$$m = (1-[M])^n \tag{3.10}$$

$$v = R_{max}\frac{(a+1)\ m}{a+m} + R_{min} \tag{3.11}$$

Here v is the final development rate, n the developer contrast, R_{max} the maximum development rate, R_{min} the minimum development rate and m_{th} the threshold inhibitor concentration close to which a change of development rates occur. a and m are here only auxiliary variables to display v in a more appropriate form. The remaining problem reduces into tracking a developer front through the resist which travels with different propagation velocities corresponding to the underlying rates. Several techniques exist for

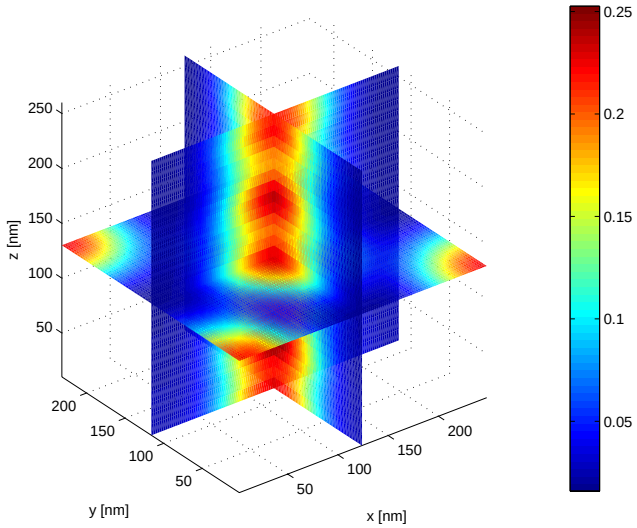

Figure 3.2.: Normalized intensity distribution as obtained from Fig. 3.1 with three intersection planes are shown. The third intersection plane is located at $z = 120\ nm$.

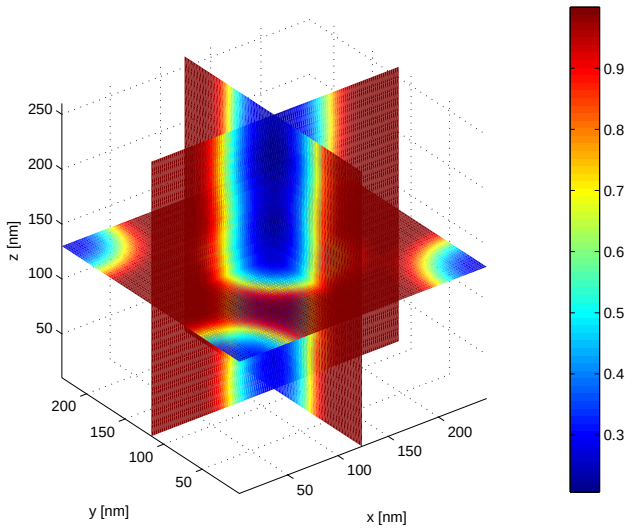

Figure 3.3.: Resulting normalized inhibitor concentration after a macroscopic PEB

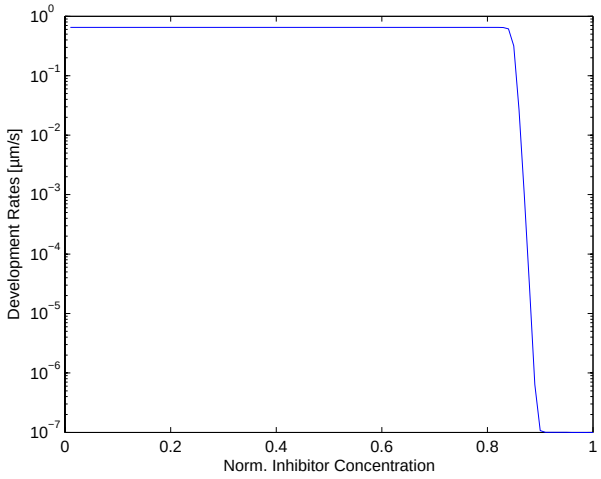

Figure 3.4.: Development rate v over inhibitor concentration $[M]$ calculated with a $Mack4$ model where $R_{max} = 0.6\mu m/s$, $R_{min} = 10^{-7}\mu m/s$, $n = 45$ and $m_{th} = 0.85$

possible solutions. The most common used is based on a cell removal algorithm [28]. Here the volume associated with each cell is divided into volume fractions, assigning a value of zero for cells being fully developed, a value between 0 and 1 for partly developed cells and a value of one to cells fully occupied by resist. Thus the information on the position of the front is mapped onto a so called fluid function f such that this method is also called *volume of fluid* method. For an incompressible flow the fluid function on a given velocity field can be propagated by an underlying partial differential equation of the form

$$\frac{\partial f}{\partial t} + (\vec{U} \cdot \nabla) f = 0 \tag{3.12}$$

where $\vec{U}$ is the velocity field. After the final volume fractions of the front have been calculated it needs to be reconstructed. Unfortunately the description of the front by volume fractions is not unique and various appoaches exist for accurate reconstruction [29, 30]. In general a large amount of cells is needed for accurate reconstruction while reconstruction itself is becoming increasingly complicated for three dimensional simulations. Also the problem of over- or underfilling of cells especially for large velocities must be considered. However, this method remains fast and can yield excellent results. But due to the expected problems a completely different approach has been implemented in this thesis based on a fast marching method which calculates the arrival times of the front. It was first proposed in [31] for simulation of photoresist development. A short introduction will be given in the following section where its details will be discussed in the results in section 4.

3.3. Level set and fast marching methods

When applying continuous models to the problem of resist dissolution a developer front must be tracked which travels through the resist with a velocity depending on its position.

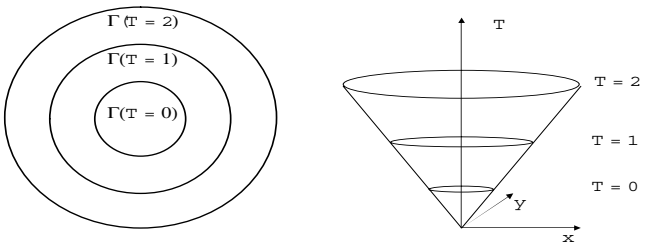

Figure 3.5.: Arrival times $T(x, y)$ for a front propagating in outward direction with unit velocity. After [33].

This can be solved by various methods. One was shortly discussed earlier based on a cell removal algorithm [29] but a completely different approach based on either calculating the arrival times of the front, the fast marching approach [31], or the actual position of the front at time t by embedding it into a higher dimensional function, the level set approach [32], can be used. This is depicted in Fig. 3.5 where a front $\Gamma(T)$ moving outward with unit velocity is displayed.

3.3.1. Fast Marching

For solving the arrival times $T(x, y, z)$ of the front in the case of the fast marching algorithm the basic equation $distance = front\ propagation\ velocity \cdot time$, which for an arbitrary small distance dx and a velocity F yield

$$dx = F dT \tag{3.13}$$

$$1 = F\frac{dT}{dx} \tag{3.14}$$

must be solved. The lower equation describes an isosurface, in multiple dimensions

$$F|\nabla T| = 1 \tag{3.15}$$

with a starting point defined by $T = 0$ on $\Gamma(0)$, where $\Gamma(t)$ describes the position of the front at time t which for a circular shaped curve moving in the outward direction with unit velocity is shown in Fig. 3.5. Note that this approach is a boundary value problem, where the position of the front at a certain time needs to be provided.

3.3.2. Level Set

Alternatively a level set method can be used where the front is embedded into a higher dimensional function $\Phi(x, y, z, t)$ as the zero level set [32]. Thus

$$Front \quad = \quad \{\ x, y, z \mid \Phi(x, y, z, t) = 0\ \} \tag{3.16}$$

The property of the function Φ, namely describing the front by a set of points within Φ at a certain level (or value), also gave this method its name. This defines a front that needs not to be given by a (unique) function but also holds in the more general case of an arbitrary surface, e.g. an ellipsoid which cannot globally be defined. Thus by the level set approach it is possible to solve non-planar surfaces with non-unique parameterizations. The time-evolution of the level set equation can be obtained by starting with

$$\Phi(\vec{\Gamma}(t), t) \quad = \quad 0\ , \tag{3.17}$$

$$\vec{\Gamma}(t) \quad = \quad \begin{pmatrix} x(t) \\ y(t) \\ z(t) \end{pmatrix} \tag{3.18}$$

Differentiation by the chain rule yields

$$\Phi_t \ + \ \nabla\Phi \cdot \vec{\Gamma}'(t) = 0 \tag{3.19}$$

Denoting by F the velocity in the outward normal direction $F = \vec{\Gamma}'(t) \cdot \vec{n}$, where $\vec{n} = \frac{\nabla\Phi}{|\nabla\Phi|}$ is the surface normal, yields

$$\Phi_t = -F\ |\nabla\Phi| \tag{3.20}$$

This equation is an initial value formulation of the surface evolution where only $\Phi(x, y, z, t = 0)$ and the velocity function $F(x, y, z)$ need to be defined for completely determining the time evolution of the front. This equation is typically solved by a finite difference scheme propagating the solution in time. It should be pointed out that while the level set method had a great impact on various research fields it was also applied to simulation of epitaxial semiconductor growth. While this field currently relies on Kinetic Monte Carlo (KMC) simulations as will be described in the next section a common problem is the simulation at high temperatures. They usually suffer from growth dynamics taking place at very fast and very slow time scales simultaneously. This demands a large number of time steps for computation. To decouple the different time scales adatom density KMC [34] has been introduced where a total adatom density is utilized to avoid calculation of single particle densities. Mandreoli et al. have proven that this approximation holds for the case of high temperature growth. In the same framework also a level set algorithm has been proposed for modelling epitaxial multilayer growth [35]. Here the island boundaries are associated with the zero level set within a level set function Φ. The velocity function propagating Φ is then determined by two steps. First the adatom density concentration

is determined by solving an underlying diffusion equation. Then the propagation velocity F for the level set function which propagates the island boundaries is determined by the change in density above and below the island boundaries.

3.4. Dynamic Monte Carlo methods

After the macroscopic or continuous approach for resist simulation has been described focus will now lie on the stochastic simulation methods applied for describing the resist on a *mesoscopic* level. This usually allows for simulation regions of up to some hundred nm. This will lead to Dynamic Monte Carlo methods and especially to the problem of solving a Markovian master equation. To derive its basic properties an example from statistical physics will be utilized after [36]. Consider a system in statistical physics with a large degree of freedom, a common example being the Ising model of a system of N spins $\vec{x} = S_1, ..., S_N$ of which each can be aligned up ($S_i = +1$) or down ($S_i = -1$). The total energy of the system can be expressed by the Hamiltonian

$$H(\vec{x}) = -J \sum_{<i,j>} S_i S_j - H \sum_{i=1} S_i \ , \ S_i = \pm 1 \tag{3.21}$$

where the first sum denotes the exchange energy of spin i with spin j where only nearest neighbour interactions are taken into account when summing up over all possible pairs. Of special interest are here thermal averages of any experimental observable A, in the canonical ensemble defined as

$$< A(\vec{x}) >_T \ = \ \frac{1}{Z} \int d\vec{x} \ e^{-\frac{H(\vec{x})}{k_B T}} A(\vec{x}) \tag{3.22}$$

$$Z \ = \ \int d\vec{x} \ e^{-\frac{H(\vec{x})}{k_B T}} \tag{3.23}$$

where k_B is the Boltzmann factor and T the temperature. Note that $p(\vec{x}) = \frac{e^{-\frac{H(\vec{x})}{k_B T}}}{Z}$ corresponds to a probability density. Due to the high dimensional space from the many different configurations possible these integrals are impossible to solve globally such that a different method, Monte Carlo, needs to be applied. Here only a small subset of configurations or phase space points M is studied. These states are selected at random utilizing pseudo-random numbers built by random number generators as commonly found in [37]. For $M \to \infty$ this will approach $< A(\vec{x}) >_T$. Unfortunately many randomly selected configurations will have a low probability of occurring when looking at a certain temperature T such that calculation would be more efficient if only configurations with a high probability would be considered. This was achieved by Metropolis et al. [38] who substantially improved the Monte Carlo method by introducing importance sampling. Here successive

configurations are not chosen independently from each other but according to a probability $P(\vec{x}_l)$.

$$\bar{A}(\vec{x}) = \frac{\sum_{l=1}^{M} e^{\frac{-H(\vec{x}_l)}{k_B T}} A(\vec{x}_l)/P(\vec{x}_l)}{\sum_{l=1}^{M} e^{\frac{-H(\vec{x}_l)}{k_B T}}/P(\vec{x}_l)} \tag{3.24}$$

This approach thereby utilizes the properties of a Markov process. In general a Markov process describes a correlation between successive states. Consider the spin states $x_1, ..., x_n$ occuring at times $t_1 > t_2 > ... > t_n$. For an uncorrelated process the conditional probability to find the system e.g. in spin configuration x_1 is independent of the probabilities to find it in any other state which can be written as

$$P((x_1, t_1)|(x_2, t_2), .., (x_n, t_n)) = P(x_1, t_1) \tag{3.25}$$

For a Markov process the conditional probability depends on the previous state such that

$$P((x_1, t_1)|(x_2, t_2), .., (x_n, t_n)) = P(x_1, t_1|x_2, t_2) \tag{3.26}$$

which also defines the Markov process. The process of generating successive states $\vec{x_l}, \vec{x_{l+1}}, ...$ with transition rates $W(\vec{x_l} \rightarrow \vec{x_{l+1}})$ (denoting a probability per unit time) is called a Markov chain. One can show that if suitable transition rates are chosen which obey the relation of detailed balance

$$P(\vec{x}_l)W(\vec{x}_l \rightarrow \vec{x}_{l'}) = P(\vec{x}_{l'})W(\vec{x}_{l'} \rightarrow \vec{x}_l) \tag{3.27}$$

$P(\vec{x}_l)$ will for $M \rightarrow \infty$ approach the equilibrium probability density

$$P_{eq}(\vec{x}_l) = \frac{e^{-\frac{H(\vec{x})}{k_B T}}}{Z} \tag{3.28}$$

which yields

$$\bar{A}(\vec{x}) = \frac{\sum_{l=1}^{M} A(\vec{x}_l)}{M} \tag{3.29}$$

and substantially improves the convergence of the algorithm. To introduce now a time dependence of the above processes a Markovian master equation in form of a partial differential equation can be set up. The probability $P(\vec{x}_l, t)$ to find the system in configuration $\vec{x}_l$ at time t then depends on

$$\frac{\partial}{\partial t} P(\vec{x}_l, t) = \sum_{\vec{x}_{l'}} [W_{\vec{x}_{l'} \rightarrow \vec{x}_l} P(\vec{x}_{l'}, t) - W_{\vec{x}_l \rightarrow \vec{x}_{l'}} P(\vec{x}_l, t)] \tag{3.30}$$

where all transitions of entering or leaving the system state $\vec{x}_l$ are taken now into account. Based on this time evolution Kinetic Monte Carlo simulations can be employed as found in [39–42]. Consider the system to be in a defined state l at $t = 0$. We are interested in finding the next possible system state l' and the time interval Δt after which this change

occurs. Therefore the total rate W_l consisting of all possible rates of leaving system state l must be calculated, namely

$$W_l := \sum_{l'} W_{\vec{x}_l \to \vec{x}_{l'}} \tag{3.31}$$

The time interval after which a transition occurs can then be described by

$$\Delta t = -\frac{1}{W_l} \ln (1 - r) \tag{3.32}$$

with r being an uniformly distributed random number within the interval $[0, 1)$. In the KMC algorithm a new uniformly distributed random number r_2 within the interval $(0, W_l]$ is drawn. E.g. for N different transition rates $W_{i=1}, ..., W_{i=N}$ for leaving state l the transition W_i occuring is then determined by the condition

$$W_{i-1} < r_2 \leq W_i \tag{3.33}$$

KMC can then be applied for the case of crystal growth or surface formation phenomena in physics [43–52] or most recently also in surface dynamics of growing cell populations in biology [53]. Here a similar concept was used applied to the simulation of the complex reaction-diffusion and ionization reactions during photoresist bake and development. The detailed theory derived for the resist simulation used here will be explained in section 5.

3.5. Molecular dynamics

A further technique applied here for simulating the photoresist was molecular dynamics (MD) simulation, first introduced in [54] for simulating the phase transition of a hard-sphere system. A thorough overview is given in [55]. In MD whole molecules or polymers typically on a *microscopic* scale from several $\mathring{A}$ to several nm can be modelled. The interactions between the different particles are described by a force field. The position x_i of particle i of mass m_i is propagated in time based on the total force F_i acting on it. This leads to an equation based on Newtons second law of motion

$$\frac{d^2\ x_i}{dt^2} = \frac{F_i}{m_i} \tag{3.34}$$

For this method to be successful time steps in the order of fs must be adjusted. Different particles or atoms are thereby connected via bonds. The force field is calculated by considering a harmonic potential for differences from their equilibrium value. A general potential V for a N particle system is then of the form

$$V(\vec{r}^N) = \sum_{bonds} \frac{k_i}{2}(l_i - l_{i,0})^2 + \sum_{angles} \frac{k_i}{2}(\Theta_i - \Theta_{i,0})^2 \tag{3.35}$$

$$+ \quad torsions + van\ der\ Waals + electrostatic \tag{3.36}$$

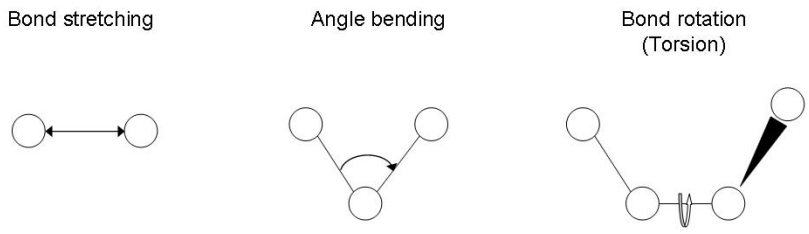

Figure 3.6.: Different bonding contributions to the final potential for MD. After [55]

Here $V(\vec{r}^N)$ is the potential energy which is a function of the positions $\vec{r}$ of the N particles. The first three terms include all bonded contributions. The first term includes all contributions from changes in bond length. Here l_i denotes the bond length of particle i together with its equilibrium value $l_{i,0}$ and k_i is a coupling constant. The second term includes all contributions from angle bending. Here Θ_i is the angle of particle i with neighbouring particles, again with $\Theta_{i,0}$ denoting the equilibrium bending angle. The third term is a potential describing bond rotation or torsion and is typically provided in form of a cosine series expansion. The last two terms include non-bonded interactions. The fourth term includes van der Waals forces and the fifth term electrostatic contributions. A schematic describing the different bonding contributions is shown in Fig. 3.6. In the simulations made in this thesis the above potential has been applied in the framework of an amber force field [56] which is frequently used in protein or nucleic acid simulation. This may show some deviations from the equilibrium value of photoresists. However, MD simulations in this thesis did not aim at an accurate description of polymer dynamics in the $\mathring{A}$ region but merely as a different way of generating an off-lattice distribution of polymers including bonding interactions to be used later during PEB and development. The reason was to investigate the changes in polymer structure on the simulation results. For improving computation time electrostatic contributions were neglected. As will be seen later the detailed polymer structure does not affect general trends obtained in LER simulation. But it may play a crucial role when trying to adjust the magnitude of LER.

3.6. Existing mesoscopic models

Today various models exist to explain roughness formation in resists. The mesoscopic models thereby rely on simulating the contributions of single acid molecules and polymer chains to the final roughness, thus incorporating fluctuations arising from statistically generated acid molecules during exposure, single acid diffusion and deprotection steps during PEB and removal of polymers during development. This is in contrast to the continuous models which neglect to incorporate all these fluctuations. As soon as the mesoscopic models take the polymer molecular weight into account most of them rely on the critical ionization model. Its foundations were laid when dissolution of early novolac resists could be explained by taking the degree of ionization of polymers into account [57]. A single polymer is then dissolved as soon as a sufficient number of its sites are ionized. By distributing polymers onto lattice sites the deprotection and dissolution of these polymers were modelled [58] where later an additional electric double layer was introduced [59, 60]. Here also the impact of increasing polymer weight on surface roughness was investigated, where a linear increase was found in accordance with [61].

As the previously discussed approach is based on resolving the polymer repeat unit different methods have been proposed to allow for simulation of larger patterns while including line edge roughness. One approach assumes statistically generated acid molecules during exposure and applies a simplified, phenomenological approach for obtaining the final development rates, thus omitting a full solution of the PEB equations [62]. It assumes that the development rate is much larger in regions where enough acid molecules have been created compared to the region where the later resist line forms. The resist can then be described by a two-phase system (or a simple threshold model) such that a percolation theory is applied. As development time increases the deprotected regions filled with developer expand and form connecting paths and thus percolate through the resist. With this model the film thickness loss of the resist can be explained quite accurately while including surface roughness evolvement. Similar to this approach a model based on soluble site density was developed where reaction and diffusion during PEB are treated by Monte Carlo methods [63, 64] thus allowing for statistical fluctuations. With this model the different developer contrast of positive and negative electron beam resists could be described well.

Also a third kind of model exists which solves the problem of simulating line edge roughness fast by introducing a convolution kernel which is applied upon the statistically generated acid distribution after exposure [65]. This resist deprotection blur function then simulates the PEB and defines the deprotected regions inside the resist. These can then be dissolved by e.g. applying a simple threshold development. The main advantage of this model besides being fast is its ability to predict roughness trends analytically. But unfortunately base effects are not included.

The simulator developed here is based on the work by Patsis et al. [66–68]. It is based upon the critical ionization model by Willson et al. [60] but introduces some approximations. While Willson et al. allow for polymer reordering by reptation algorithms and explicitly take the developer diffusion into account Patsis et al. assume a static polymer dissolution and instantaneous developer diffusion which considerably improves the computational efficiency. Recently also a new event based development algorithm was introduced [69, 70] which follows a similar approach as Patsis et al. while incorporating LER effects by Monte Carlo techniques.

While an overview of current existing simulators was now given the basic experimental trends measured by many groups will now be discussed. A good simulator which incorporates LER must fulfill all of these findings while maintaining a reasonable computation time.

3.6.1. Experimental results

Many resist screens have been performed aiming at an understanding of line edge roughness for small pitches. In general LER depends on the quality of the aerial image, as e.g. found in [71]. This was recently verified for the 193nm platform in a thorough screen in [72]. Here the increase of LER was even related one step further, not anymore to the aerial image, but directly to its resulting effect: Decreasing inhibitor contrast in the region of edge formation after PEB, or polymer protection gradient as it is called there.

Also a second often observed LER trend can be found there: A decrease in LER for increasing base concentration when adjusting the dose to size accordingly. Similarly for EUV based platforms a decrease in LER for increasing dose to size when changing base concentrations or acid diffusion was observed in [73, 74] where no agreement at the moment exists whether these effects are related to shot noise.

Finally in [75] a LER trend regarding acid diffusion length for DUV resists was observed. They performed a series of line width and LER measurements in a certain double exposure set-up where they varied the pre-apply bake, and thus the solvent content of the resist. They showed that an increase in acid diffusion length when comparing same line widths initially reduces LER while it increases again for large diffusion lengths $> 45\ nm$. However, acid diffusion length is not measured directly but determined indirectly within the context of an edge roughness evaluation method proposed in [76].

4. Continuous model: Fast Marching Development

4.1. Introduction

After describing the field of optical lithography and deriving the basic methods applied a closer look will now be taken on the exact algorithms developed and results obtained. This leads to two fields, the *continuous* and the *mesoscopic* resist simulation. In the current *continuous* section the fast marching algorithm developed as part of this thesis to model photoresist dissolution will be introduced. A benchmark has been performed comparing the fast marching algorithm to a level-set algorithm from [77]. With this algorithm and other already existing modules for simulation of the exposure step and the subsequent post-exposure bake step in lithography a new double exposure process was invented and simulated where its properties will be discussed for the first time here.

In the next section 5 the algorithm for *mesoscopically* simulating the photoresist bake and development will be explained. Together with an already existing mesoscopic post-exposure bake simulation method fundamental calculations discussing some limitations of chemically amplified resists regarding line edge roughness were made.

Finally in section 6 the PEB was treated mesoscopically while continuous development algorithms have been applied, thus combining continuous and mesoscopic models. In this framework a narrow-band *level set algorithm* for simulating the resist development was realized where an added curvature term is investigated for its effectiveness in modelling line edge roughness. The further part then deals with a benchmark where the various development algorithms (fast marching, level set and mesoscopic development) were combined with the mesoscopic PEB to simulate LER in contact holes where a comparison with experimental data is made.

4.2. Numerical Solution

The fast marching algorithm developed was described 1999 in detail in [33]. It determines the arrival times of a front depending on the underlying velocity function. The propagation velocity itself is here given by the Mack rate equation, which transforms the local

inhibitor concentration into development rates. Note that this approach holds not for arbitrary velocity functions as for a unique solution of the arrival times $T(x, y, z)$ the velocity function must always be positive. Otherwise multiple arrival times could be assigned to a single point as the front moves forward and backward in space. For the resist dissolution this approximation can be made and is quite common in todays lithography simulators. The problem can be solved numerically for arbitrary positive velocity functions. Therefore $T(x, y, z)$ needs to be approximated on a grid divided into lattice points $T_{i,j,k}$ with spacing $\Delta x,\ \Delta y,\ \Delta z$ to solve for

$$|\nabla T| = 1/F \tag{4.1}$$

For simplicity consider the grid dimension to be of size $i, j, k \in \{1, .., N\}$. Each point $T_{i,j,k}$ describes the arrival time of the front which needs to be determined. As a first example a simple case will be discussed. Consider the lattice point $T_{i,j,k}$, which needs to be calculated, with the arrival time of the front at $T_{i-1,j,k}$ known. Then the quadratic equation

$$(\frac{(T_{i,j,k} - T_{i-1,j,k})}{\Delta x})^2 = 1/F_{i,j,k}^2 \tag{4.2}$$

needs to be solved for the condition $T_{i,j,k} \geq T_{i-1,j,k}$, and Δx being the lattice spacing. By this approach $|\nabla T| = 1/F$ was approximated on a numerical grid, with an error value of order $O(\Delta x)$. If more than one neighbour is known above equation needs to be calculated for all different known pairs and for each combination of forward/backward, left/right, and up/down pair. For example looking at the case of 2 known nearest neighbours (n.n.) in 3D, the following conditions could be possible as shown in Fig. 4.1.

For example picking the condition shown in Fig. 4.2 the quadratic equation would yield

$$(\frac{(T_{i,j,k} - T_{i-1,j,k})}{\Delta x})^2 + (\frac{(T_{i,j,k} - T_{i,j,k-1})}{\Delta z})^2 = 1/F_{i,j,k}^2 \tag{4.3}$$

where Δx and Δz denote the lattice spacing. For the numerical computation the quadratic equation is rearranged into the form $aT_{i,j,k}^2 + bT_{i,j,k} + c = 0$, with a,b,c being

$$a = \frac{1}{\Delta x^2} + \frac{1}{\Delta z^2} \tag{4.4}$$

$$b = -2(\frac{T_{i-1,j,k}}{\Delta x^2} + \frac{T_{i,j,k-1}}{\Delta z^2}) \tag{4.5}$$

$$c = \frac{T_{i-1,j,k}^2}{\Delta x^2} + \frac{T_{i,j,k-1}^2}{\Delta z^2} - \frac{1}{F_{i,j,k}^2} \tag{4.6}$$

and being solved for $T_{i,j,k}$. Of all possible solution (in this example, for each combination of a single known value, and for the solution of the 2 known values) the minimum solution is accepted which satisfies the condition $T \geq \max T_{known}$ where T_{known} are the known n.n. values[1]. Including 3 or more possible known values this sums up to a total of 26 conditions

[1] Note that opposing known values are not allowed for being solved as two terms in the quadratic equation. Instead they must be considered as a case of two single known n.n.

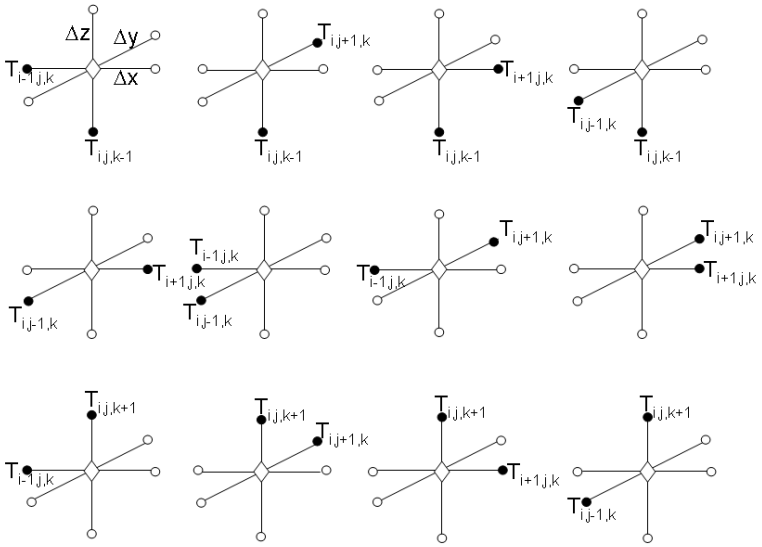

Figure 4.1.: Possible combination of two known nearest neighbours where the square in the center denotes the unknown lattice point $T_{i,j,k}$ which needs to be determined. Also denoted by black circles are for each case the known nearest neighbours with lattice indices. The white circles are unknown lattice points.

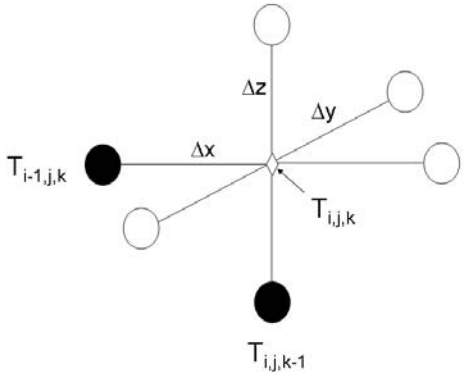

Figure 4.2.: An example for the numerical implementation of the fast marching approach. The front arrival times at $T_{i-1,j,k}$ and $T_{i,j,k-1}$ are known which is denoted by black circles. The front arrival time at $T_{i,j,k}$ needs to be determined. The other remaining nearest neighbours are unknown displayed by white circles. Also shown are the lattice spacings $\Delta x, \Delta y, \Delta z$.

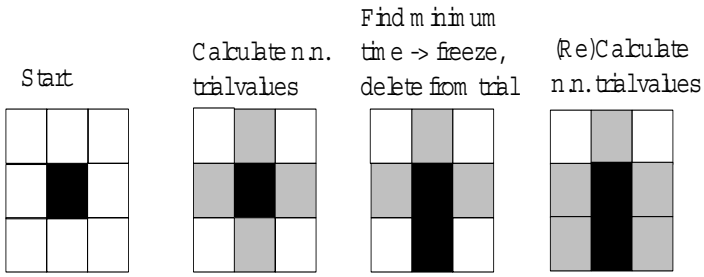

Figure 4.3.: Propagation of the solution by the fast marching method. White cells denote far values, grey trial values and black known values.

which must be checked during each computation step: 6 single known values, 12 for two known values, 8 for three or more known values. This needs to be done for every lattice point.

4.3. Performance

Normally several sweeps throughout the whole lattice are necessary to obtain the final solution when updating the grid after each iteration. A much faster convergence can be achieved. Therefore it is crucial to consider the causality principle. This, together with a rearrangement of the lattice points in a heap structure, will lead to a convergence within $O(N^3 \log(N))$ as the front runs across every lattice point only once and therefore only needs one iteration over the whole grid. This approach is the fast marching method.

4.4. Causality

The causality principle states that in the case of positive velocity functions no point with smaller arrival times is affected by points with larger arrival times. This means that it is possible to expand a solution outwards from the point of minimum time. The algorithm then consists of a simple scheme shown in Fig. 4.3 for a few iterations:

1. Find point of minimum time
2. Delete from trial values and add to known values
3. Recalculate nearest neighbours based on known values. If not part of trial values, add. Then continue at 1.

The only limiting factor of this scheme is to find the point of minimum time after each iteration. To overcome this problem the lattice can be arranged in a heap structure with

the point of minimum time at top. After each step, the top of the heap is chopped off and the heap structure rearranged. Therefore updated trial values are shifted within the heap to retain its structure, which takes only amount of $O(2)$ labour, and new trial values are inserted in the appropriate nodes, with a maximum time spend of order $O(\log(M))$ for a heap of size M. This is shown schematically in Fig. 4.4.

Numerically the heap exists within a large list, where each value in the list is properly arranged such that $\lceil n/2 \rceil - 1, n \in \{0, ..., M_{node}\}$, where M_{node} is the number of nodes, leads to the upper node and $2n+1, 2n+2$ to the left and right branches of the lower node.

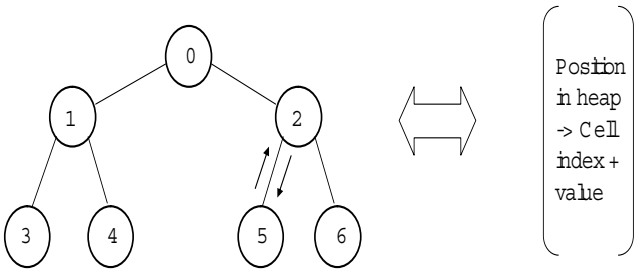

Figure 4.4.: The heap structure. The cell times are arranged in a binary tree with the point of minimum time on top. By storing back pointers in a matrix the position of a cell in a heap can be tracked. When e.g. the cell in position 5 changes its trial value such that it is smaller than the one in the node above, a sift up process takes place, restoring the heap.

4.5. Benchmark

The previously explained and developed algorithm was benchmarked against a different algorithm for front propagation based on a level set approach where a toolbox developed for Matlab by I. M. Mitchell was used [77]. As a first test a linear velocity function $F(x) = x$ in 1D was used such that

$$T(x) = \int_{x_1}^{x_2} 1/F(x)\ dx \tag{4.7}$$

$$T(x) = \log(x_2) - \log(x_1) \tag{4.8}$$

where $x_1 = 10\ nm$ at $t = 0s$ and $x_2 = 90\ nm$ such that the resulting analytical solution is $log(90) \sim 4.4998$. The results are displayed in Fig. 4.5. As can be seen the algorithm approximates the analytical solution well and converges for increasing resolution. Another test for a more complicated velocity function, now being $F(x) = 1 + \sin^2(ax)$, where $a = 180/\pi$, with the analytical solution

$$T(x) = \int_{x_1}^{x_2} 1/F(x)\ dx \tag{4.9}$$

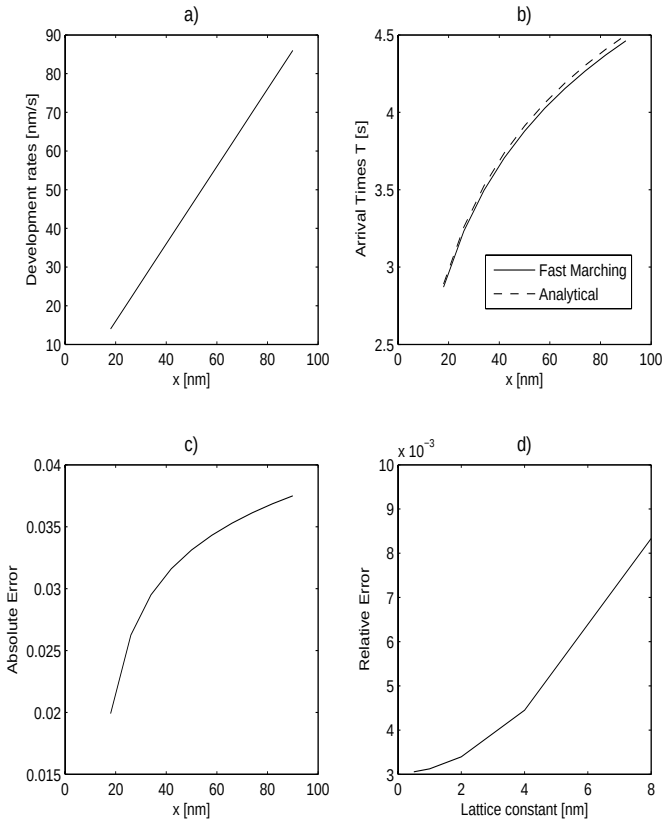

Figure 4.5.: The results for the 1D benchmark for a linear velocity function $F(x) = x$ are shown. In a) the linear velocity function can be seen. In b) the resulting arrival times as calculated by the fast marching algorithm compared to the analytical solution are shown for a lattice constant of 8 nm. In c) the total error between both solutions is displayed for the same lattice constant. In d) the relative error now for different lattice constants can be seen.

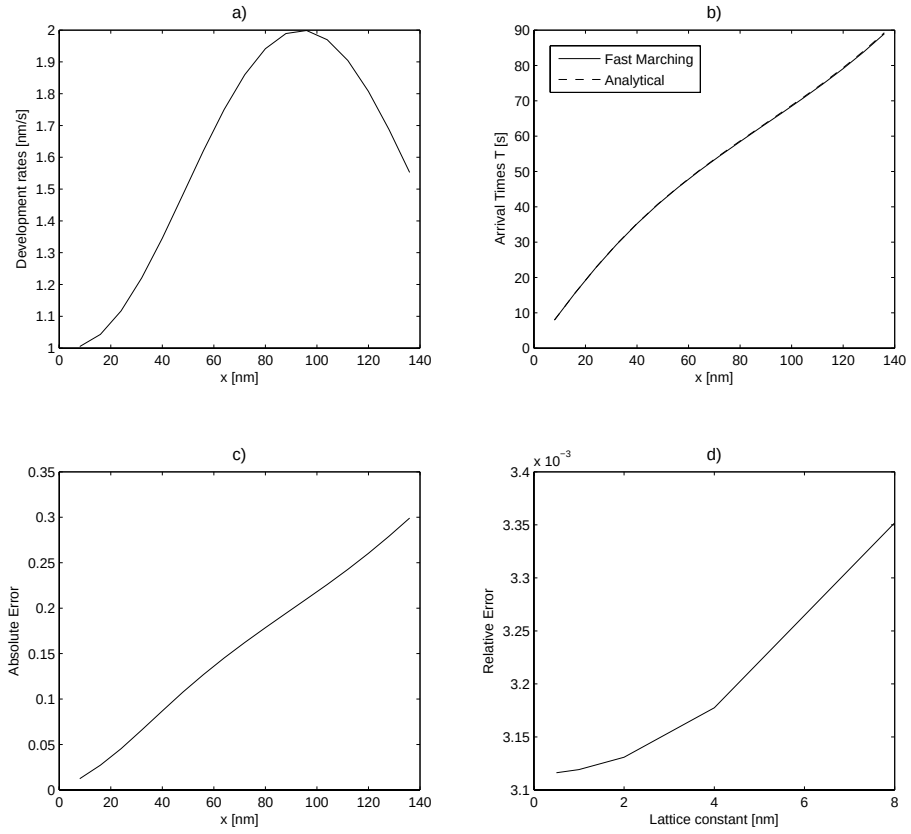

Figure 4.6.: The results for the 1D benchmark for $F(x) = 1 + \sin^2(ax)$ are shown. In a) the velocity function can be seen. In b) the resulting arrival times as calculated by the fast marching algorithm compared to the analytical solution are shown for a lattice constant of 8 nm. In c) the total error between both solutions is displayed for the same lattice constant. In d) the relative error now for different lattice constants can be seen.

$$T(x) \quad = \quad \left[\frac{1}{2\sqrt{2}} \arcsin\left(\frac{3\sin^2(ax) - 1}{\sin^2(ax) + 1}\right) \right]_{x_1}^{x_2} \tag{4.10}$$

was performed for the fast marching algorithm with $x_1 = 0\ nm$ at $t = 0s$ and $x_2 = 140\ nm$. The results are shown in Fig. 4.6 where similar results as for the previous test case can be observed.

To check the level set toolbox from Mitchell et al. the same benchmark for $F(x) = x$ was performed. Therefore the function $\Phi(x, y, t)$ which embeddes the zero level set needs to be properly initialized such that $\nabla\Phi = 1$. This ensures that as the level set function Φ is propagated in time the actual zero level set always corresponds to the correct arrival time t. The resulting function is shown in Fig. 4.7 for $t = 0s$. As time now increases the zero level set propagates forward which is displayed in Fig. 4.8. As for the solution of the partial differential equation the solver implemented in Matlab was used, the time steps

were chosen automatically such that the solution exactly converged towards the analytical value.

After the convergence has been checked for the $1D$ case the final benchmark on a full 3D contact hole has been performed. Here no analytical solution exists such that both algorithms were compared to each other. The initial aerial image intensity and inhibitor concentration, as well as the Mack parameters for development were the same as already shown in Fig. 3.2, Fig. 3.3 and Fig. 3.4 in section 3.1 and 3.2. The resolution was set to 2 nm along the resist plane and to 10 nm for the z-direction. The final 3D profile for the fast marching solution is displayed in Fig. 4.9. To compare with the results from the level set toolbox the difference between both final profiles was calculated divided by the mean circumference of the contact hole. The obtained mean error is shown in Fig. 4.10 for the cuts through the different heights in z. As can be seen the maximum mean error is 0.27 nm at a resolution of 2 nm along the resist plane. This shows a very good convergence. For higher accuracy the resolution must be increased.

4.6. New single layer resist process

The above explained fast marching algorithm was combined with an already existing in-house software to determine the aerial image after exposure and the inhibitor concentration after the post-exposure bake. The modules can be easily addressed independently of each other. This led to an investigation of a possible new double exposure process which until today can not be modelled with commercially available software. The need for double exposure processes arises from printing smaller feature sizes. For the current dry exposure tools minimum feature size for dense arrays is at approximately 130 nm pitch for $k1 = 0.3$, $NA = 0.93$ and $\lambda = 193$ nm. To go below this limit either immersion lithography [78] or double lithography must be utilized [79]. The main advantage for double lithography results from extending the current lifetime of dry exposure tools. In this context a possible new double exposure process which would need a specially designed resist was investigated. Therefore the resist is first exposed with a periodic line space pattern, after which a post-exposure bake is applied. Usually a development step would now follow to dissolve the resist in the unprotected regions. Instead, first a neutralization treatment is applied where acid and base are allowed to diffuse for $30s$ at low temperatures such that no deprotection occurs, followed by a second exposure where the pattern is shifted by one half of the period of the mask pattern. After the second post-exposure bake the profile is dissolved. The main advantage of this double exposure process results from the fact that the wafer is only once coated with resist, therefore being a new single layer resist process, where line space pattern with critical dimensions much smaller than the original mask pitch could be created. While the aerial image intensity of both exposures adds up to a constant, the nonlinear processes inside the resist are utilized to create a

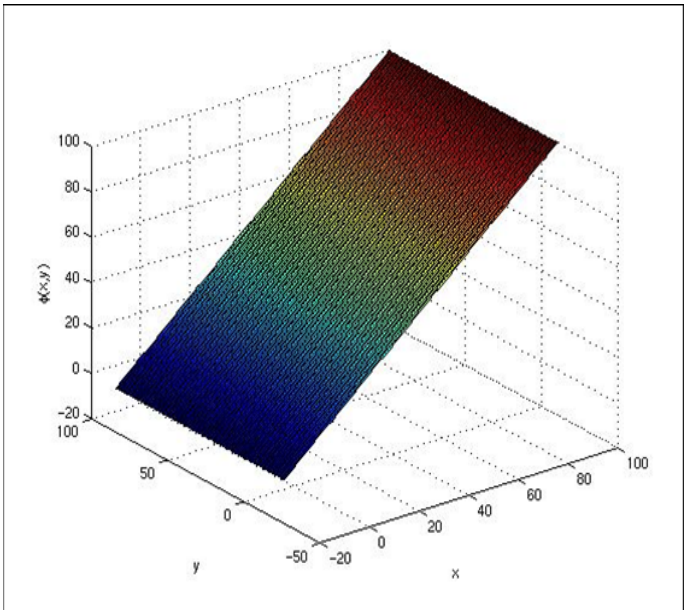

Figure 4.7.: Level set function $\Phi(x, y)$ at $t = 0s$

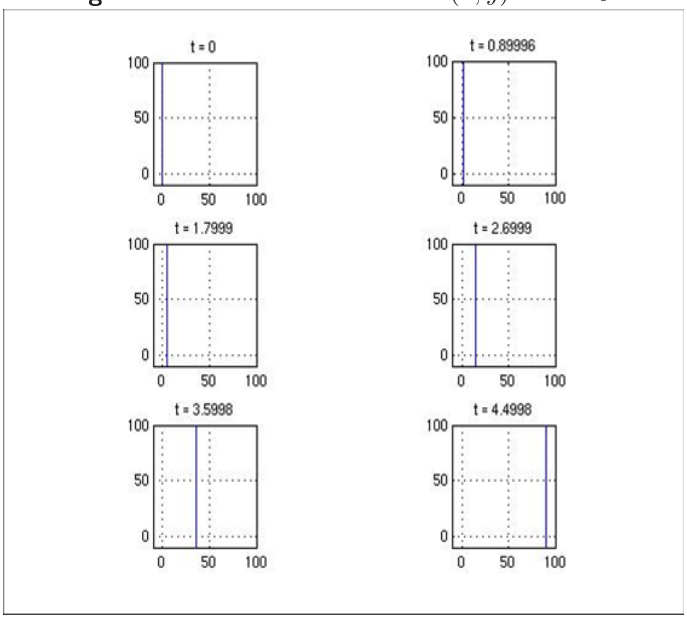

Figure 4.8.: Here the position of the zero level set is displayed which moves forward with increasing time according to the linear velocity function $F(x) = x$.

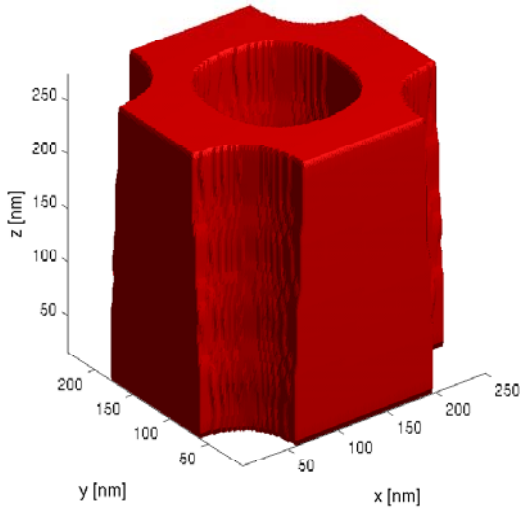

Figure 4.9.: Final 3D contact hole after fast marching development

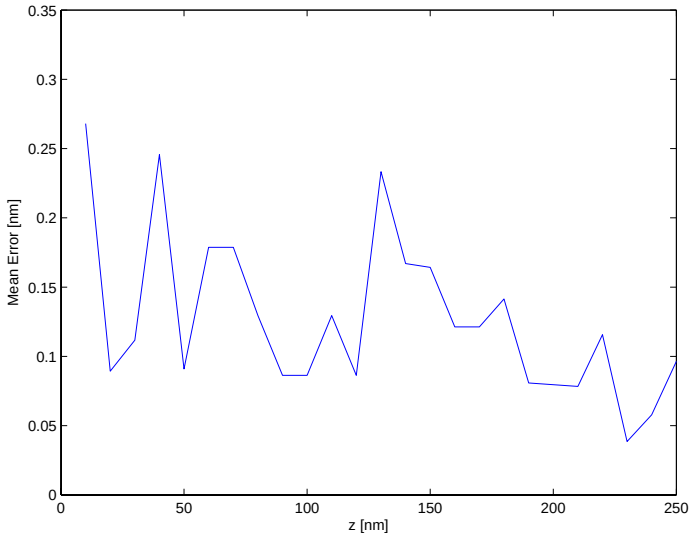

Figure 4.10.: Differences between the level set and the fast marching solution in terms of a mean error for cuts at different resist heights z. The mean error is defined by calculating the difference between both solutions divided by the circumference of the printed contact hole.

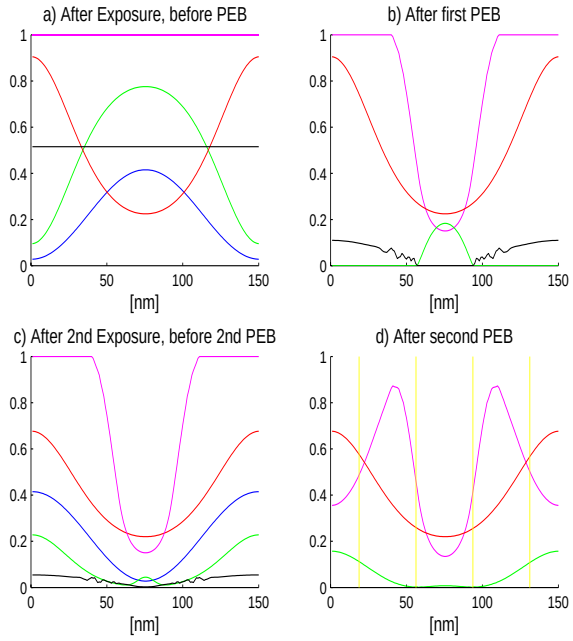

Figure 4.11.: The different concentrations inside the resist top for a cut through the line for the proposed single layer resist process. The different colours represent: blue = intensity, red = photoacid generator, green = acid, black = base and magenta = inhibitor. In d) the yellow lines represent the target CD value of 37.5 nm with a resulting periodicity or pitch of 75 nm.

final pattern. For the exposure a half-tone phase shifting mask with 6% transmission in the phase shifting regions was used, with $CD = 70\ nm$ and a space of 80 nm, such that the resulting pitch is 150 nm. The resist has a large acid conversion efficiency of $DillC = 0.1\ cm^2/mJ$, together with a high level of normalized base concentration of 0.51. Furthermore $k_1 = 0.0697561/s, k_2 = 0, k_3 = 0$ and $k_4 = 50\ 1/s$ where only first order reactions are used. Diffusion lengths are $D_A = 10\ nm$ and $D_B = 50\ nm$. The line formation can be explained when looking at Fig. 4.11. After the first PEB the inhibitors in the centre region are dissolved. After applying the neutralization treatment to acid and base the final base concentration is levelled, and acid concentration in the centre region is slightly reduced. After the second exposure new acid is generated at the edges, which deprotect the resist after the final second PEB step. The resulting inhibitor concentration has now distinct peaks which after applying a development with $m_{th} = 0.45$ results in the desired equal line space formation of $CD = 37.5\ nm$. Note that this resulting CD value is much below the usually possible optically resolvable feature size of a dry exposure tool. To investigate a possible process window the displacement of the lines must be taken into account. As the first and second exposure doses vary, the lines are not printed at the desired position, but due to the relative change of does values shift either towards each other decreasing the space between them, or shift away from each other. The resulting overlapping process window for $\pm 10\%$ variation in printed target

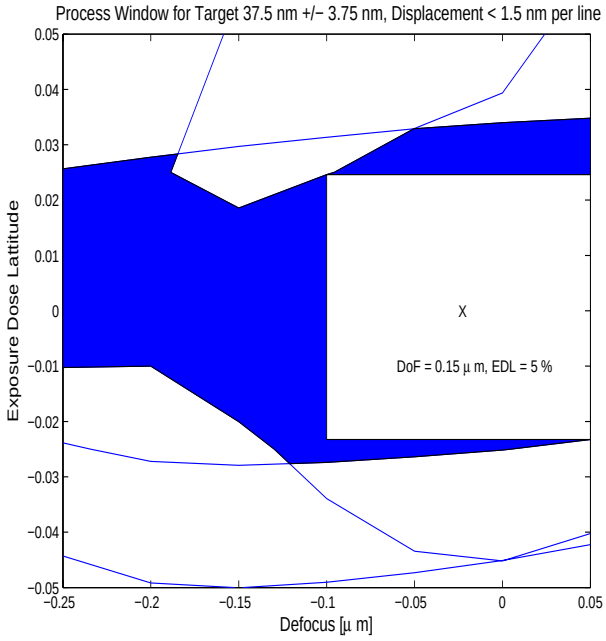

Figure 4.12.: Resulting overlapping process window for the proposed double exposure.

CD where line displacement of $< 1.5\ nm$ per line was considered is shown in Fig. 4.12. The working point is at $-0.025\ \mu m$ defocus, where the first dose is 36 mJ/cm^2 and the second dose is 7 mJ/cm^2, leading to a rectangular process window with an exposure dose lattitude (EDL) of 5% and a depth of focus (DoF) of 0.15 μm.

5. Mesoscopic Resist Simulation

While in the previous section a continuous approach to resist dissolution has been explained focus lies now on simulating on a mesoscopic scale. Therefore the photoresist must be divided into cells on which polymers are distributed. This can be achieved by performing a self-avoiding random walk on the lattice sites to create a polymer. Here also another method was investigated where polymers were simulated by molecular dynamics simulation [80].

5.1. Molecular Dynamics Simulation of Photoresist Polymers

For the molecular dynamics (MD) simulation the tool package MMTK was used [81]. The model polymer poly(4-tert-butoxycarbonyloxystyrene) (PBOCST) was added to the database and the simulation volume was prepared as shown in appendix D. PBOCST was chosen as it served as a standard polymer used in previously developed simulators, see e.g. [82]. In this polymer only protected or unprotected side chains occur where the unprotected side chains can be ionized during the development reaction. Here only a fully protected polymer was used for the MD simulation. Additional photoresist species such as PAGs, base and solvent where neglected. The PAG was assigned later for the post-exposure bake as additional cell contents. The position of the oxygen atom at the bottom of the benzole ring was taken as the reference coordinate which localizes the protection group. For the later development step the same coordinate was used for the position of the ionization reaction. A sketch of the molecule repeat unit is shown in Fig. 5.1. The resulting molecular volume is displayed in Fig. 5.2. More details on the MD simulation can be found in appendix D.

For the PEB and development simulation a lattice with cubic grid cells of length 0.8 nm was superposed to the periodically expanded MD box as depicted in Fig. 5.3, and protection groups corresponding to a polymer were assigned to the positions of the previously mentioned oxygen atom. Along the resist plane periodic boundary conditions were applied whereas at the resist bottom and top reflecting boundary conditions were used. Only for polymers created with the MD simulation those polymers extending the simulation volume at the top and bottom boundary were removed.

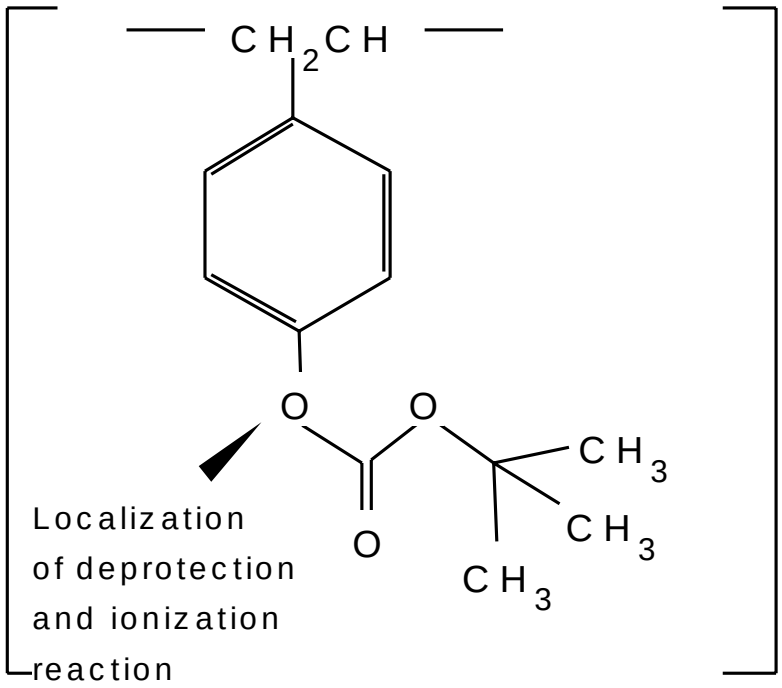

Figure 5.1.: The repeat unit of the modelled PBOCST where the oxygen atom is shown to which the deprotection reaction during PEB and the ionization reaction during development has been assigned.

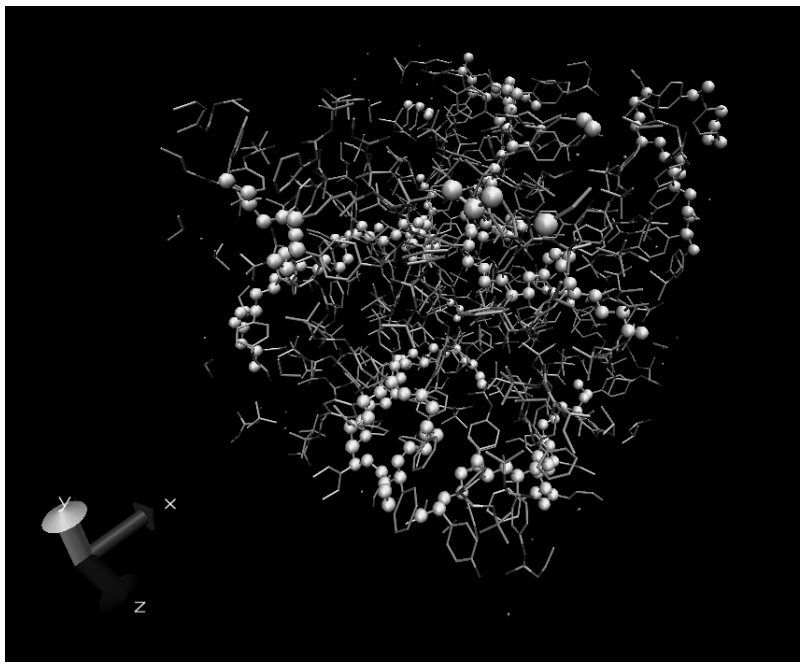

Figure 5.2.: The resulting compressed volume with a box length of 43 Å where 6 polymers with 40 repeat units each are displayed. The polymer backbone atoms are displayed as spheres. The figure was created with VMD [83].

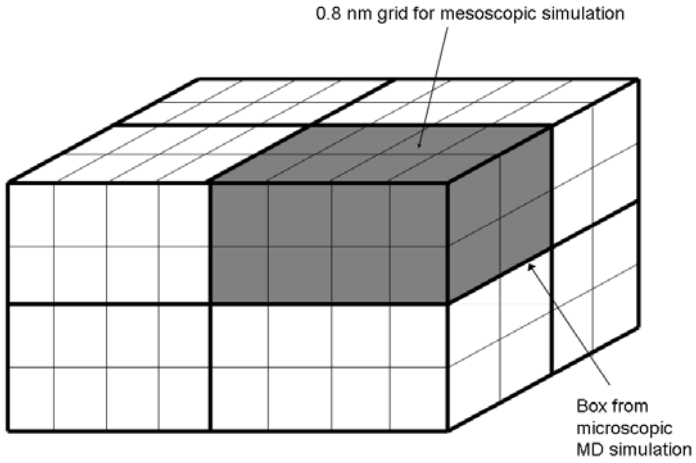

Figure 5.3.: Schematic demonstrating the different grids used. The MD simulations were performed off-lattice where the (periodic) MD volume is displayed in dark grey. Afterwards the corresponding repeat units were assigned on the basis of a 0.8 nm grid. If the previously described oxygen atom of the corresponding protection group was within a cell of length 0.8 nm the corresponding cell was assigned to the polymer.

5.2. Stochastic Post-exposure bake

The stochastic PEB simulation was developed in [84] based on a approach by [85]. Hereby the time evolution was determined by means of a Gillespie algorithm [23, 24] where its basic theory was already described in section 3.4. When looking at the PEB rate equation as defined in section 3.1 it can be solved by a Gillespie algorithm if the simulation volume is divided into cells. The total system consisting of cells with index $\nu = 1, ..., N$ can then be assumed to be in a defined state l. As explained previously in section 3.4 for a proper numerical implementation of a Markov process only the possibilities of leaving the actual system state need to be considered. The total transition rate of leaving state l, W_l, is then of the form

$$W_l = \sum_{l'} W_{\vec{x}_l -> \vec{x}'_l} \tag{5.1}$$

where l' denote the possible transition rates associated with possible new states as defined in equation (3.31). For the stochastic PEB simulation the transition rates of a single cell W^ν are given by

$$W^\nu = \frac{k_1 n_M^\nu n_A^\nu}{V} + k_3 n_A^\nu + \frac{k_4 n_A^\nu n_B^\nu}{V} + 2D n_A^\nu \left(\frac{1}{\Delta x^2} + \frac{1}{\Delta y^2} + \frac{1}{\Delta z^2}\right) \tag{5.2}$$

Here $n_M^\nu, n_A^\nu, n_B^\nu$ denote the number of inhibitor, acid and base molecules per cell. V is the cell volume while $\Delta x, \Delta y, \Delta z$ are the lattice constants along each direction. D is the diffusion coefficient. Here the first term on the right hand side corresponds to the inhibitor

deprotection rate, the second term to spontaneous acid loss, the third term to the acid-base neutralization rate. k_1, k_3, k_4 are the corresponding rate constants. The last term includes an acid diffusion rate either along the x,y or z-direction. The total transition rate of the system can be determined by summing up over all cell transition rates such that $W_l = \sum_\nu W^\nu$. The PEB algorithm in a simplified form then consists of

1. Compute time interval after which system change occurs by $\Delta t = -\frac{1}{W_l} \ln(1-r)$ where r is a random number in the interval $[0, 1)$.

2. Determine reacting cell ν by drawing a second random number R in the interval $(0, W_l]$ and subsequently subtract $R \leftarrow R - W^\nu$ for $\nu = 1, ..., N$ until $R < 0$.

3. Similarly, determine new random number R_2 in the interval $(0, W^\nu]$ and subtract $R_2 \leftarrow R_2 - reactions$ for the different types of reactions which occur within a cell until $R_2 < 0$ and update cell contents and transition rates within the cell accordingly.

4. Update time $t + \Delta t$. If $t < t_{max}$ where t_{max} is the maximum computation time, continue at 1. Otherwise stop.

This scheme runs until a maximum simulation time has been reached. To account for polymer removal some changes have been made. Additionally to the description in [84] the positions of the deprotection groups as resulting from the MD simulation are assigned to the cells of the superposed simulation lattice. In this way, different cells with a typical side length of $0.8nm$ contain a varying number of deprotection groups. Whenever an acid-catalyzed reaction occurred it was assigned to the repeat unit of the polymer in the corresponding cell which then was deprotected.

5.3. Stochastic Development

The stochastic development model applied is based on the "critical ionization model" [59, 82] plus the randomized polymer structure which is the outcome of the MD and PEB steps and will be explained in the following. During the previous post-exposure bake step some of the polymer sites remain protected with intact blocking groups. The other sites can be easily ionized in an aqueous base developer solution while the protected sites cannot. Thus, regarding the development process, the resist can be treated as a two level system with the polymer sites being in either of two states, ionized or neutral, while the protected sites do not participate directly in the reaction process. According to the "critical ionization model" (CI) a polymer is dissolved if a certain fraction of ionized sites is exceeded. Thus, although the protected sites are not involved directly in the reaction process they do have an influence as a strongly protected polymer is unlikely to meet the critical ionization criterion.

5.3.1. Stochastically simulating the chemical reactions of the CI model

The ionization reaction for a polymer of length M with k protected sites and l ionized sites reads

$$T_k H_{M-k-l} I_l \; + \; OH^- \rightleftharpoons T_k H_{M-k-l-1} I_{l+1} \; + \; H_2O \tag{5.3}$$

where T symbolizes the protected sites, H the non-protected sites, I the ionized sites, OH^- the reacting hydroxide group of the aqueous base, and H_2O the resulting water molecule after the ionization. If more than a certain fraction, the critical ionization level, of polymer sites are ionized, the polymer is dissolved. During the creation of the lattice a list is established which links the individual polymer sites to corresponding cells and vice versa. A second list contains labels that identify the polymer to which a single site belongs. As will be discussed later in more detail, the probability of a reaction of type (5.3) to occur in a lattice cell depends strongly on the cell contents. Thus, each cell is also assigned a "reactivity"which is a measure of this reaction probability. Then each cell is assigned to a "logarithmic class". Each such class collects cells with similar reactivities which is useful for speeding up the simulation. The links between lists and lattice are shown in Fig. 5.4.

Each cell contains information on the total number of ionized, neutral and blocked sites of the polymers which run through it. A system state n can be defined, which is characterized by the number of ionized and neutral sites in all of the cells that are in contact with the developer solution. However, not all of the cells are accessible to the developer solution. In order to account for this fact a "reaction front"collecting all accessible cells has to be incorporated into the simulation. Then the system state is solely characterized by the number of ionized and neutral sites in the cells belonging to the reaction front.

It is assumed that the diffusion of the developer into the resist takes place on time scales much shorter than the reaction time scales (which will be the case if always enough OH^- ions are existent at the resist boundary). In the beginning of the dissolution process, the reaction front contains lattice cells at the top of the resist down to a certain penetration depth. As the simulation time evolves, the reactions (5.3) take place and more and more polymers meet the critical ionization criterion and are removed. When a cell contains no more polymers, it is developed and all nearest neighbour cells become part of the reaction front. If one of the added cells is already empty additional nearest neighbours of the empty cell are added as well. Thus, by development of a cell content other (neighbouring) cells, which could not be reached before by the developer solution, then become accessible. Finally, at the end of the development, the cluster of non-developed lattice points still connected with the substrate is identified and displayed as the final resist profile. Note that for a sufficient percolation of the developer front an appropriate number of void cells must exist in the simulation region. While in other simulators this number can be adjusted

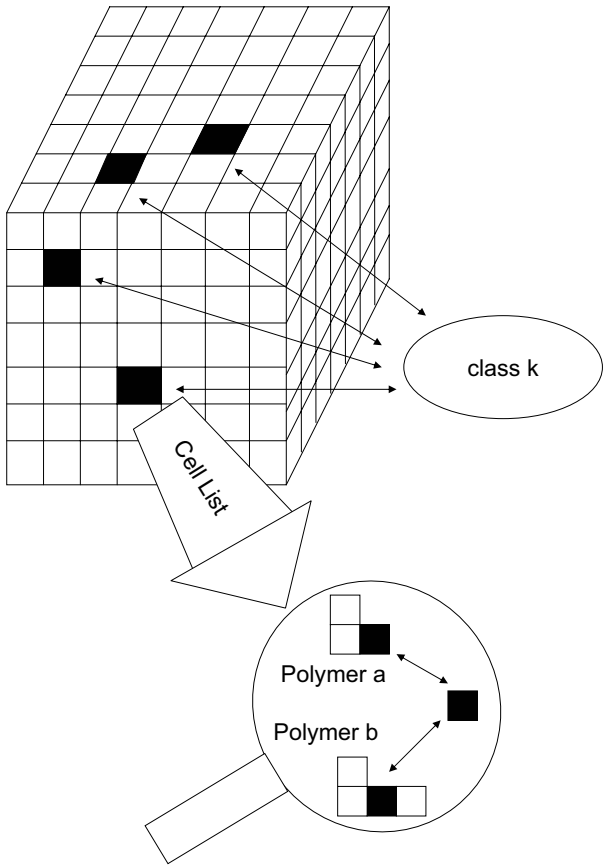

Figure 5.4.: Picture of the links between polymers, lattice cells and classes. Each cell is assigned to its appropriate logarithmic class. Every cell list contains information on the polymers it consists of and vice versa.

Reactivity	Meaning	Connection with system state n
W_n	Total reactivity of system state n	Defines system state n
$W_{I,n}$	Ionization reactivity of system state n	$W_n = W_{I,n} + W_{N,n}$
$W_{N,n}$	Neutralization reactivity of system state n	$W_n = W_{I,n} + W_{N,n}$
$w^{(k)}$	Total reactivity in class k	$W_n = \sum_k w^{(k)}$
w_ν	Total reactivity in cell ν	$w^{(k)} = \sum_{\nu \in (k)} w_\nu$
W_{I_p}	Ionization reactivity of all sites of polymer p in cell ν	$w_\nu = \sum_{p \in \nu}(W_{I_p} + W_{N_p})$
W_{N_p}	Neutralization reactivity of all sites of polymer p in cell ν	$w_\nu = \sum_{p \in \nu}(W_{I_p} + W_{N_p})$

Table 5.1.: All types of reactivities

it is here given by the combination of the resolution of the superlattice (here 0.8 nm) and the position of the oxygen atom resulting from the MD simulation.

5.3.2. System properties and cell reactivities

At each instant of time the system to be simulated is made up of all the reaction front cells which are in contact with the developer. If a lattice cell becomes empty because all of its cell content has been dissolved a new system is defined by the resulting new reaction front. The total size of the system to be simulated is defined by all cells which are contained within the reaction front. The only chance of this system to leave its state n and enter a new state n' is through an ionization or neutralization of a polymer site in a certain cell. To model this type of system the transition rates of the system are to be computed for each state n. It is assumed that the rate W_n with which the state n can be left is proportional to the number of accessible ionized and neutral sites, respectively,

$$W_n \sim k_1[OH]^- \ [H] + k_2[H_2O] \ [I] \tag{5.4}$$

where [H] and [I] denote the total numbers of accessible neutral and ionized sites and k_1 and k_2 are the rates for the forward and backward reactions in 5.4. Since the number of accessible ionized and neutral sites can be split into a sum over cells belonging to the reaction front

$$[H] = \sum_i [H]_i \ , \ [I] = \sum_i [I]_i \tag{5.5}$$

the overall rate W_n can be partitioned into a sum over cell reactivities

$$W_n = \sum_i (k_1[OH]^- \ [H]_i + k_2[H_2O] \ [I]_i) \equiv \sum_i w_i \tag{5.6}$$

were $w_i = k_1[OH]^- \ [H]_i + k_2[H_2O] \ [I]_i$ denotes the cell reactivity in lattice cell i. In this way each cell contributes to the total rate $W_n = \sum_{n'} W_{n \to n'} = \sum_i w_i = W_{I,n} + W_{N,n}$ which itself consists of the total ionization rate $W_{I,n}$ and the total neutralization rate $W_{N,n}$. The various types of reactivities are listed in Table 5.1.

The system can be modelled within the framework of Monte Carlo simulations [36]. Introducing the notation $p(n, t|n'')$ which describes the conditional probability for the system

to be found in state n at time t provided it had been in state n'' at time $t = 0$ the time evolution is governed by a master equation [86–88]

$$\frac{\partial}{\partial t}p(n,t|n'') = \sum_{n'}[W_{n'\to n}p(n',t|n'') - W_{n\to n'}p(n,t|n'')] \tag{5.7}$$

where $W_{n\to n'}$ denotes the transition rate from state n into the new state n'. In equ. (5.7) not only all possible transitions to leave the state n but also all transitions to enter the state n are taken into account. Thus the master equation is a balance equation describing the time evolution of the conditional probability by adding up all possible ways of entering or leaving the actual state n.

5.3.3. Simulating the Master equation

The master equation can be simulated with the Gillespie algorithm [23, 24]. Assuming the system to be in state n within a time interval $[t_0, t_1)$ the probability to be in any other state n' vanishes. For that time interval the master equation reduces to

$$\frac{\partial}{\partial t}p(n,t|n,t_0) = -W_n\ p(n,t|n,t_0) \tag{5.8}$$

As the system at time t_0 was in state n, (5.8) has to be solved with the initial condition $p(n,t_0|n,t_0) = 1$. This yields

$$p(n,t|n,t_0) = e^{-W_n\ (t-t_0)} \tag{5.9}$$

As this is the probability to find the system after the elapsed time $t - t_0$ in the state n, $1-p(n,t|n,t_0)$ is the probability to leave the state. Considering the case of an infinitesimal time interval $t_1 \le t \le t_1\ +\ dt$ in which a possible transition could occur this leads to a probability density

$$\begin{aligned}
\varrho(t_1)\ dt_1 &= (1 - p(n, t_1\ +\ dt_1|n,t_0)) && (5.10)\\
&- (1 - p(n,t_1|n,t_0)) \\
&= -dt_1\ \frac{d}{dt_1}e^{-W_n\ (t_1-t_0)} && (5.11)\\
&= dt_1\ W_n\ e^{-W_n\ (t_1-t_0)} && (5.12)
\end{aligned}$$

The transition time interval $\delta t = t_1 - t_0$, after which a change of system state takes place is thus exponentially distributed and can be modelled with a set of random numbers drawn from $W_n e^{-W_n\ \delta t}$. This property is a key feature of the Gillespie algorithm.

Exponentially distributed random numbers can be generated from uniformly distributed random numbers in the interval $[0, 1)$. Thus, the time interval after which a transition takes place can be simulated by

$$\delta t = -\frac{1}{W_n}\ \ln(1 - r) \tag{5.13}$$

where r is drawn from uniformly distributed random numbers. Therefore the algorithm in a simplified form consists of

1. Initialize: Create proper start distribution at $t = 0$ in state n'' and evaluate all reactivities of accessible cells, set up reaction front
2. Advance time step after (5.13)
3. Select randomly the next reacting cell among the accessible ones according to its reactivity weight
4. Choose reacting polymer inside the cell according to its reactivity weight
5. Choose reaction (either ionization or neutralization) according to its reactivity weight
6. Actualize reaction front and reactivities

The problem with this modelling approach is the computation time. As the complete list of accessible cells can be huge, it is very time consuming to search a reacting cell within this list. A faster alternative is described in the following.

5.3.4. Von Neumann Rejection

The von Neumann rejection scheme is particularly useful when dealing with a large number of cells out of which a possible reacting cell is to be drawn. The main mechanism is shown in Fig. 5.5 a.

Labelling of an accessible cell within the reaction front by x, a relative reaction probability can be assigned to each accessible cell

$$p(x) = \frac{w(x)}{W_n} \ , \ W_n = \sum_{x'} w(x') \tag{5.14}$$

Defining a "trial function" α

$$\alpha = \max_x \{p(x)\} \ \forall x \tag{5.15}$$

$$\tag{5.16}$$

the following von Neumann rejection scheme can be applied to draw a cell from $p(x)$ without searching the whole list:

1. Draw two random (uniformly distributed) numbers r_1, r_2 independent from each other and calculate,

$$x := N r_1 \tag{5.17}$$

$$y := \alpha r_2 \tag{5.18}$$

   where N is the length of the cell list

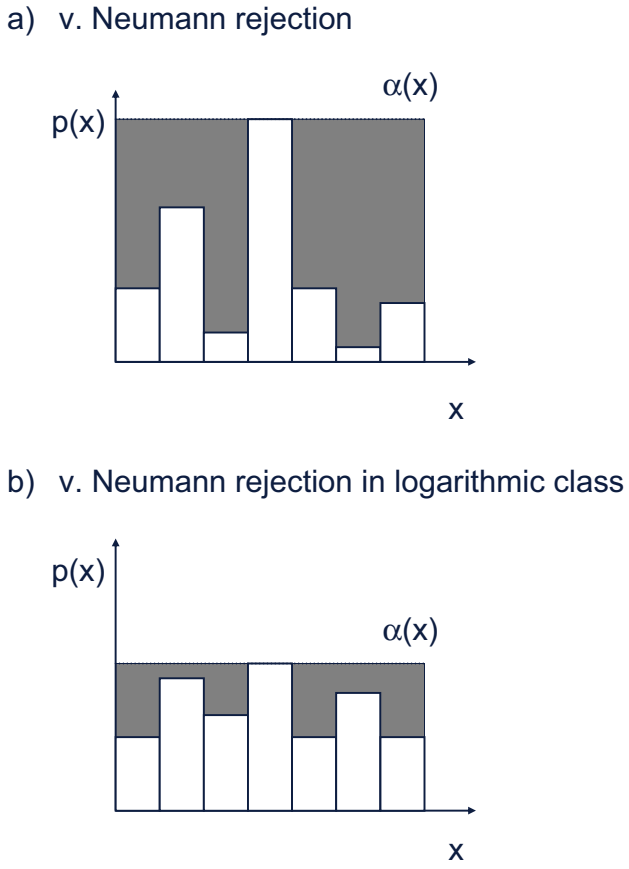

Figure 5.5.: a) Von Neumann rejection. The probability for a cell x to be selected is given by its reactivity weight $p(x) = \frac{w(x)}{\sum_{x'} p(x')}$. An accessible cell is drawn from its probability distribution $p(x)$ inside the reaction front by comparing the values of $p(x)$ and a (arbitrary) function $\alpha(x) \geq p(x)$, here assumed as $\alpha = \max_x \{p(x)\}$. The acceptance ratio is defined by the fraction of the areas below the two functions. The shaded area thus shows the relative probability of rejection. b) In a logarithmic class the reactivity between different cells in the same class differs only by a factor ≤ 2. The acceptance ratio is significantly increased.

2. Accept x as a possible reacting cell if

$$y \leq p(x) \tag{5.19}$$

otherwise reject it and go to 1.

Whether this cell selection algorithm works fast depends on the acceptance ratio ν given by

$$\nu := \frac{\int_0^1 \, dx \; p(x)}{\int_0^1 \, dx \; \alpha(x)} \tag{5.20}$$

Therefore the cell reactivities within the list should not differ too much from each other, and the cell list should be within reasonable length. Otherwise the acceptance ratio would be $\ll 50\%$. To overcome this problem logarithmic classes are implemented.

5.3.5. Logarithmic classes

A logarithmic class is build up of cell reactivities w_ν, where in each class the reactivity differs by a factor of less than 2, such that

$$2^{k-1} < w_\nu \leq 2^k \tag{5.21}$$

the class (k) contains all cells ν with reactivity w_ν which satisfy the above equation. The overall reactivity in class k is then defined as

$$w^{(k)} := \sum_{\nu \in (k)} w_\nu \tag{5.22}$$

with the total rate being

$$W_n = \sum_k w^{(k)} \tag{5.23}$$

It can be seen that by this sorting trick the acceptance ratio is significantly increased as shown in Fig. 5.5 b. When backpointers are introduced linking the cells and classes the computation time is reduced from L^2 to $L \log(L)$ where L describes the system size. As L is typically in the order of 10^5 the gain in computation efficiency is large.

5.3.6. The complete algorithm

A simplified flow diagram of the algorithm can be seen in Fig. 5.6.

The whole algorithm then consists of

1. Calculate time step after (5.13)

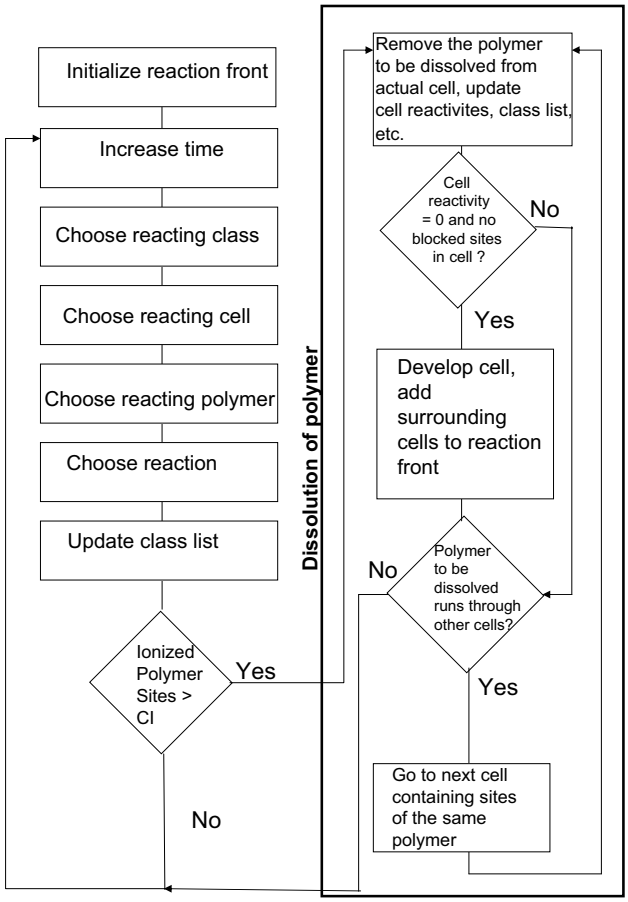

Figure 5.6.: Flow diagram of development algorithm

2. Choose reacting class k with uniformly distributed random number r_1 such that,

$$w_i = W_n r_1 \tag{5.24}$$

subtract subsequently from w_i the class reactivities $w^{(k)}$

$$w_i \leftarrow w_i - w^{(k)} \tag{5.25}$$

and accept class k if w_i becomes negative for the first time.

3. von Neumann rejection scheme: Select reacting cell by choosing random numbers r_2, r_3 independent from the first and compute

$$\nu = \lfloor m r_2 \rfloor + 1 \ , \ y = 2^k r_3 \tag{5.26}$$

where m denotes the number of cells in class ν and $\lfloor m r_2 \rfloor$ stands for the nearest integer smaller or equal $m r_2$. Accept if $y \leq w_\nu$. If cell ν is accepted, continue, otherwise repeat step three with new random numbers.

4. Select reacting polymer in cell ν with random number r_4 by subsequently subtracting polymer ionization reactivities W_{I_p} such that

$$c_i = w_\nu(k) \ r_4 \tag{5.27}$$

$$c_i \leftarrow c_i - W_{I_p} \ \forall \ p \in [1, .., q] \tag{5.28}$$

where q denotes the number of polymers in cell ν. Accept ionization in cell ν when $c_i \leq 0$ for the first time. If $c_i > 0$ after subtraction of all ionized q polymers, continue with subtracting neutralization reactivities W_{N_p} until $c_i \leq 0$, meaning that an ionized site in polymer p in cell ν is neutralized.

5. If a polymer is ionized and exceeds the critical ionization level, the polymer is removed from the lattice and its reacting sites removed from all lattice points it came across.

   a) If a lattice cell contains no more polymers, the lattice point is dissolved: Add surrounding cells to the reaction front, sort surrounding cells into appropriate logarithmic classes.

6. Actualize cell reactivities, if necessary move cell into appropriate new class which satisfies (5.21).

5.4. Results: Resolution limitations in chemically amplified resists

To investigate the impact of acid diffusion length and PAG concentration on the final profile an aerial image with a rather high contrast of $c \approx 0.8$ was created where around 9%

Module	Name	Value
General	Resolution	0.8 nm
	Simulation Vol.	$120 \times 80 \times 88\ nm^3$
	PEB computation time	$\sim 60s$
	Development computation time	$\sim 12s$
PEB	Deprotection k1 $[nm^3/s]$	1.0
	Spontaneous acid-loss k2 [1/s]	0.0
	Acid-base neutr. k3 $[nm^3/s]$	3.0
	Diffusion coefficient $[nm^2/s]$	2.5
	PAG concentration $[1/nm^3]$	0.25-0.4
	Dill C $[cm^2/mJ]$	0.30
	Polymer size [r.u.]	10-60
Development	Ionization rate [1/s]	100
	Neutralization rate [1/s]	1
	Critical Ionization Level	50 %

Table 5.2.: PEB and development parameters

flare were added. An ideal aerial image with infinite resolution was not chosen in order to yield more realistic conditions. Although the flare level of current EUV tools is at $\sim 16\%$ around 8% are targeted for production [89] which is close to the value used here. The aerial image and continuous PAG concentration was calculated with the commercial Solid EUV software [22] where a 2D Kirchhoff approximation for a binary mask was used. The numerical aperture (NA) was set to 0.25, $\sigma = 0.6$ and $DillC = 0.30\ cm^2/mJ$ with circular illumination and a mask pitch of 120 nm for 60 nm lines. For all simulations the PEB time was set to 90 s and the development time to 30 s. A detailed list of the parameters varied during PEB and development is shown in Table 5.2. The resist dimensions are of 120nm width, 80nm length and 88nm height at a cell resolution of 0.8 nm such that 1.65 Mio. cells were used for the simulation. The obtained initial normalized PAG density averaged along the line compared to a continuous PAG density from Solid EUV is shown in Fig. 5.7 together with the normalized intensity. The initial PAG density is obtained by distributing the PAGs randomly over the whole simulation region where only one PAG molecule is allowed per cell. The continuous PAG concentration is then interpreted in terms of a survival probability per PAG molecule leading to a high survival probability in regions of low intensity and vice versa.

5.4.1. Performance

All calculations were carried out on a Linux 64Bit cluster on AMD Opteron 2.4 GHz processors. The computation time for the PEB was at around $60s$. A comparable continuous simulation at the same resolution with Solid EUV at 10 time steps yields $\sim 6\ s$. While for cell numbers ≤ 100000 the stochastic simulation time is comparable to a continuous simulation the computing time of the stochastic PEB increases for large cell numbers. This is mainly because of the many stochastic diffusion steps resulting due to the high spatial resolutions necessary for the development which slow down the algorithm considerably. A

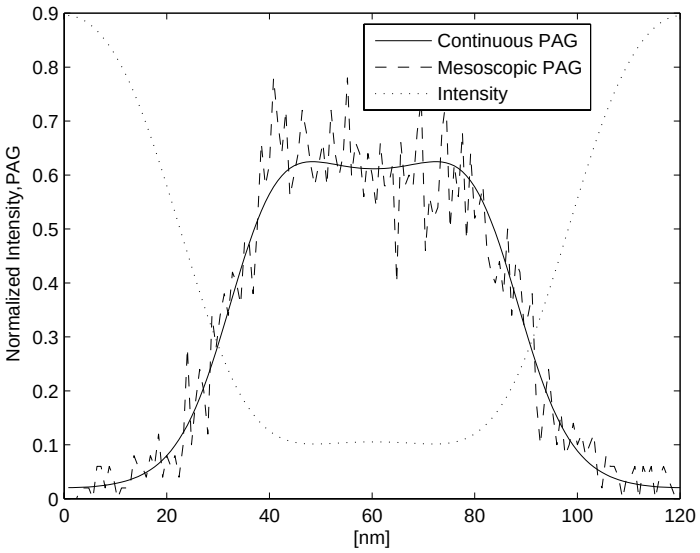

Figure 5.7.: Initial PAG density taken as input for the PEB simulation compared to the underlying continuous PAG distribution and the aerial image averaged along the line

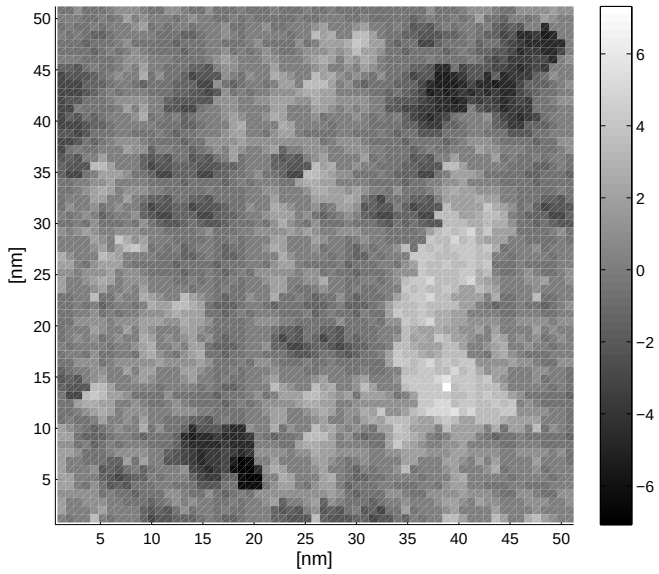

Figure 5.8.: Resulting height profile when fitting to a plane along the sidewall for MD based polymers of 40 r.u. size and $D = 2.5\ nm^2/s$. The colorbar shows the deviation from the plane in [nm].

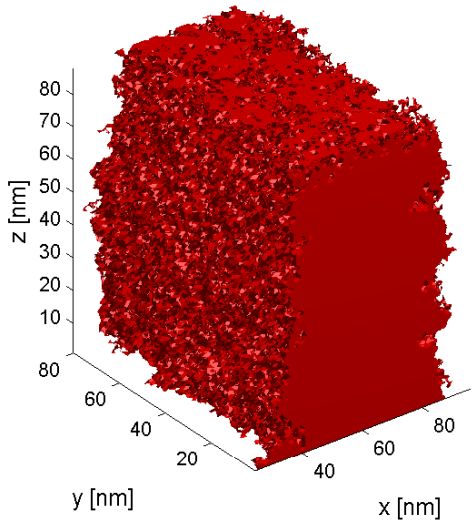

Figure 5.9.: Resulting 3D profile for 40 r.u. polymers and $D = 2.5\ nm^2/s$.

speed-up can be obtained by running the PEB on a lower resolution and then switch to a high resolution for the development. For the development step a simulation took around $12s$ and is within a factor 3 when compared to the $\sim 4\ s$ computation time of a continuous development. Here the benefit of using logarithmic classes is visible. We conclude that the mesoscopic model is with a total computation time of $\sim 70\ s$ for 1.65 Mio. cells suitable for resist calculations.

5.4.2. Roughness evaluation

The roughness has been analyzed by fitting to a plane along the resist sidewall as shown in Fig. 5.8 where only points between a resist height of 11 nm to 62 nm were considered. A full 3D profile is shown in Fig. 5.9. The standard deviation σ was determined by calculating the height-height correlation function in 2D

$$C(\vec{r}) =< (z(\vec{x}) - \bar{z})\ (z(\vec{x} + \vec{r}) - \bar{z}) >_{\vec{x}} \tag{5.29}$$

following the approaches in [48, 50, 51, 90, 91]. Here $\vec{x}$ is the position vector in the plane of the sidewall and $z(\vec{x})$ is the distance normal to the sidewall. $\bar{z}$ is the mean value. The brackets stand for averaging over all position vectors $\vec{x}$. The obtained 2D correlation function was then averaged over all azimutal positions to obtain C(r) depending only on the radius value $r = \|\vec{r}\|$. Note that per definition $C(0) = \sigma^2$. Similar, the height-difference correlation function for determining correlation lengths and critical exponent is defined by

$$H(\vec{r}) =< (z(\vec{x}) - z(\vec{x} + \vec{r}))^2 >_{\vec{x}} \tag{5.30}$$

Its average over all azimutal positions was computed from $C(r)$ by $H(r) = 2(C(0) - C(r))$. Note that the saturation value of $H(r)$ corresponds to $2\sigma^2$ and scales as $H \sim r^{2\alpha}$ if $r < l_c$ where α is the critical exponent describing the scaling behaviour of the sidewall roughness and l_c is the correlation length. This implies that an increase of the critical exponent α also results in larger local height differences.

5.4.3. Impact of polymer size at constant photoacid generator and constant diffusion

We start by considering the case of a high PAG concentration of 13 % and no base, thus the sidewall roughness is only limited by polymer size and diffusion length. Due to the high PAG concentration and the high CI level of 50% the resist is in an acid saturated regime where lowering the diffusion length results in more resist loss. First the dose was fixed at 16 mJ/cm^2 such that the amount of acid generated was kept constant. The CD of the resulting line varies for the different polymer lengths as resist solubility is changed which was already reported in [68]. To obtain a similar range of CD values for the different polymer generation methods some parameters for polymers distributed by a self-avoiding random walk had to be changed. The k_1 value was set to 0.9 nm^3/s and the CI value to 60%. Furthermore D was set to 2.5 nm^2/s for MD based polymers and to 3.0 nm^2/s for polymers distributed by a self-avoiding random walk, thus an offset between the different diffusion coefficients of 0.5 nm^2/s was applied. The reason for the major differences between the two polymer generation methods is the distribution of void cells. The void cells are distributed periodically for the case of the MD generated polymers and at random for polymers generated by a self-avoiding random walk. As will be seen later this also affects the critical exponents and correlation lengths. The CD here increases for increased polymer r.u. as resist solubility is changed. As the developer percolates through the resist larger polymers are not as easily enclosed as smaller ones leading to an offset between 10 $r.u.$ and 60 $r.u.$ polymers of around 8 nm for self-avoiding random walk polymers which yields 46 $nm < CD < 54$ nm for increasing r.u., and similar 42 $nm < CD < 58$ nm for MD based polymers. The difference of the resist solubility for varying the polymer repeat unit between both polymer generation methods arises from the fact that the mean spacing for the MD based void cells is larger than for the randomly distributed polymers which affects developer diffusion. All 3σ values for the different repeat units for the polymers are shown in Fig. 5.10. Note that for each point an average over 10 simulations was used. As can be seen lower MW polymers with 20-30 repeat units show the best performance where the lowest 3σ value found in our simulation corresponds to 5.3 nm for the MD generated polymers and 6.0 nm for polymers generated by the self-avoiding random walk. For larger polymers roughness increases which was observed in [68, 92]. To explain the increase in roughness for very low MW polymers the degree of ionization (DoI) per polymer, i.e. the ratio of ionized groups per polymer over the number of repeat units, must be taken into

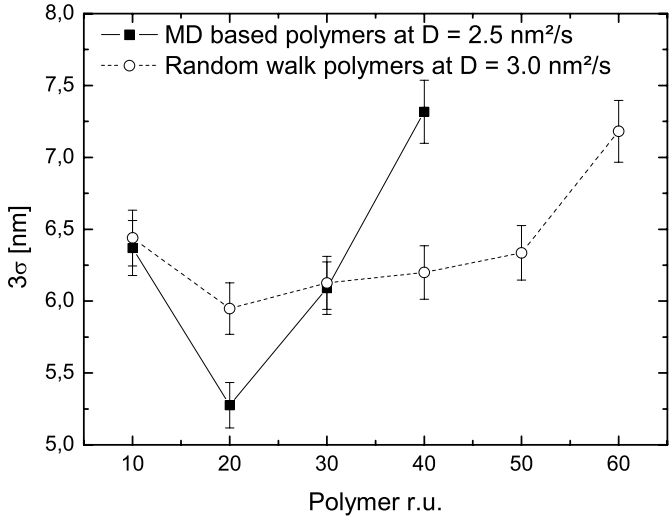

Figure 5.10.: Resulting sidewall roughness for both polymer generation methods

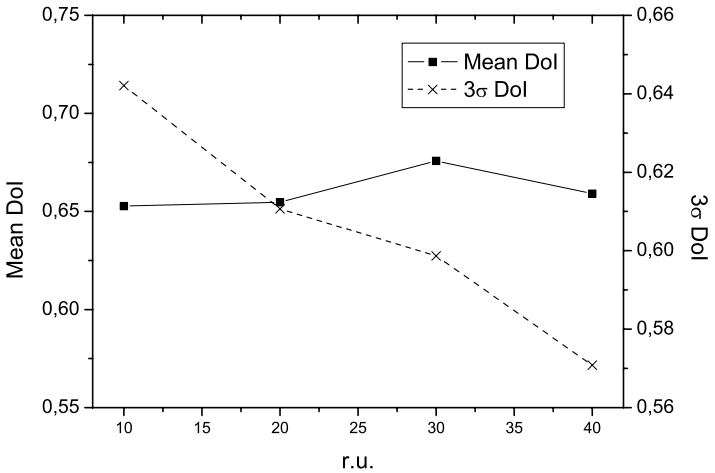

Figure 5.11.: Average degree of ionization (DoI) and number fluctuations for the whole simulation region are displayed for $D = 2.5\ nm^2/s$ for polymers generated with MD simulations. The results were averaged over 10 simulations. As can be observed the DoI remains approximately constant while number fluctuations increase for shorter polymers.

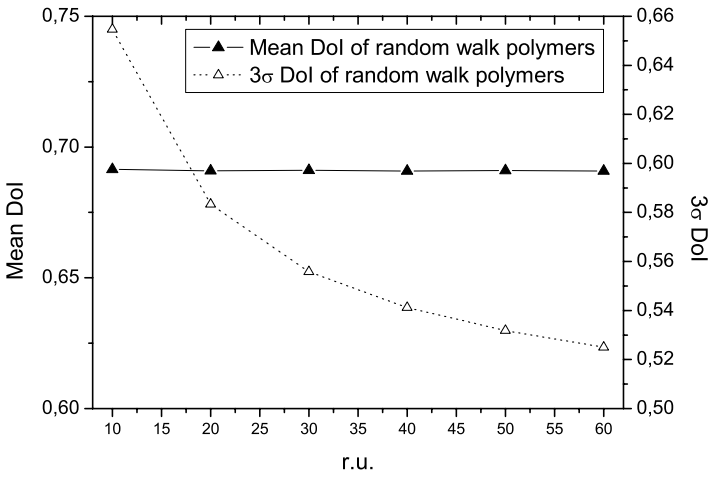

Figure 5.12.: Average degree of ionization (DoI) and number fluctuations for the whole simulation region are displayed for $D = 3.0\ nm^2/s$ for polymers generated with a random walk. The results were averaged over 10 simulations. An increase in the number fluctuations can be observed aswell with an even larger increase for shorter polymers.

account. While the mean DoI per polymer is approximately independent on the polymer length, the local fluctuations of the DoI is not. The reason being that longer polymers average over more polymer sites and therefore smooth out the number fluctuations. This is depicted in Fig. 5.11 for the MD generated polymers and in Fig. 5.12 for self-avoiding random walk polymers. Here the DoI for the whole simulation region (line and space) was calculated. As can be observed the average DoI remains approximately constant while its standard deviation 3σ *DoI* (i.e. the number fluctuations of ionized sites) increases for smaller polymers. The increase for the different polymer generation methods varies. For the MD based polymers it is linear, while for the random walk polymers a larger increase for shorter polymers occurs. However, both methods lead to a trade off for reducing LER between decreasing the polymer grain size at the resist edge by lowering MW and minimization of statistical fluctuations by increasing MW. A similar increase in LER for polymers $\leq 50\ r.u.$ for the case of chemically amplified resists was found in [68]. While in general our simulation results agree with [68] when using the same polymer distribution by a self-avoiding random walk, differences in the magnitude of the LER and exact shape of the curves are most probably related to the different aerial image and polymer matrix used. In [68] an ideal aerial image with a contrast of 1 was used with partially protected polymers where the fraction of void cells f_V was explicitly set to $f_V = 0.10$. In the present work the fully protected polymer structure and f_V are either fixed by MD and the 0.8 nm superlattice and vary slightly for the different repeat units, namely $0.14 \leq f_V \leq 0.16$ for $10 \leq r.u. \leq 40$, or are fixed for the self-avoiding random walk polymers to $f_V = 0.15$.

5.4.4. Critical exponents and correlation length

To further analyze the simulated roughness, correlation lengths l_c and critical exponents α have been calculated for for MD based polymers and for the self-avoiding random walk polymers. The two height-difference correlation functions for 10 and 40 r.u. MD based polymers are displayed in Fig. 5.13. As the local fluctuations of the inhibitor concentrations after PEB are approximately independent on the number of repeat units the following effects are mainly related to the polymer matrix and the development step. For the self-avoiding random walk polymers α remained close to 0.26 ± 0.02 while the correlation length was at around $8.5 \pm 1\ nm$ where no clear change of α or l_c for different repeat units could be observed. All extracted correlation lengths and critical exponents for the MD based polymers are shown in Fig. 5.14. As can be seen l_c increases for larger polymers which implies that long-range interactions of the system scale with polymer size. This results from the distribution of void cells which changes slightly for larger polymers. This changes the percolation of the developer through the resist matrix as longer polymers are not as easily enclosed by the developer as shorter ones. To understand the change of α the relation $H \sim r^{2\alpha}$,see section 5.4.3, leads to the conclusion that larger polymers result in increased local height differences. This is simply due to the dissolved particle size being larger. α then reduces with decreasing polymer size. However, for 10 r.u. polymers the number fluctuations prevail over the decreasing grain size at the resist edge which then is also visible by the increase of α.

All observed critical exponents in simulation are smaller than those normally found in experiments where α is in the range of 0.4 to 0.6 as found in [93]. This might result from several effects. First of all, a static polymer matrix was used here, but for real polymers also a reordering occurs during PEB which might affect acid diffusion and development as the distribution of void cells is changed. Also at the developer-resist interface various reorderings might occur which change the final profile and therefore α. Furthermore the polymer matrix used here is only an approximation to a real resist which consists of much more functional groups and additional contents such as solvent and base. Further effects might be related to the measurement method. Here a 3D profile is analyzed while most critical exponents are commonly measured with a top-down scanning electron microscope (SEM). In the SEM secondary electrons are utilized for detecting the feature, yielding a final 2D image where a large signal at edge features is detected (where more secondary electrons are created). Thus an averaging over the sidewall occurs. Also subsequent averaging filters applied during SEM profile evaluation might change roughness. Finally even for measurements with an atomic force microscope effects from tip convolution can affect critical exponents.

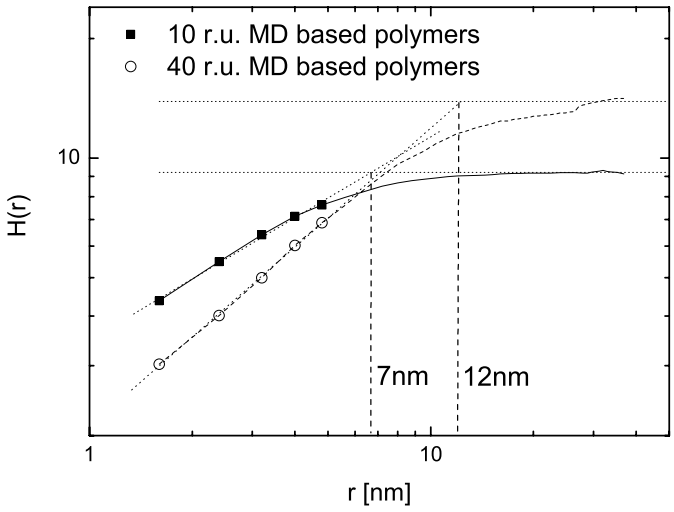

Figure 5.13.: Height-difference correlation functions for 10 and 40 r.u. MD based polymers are shown. The increase in correlation length from 7 nm to 12 nm for large polymers is visible.

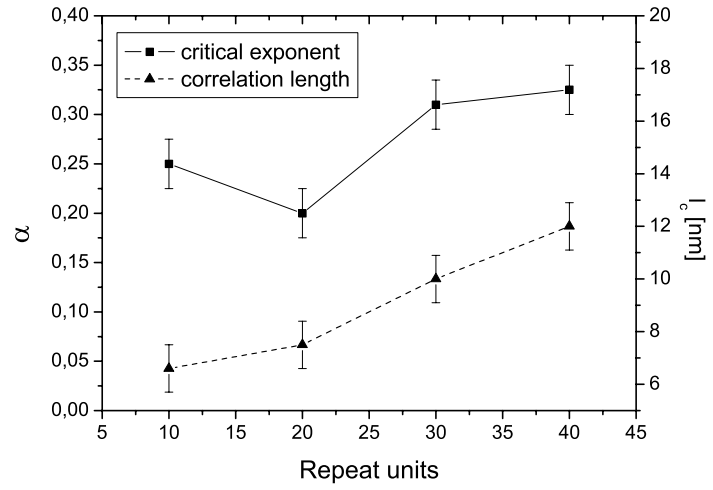

Figure 5.14.: Correlation length l_c and critical exponent α for all repeat units of the MD based polymers for $D = 2.5\ nm^2/s$ are shown. The correlation length decreases for smaller polymers. The critical exponent decreases as well for smaller polymers whereas for 10 r.u. an increase can be observed.

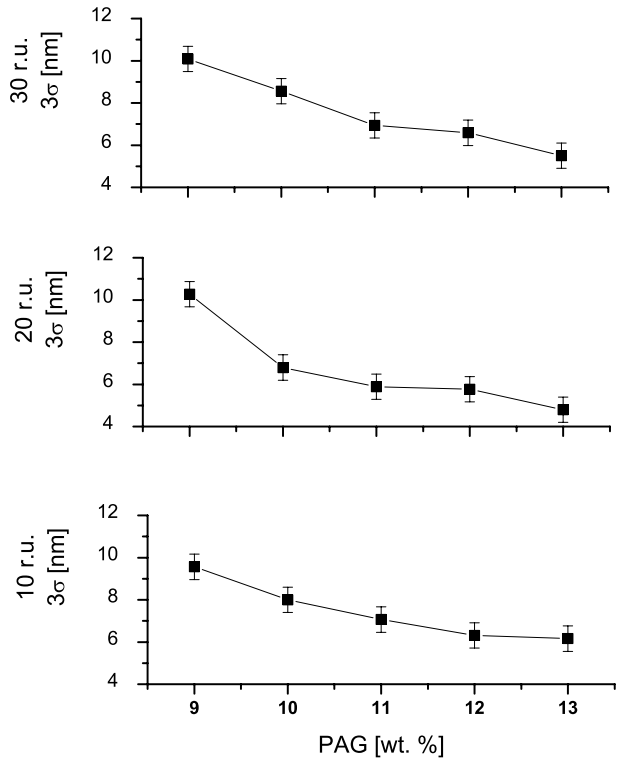

Figure 5.15.: Sidewall roughness 3σ as a function of increasing polymer size and PAG concentration for $D = 2.25\ nm^2/s$.

5.4.5. Impact of PAG concentration at constant diffusion

As not only the polymer size and acid diffusion length influences the final roughness, the PAG concentration was varied from 9 % to 13 % for polymer lengths of 10 to 30 repeat units for the MD based polymers as shown in Fig. 5.15, now keeping the diffusion length constant at $D = 2.25\ nm^2/s$. The dose was properly adjusted to keep the amount of acid generated constant where the resulting target line width was $46 \pm 2\ nm$ for 10 r.u. polymers, $53 \pm 2\ nm$ for 20 and $55 \pm 2\ nm$ for 30 r.u. polymers. According to [84] lowering the PAG content introduces larger fluctuations in acid concentration. Thus in general an increase in PAG concentration results in lower roughness. This trend was confirmed by the simulation results.

5.4.6. Impact of inhibitor contrast on line edge roughness

To further investigate the impact of inhibitor contrast on line edge roughness the diffusion coefficient, now only considering the self avoiding random walk polymers, has been varied. As was already reported by Pawlowski et al. a change of inhibitor contrast will change LER. By varying here the diffusion coefficient when keeping the amount of acid generated constant this changes line width and by this also the inhibitor contrast at the later forming edge. The change of inhibitor concentration averaged along the line for the different diffusion coefficients is depicted in Fig. 5.16. As mentioned previously the resist is here acid saturated due to the high PAG concentration, large $k1$ value and large Dill C value, thus an increase in diffusion coefficient leads to a broader line. To compensate for the change in CD values when using different polymer lengths the fraction of void cells was now additionally varied from $f_V = 0.10$ for 10 r.u. polymers up to $f_V = 0.19$ for 60 r.u. polymers. By this the relative change in CD values could be reduced to about 4 nm compared to 8 nm before. The resulting LER values plotted over CD are shown in Fig. 5.17. The increase in LER can be observed as the inhibitor contrast changes at the later forming edge when the diffusion coefficient is reduced while the increase of LER for the different polymers is similar. For $D = 1.75\ nm^2/s$ the change in inhibitor concentration M_c in the region of edge formation as obtained from Fig. 5.16 is $M_c = 1.5\ \%/nm$, for $D = 2.5\ nm^2/s$ contrast is improved such that $M_c = 2.4\ \%/nm$ and for $D = 3.25\ nm^2/s$ it decreases again to $M_c = 1.7\ \%/nm$.

Also note that the critical ionization level was set to 0.6, thus corresponding to a critical inhibitor concentration of 0.4. But the line forms in a region of around 0.3. This effect results from the diffusion of the developer which cannot fully enclose polymers close to the critical ionization level as percolation is more and more difficult to achieve. Development therefore stops before reaching a line width as would be defined by the critical ionization level.

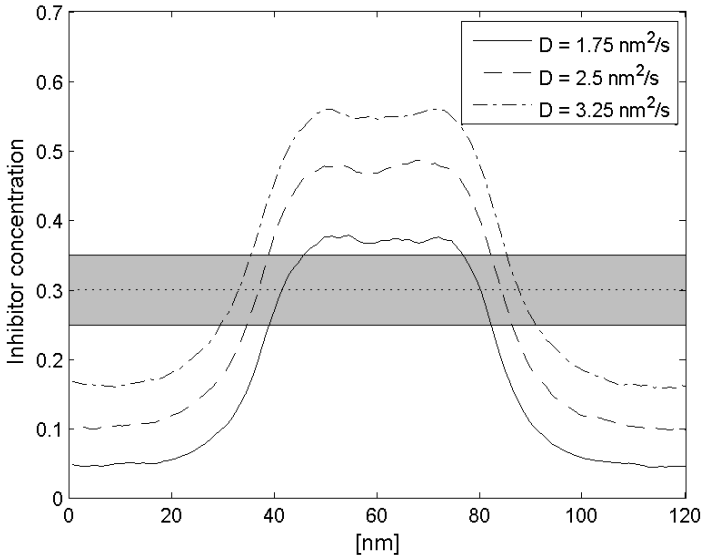

Figure 5.16.: Change in inhibitor concentration per polymer when varying the diffusion coefficient averaged along the line. Also the region of line formation around 0.3 ± 0.05 is shown. For increasing diffusion concentration the contrast in the region of line formation improves while it slightly degrades again for $D = 3.25\ nm^2/s$.

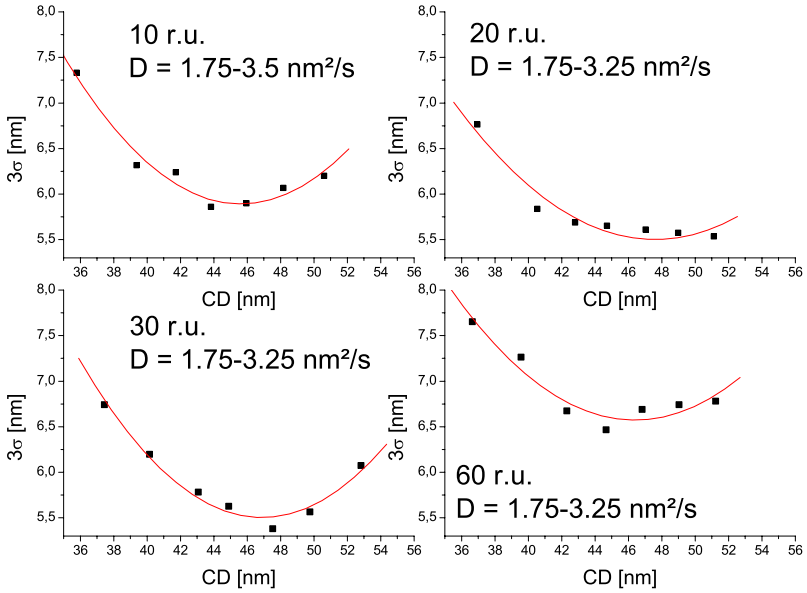

Figure 5.17.: Resulting LER values for the changing CDs.

5.4.7. Acid breakable polymers

The idea of acid breakable polymers was first introduced in 1987 by Frechet et al. [94] while recently attention has been drawn to these systems by Eschbaumer et al. [95] in 2003 where improvements in LER of up to 30 % have been found. Although high glass transition temperature and etch stability for these polymer platforms remain an issue our model was used to determine a theoretical potential in terms of LER. To model such a polymer it was allowed for the acid molecules to break a polymer in the simulation where a minimum polymer size can be defined which does not undergo any further scission reactions. For our simulations a lattice consisting of 60 r.u. polymers distributed by a self-avoiding random walk was chosen together with a minimum size after scission of 10 repeat units. The remaining parameters equal those from the previous section with a PAG concentration of 0.4 $1/nm^3$ and fixing the fraction of void cells again to $f_V = 0.15$, where now additionally the diffusion coefficient was varied between $D = 2.0\ nm^2/s$ to $D = 3.0\ nm^2/s$. Each polymer was allowed to undergo a scission reaction with a probability of $p = 0.2$ if a deprotection reaction occurred at the inhibitor site. The resulting line width for the main-chain scission polymers decreased by about 6 nm when compared to the 60 r.u. polymers due to the previously mentioned percolation effect of the developer. The y-averaged polymer size distribution together with the histogram of the number of polymers over polymer size is depicted in Fig. 5.18 and Fig. 5.19. The resulting 3σ values are shown in Fig. 5.20. As can be seen in Fig. 5.18 the polymer size is changing locally with a large area of long chain polymers present near the unexposed region. For larger diffusion lengths roughness increases for the 60 r.u. polymers. As the resist is in an acid-saturated regime as previously mentioned, and the amount of acid generated was kept constant, line width increases for larger diffusion coefficients. This degrades chemical contrast and by this increases roughness. However, the acid-breakable polymers perform much better for increasing diffusion coefficients and show a lower roughness than the 60 repeat units. At low diffusion lengths the acid concentration during PEB remains high close to the exposed-unexposed interface. This results in a large fraction of small (acid-broken) polymers at the interface in turn leading to large fluctuations of the DoI, i.e. large fluctuations of the relative number of ionized sites per polymer, see section 5.4. This causes increased LER.

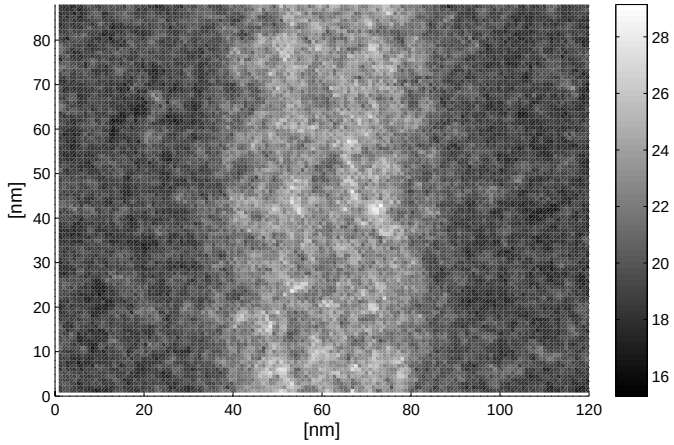

Figure 5.18.: The chain length at the mean centre of mass of the different polymers for a cross section through the line at $D = 3.0\ nm^2/s$. The result was averaged over the length of the line. The colorbar shows the number of repeat units.

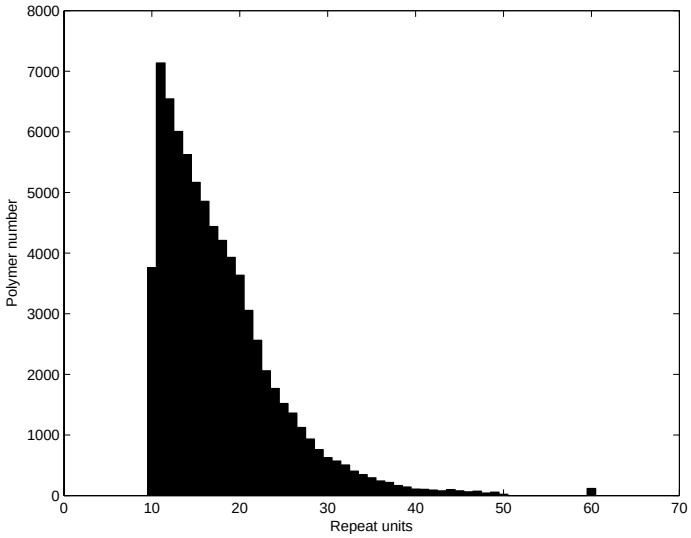

Figure 5.19.: The corresponding polymer size distribution of all polymers in the simulation region.

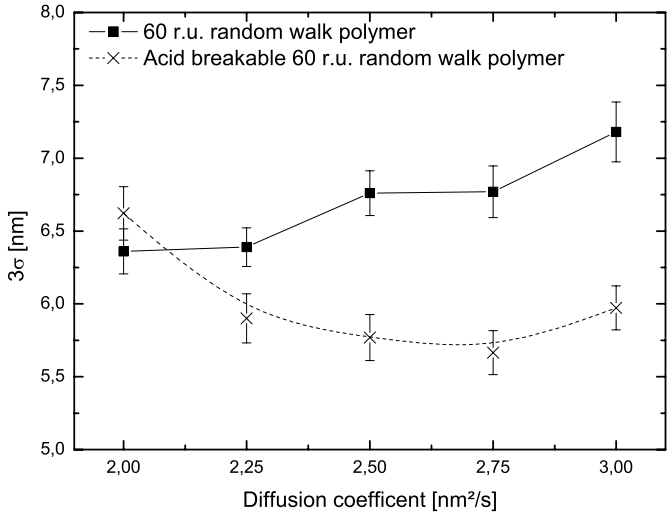

Figure 5.20.: Resulting sidewall roughness for the single r.u. polymer and the acid-breakable polymer is shown. The single 60 r.u. polymers yield a larger roughness value than the acid breakable polymers for larger diffusion lengths.

6. Combined continuous and mesoscopic models

The model described in section 5 is limited to resolving the polymer repeat units of a single polymer. To investigate a different approach the mesoscopic model was combined with a continuous development model neglecting polymers. Thereby the chemical diffusion and deprotection reactions within a cell during PEB are calculated for a fixed density of inhibitors, namely 3 inhibitors per nm^3, which are not assigned to polymers, and scaled appropriately for the resolution defined for simulation. Also the number of PAG, acid and base molecules inserted into a single cell is scaled according to the defined cell size. After PEB the obtained number of inhibitors is normalized to 1 such that the Mack rate equations can be used to calculate the development rates in each cell. These can then be used as input for a fast marching algorithm as described in section 4. This approach thereby follows the theory of a soluable site density model as proposed in [63].

Here also a different method based on a level set method was investigated. The reason was that in the level set approach it is possible to incorporate a curvature term which simulates surface reordering. This could be a different way of incorporating a reorder mechanism to achieve a better control over the magnitude of simulated roughness. As will be shown in the following the curvature term can be linked to fundamental polymer properties by starting with the Gibbs free energy and the chemical potential. From these starting point the curvature term can be associated with a surface tension and polymer properties such as the relaxation time used for defining a surface mobility can be explained.

As described earlier when dealing with percolation theory the resist can be described as a two phase system with chemical potentials μ_1 and μ_2 where regions below a certain inhibitor threshold are dissolved. This is depicted in Fig. 6.1. This leads to the following theory derived here for the first time for the case of resist dissolution. It is based on the equation which combines the Gibbs free energy of a system with the chemical potentials

$$\mu_i = \frac{\partial G(T, p, n_i)}{\partial n_i} \tag{6.1}$$

where T is the temperature, p is the pressure, and n_i is the number of particles in material type i. The Gibbs free energy G of a thermodynamic system is minimized when moving towards equilibrium. The derivation was found for the case of crystal growth in [96, 97].

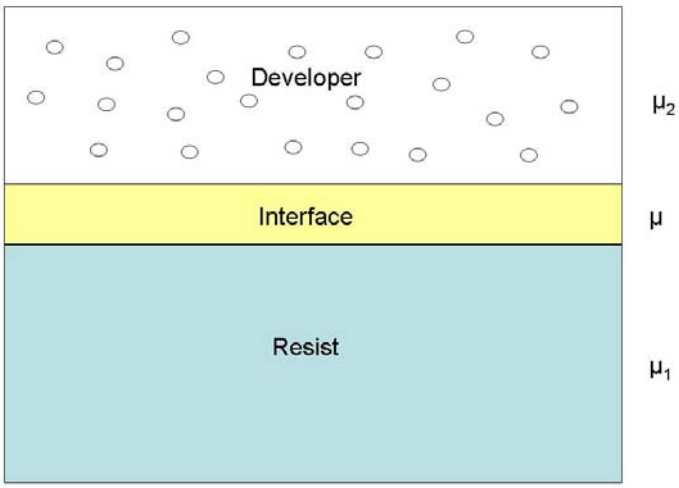

Figure 6.1.: Developer, interface and resist defined by the chemical potentials μ_2,μ and μ_1. At equilibrium the chemical potential of the interface region μ equals both the chemical potential of the resist and of the developer $\mu = \mu_1 = \mu_2$.

6.1. Interface reshaping without material loss

We start by considering an interface changing its shape without any material loss. When looking at time t at the interface $h(x, y, t)$ it is characterized by its total surface free energy

$$G = \int g(h_x, h_y)\ dx\ dy \tag{6.2}$$

where $g(h_x, h_y)$ is the surface free energy per projected area and the shorthand notation $h_x = \frac{\partial h}{\partial x}$,$h_y = \frac{\partial h}{\partial y}$ was used. Here x and y are global variables as shown for the one dimensional case in Fig. 6.2.

Close to equilibrium the chemical potential μ at the interface varies such that the surface free energy is minimized. The chemical potential is linked to the surface free energy and the geometrical shape of the interface. The definition of a mean polymer volume Ω leads to the equation for fixed particle number n

$$\Omega^{-1} \int h(x, y, t)\ dx\ dy = n \tag{6.3}$$

Furthermore the variation of G can be calculated

$$\delta G = \int \delta g(h_x, h_y)\ dx\ dy = \int (\frac{\partial g}{\partial h_x}\ \delta h_x\ +\ \frac{\partial g}{\partial h_y}\ \delta h_y)\ dx\ dy \tag{6.4}$$

As the chemical potential μ of the added or subtracted molecules is defined by equation (6.1) the free energy variation can also be expressed as $\delta G = \Delta\mu\ \delta n$, where $\Delta\mu$ is the chemical potential relative to the bulk phase. This leads to

$$\delta G = \Omega^{-1} \int (\mu - \mu_1)\ \delta h\ dx\ dy \tag{6.5}$$

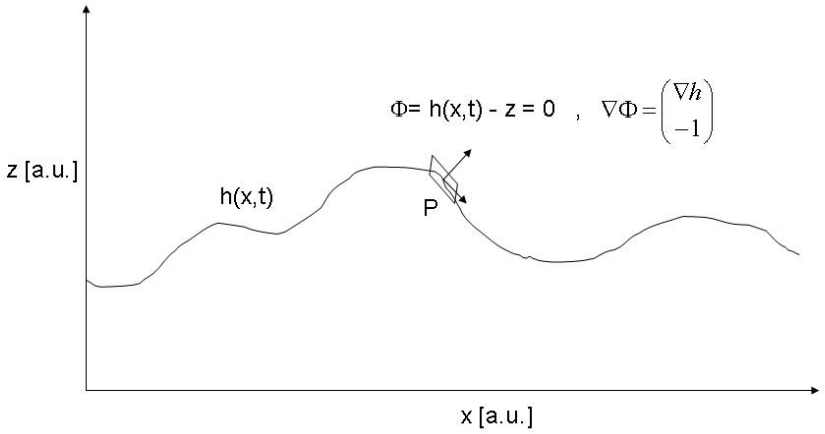

Figure 6.2.: Interface h(x,t). At point P also the surface normal and the surface element are shown. Additionally the description of the interface $h(x,t)$ within the level set framework is shown where $\Phi = h(x,t) - z$ such that the zero level set corresponds to $h(x,t)$.

Expression (6.5) and (6.4) can be equated. Note that the term $\mu - \mu_1$ defines the chemical potential relative to the bulk phase and the variation of the particle number δn is given by $\int \frac{\delta h \; dx \; dy}{\Omega}$. Taking the first variation with respect to h to be zero for h fixed at the endpoints [96, 97] and subsequent differentiation by parts gives

$$0 = \int dx \; dy \left(\frac{\partial g}{\partial h_x} \; \delta h_x \; + \; \frac{\partial g}{\partial h_y} \; \delta h_y - \Omega^{-1}(\mu - \mu_1) \; \delta h\right) \tag{6.6}$$

$$= - \int dx \; dy \left(\frac{\partial}{\partial x} \; \frac{\partial g}{\partial h_x} \; + \; \frac{\partial}{\partial y} \; \frac{\partial g}{\partial h_y} \; + \; \Omega^{-1}(\mu - \mu_1)\right) \; \delta h \tag{6.7}$$

Applying the chain rule[1] yields

$$0 = \int dx \; dy \left[\left(h_{xx} \; \frac{\partial^2 g}{\partial h_x^2} \; + \; 2h_{xy} \frac{\partial^2 g}{\partial h_x \; \partial h_y} \; + \; h_{yy} \; \frac{\partial^2 g}{\partial h_y^2}\right) + \frac{(\mu - \mu_1)}{\Omega}\right] \; \delta h \tag{6.8}$$

For the integral to vanish for arbitrary areas the integrand must be zero, thus

$$(\mu - \mu_1) = -\Omega \left(h_{xx} \; \frac{\partial^2 g}{\partial h_x^2} \; + \; 2h_{xy} \frac{\partial^2 g}{\partial h_x \; \partial h_y} \; + \; h_{yy} \; \frac{\partial^2 g}{\partial h_y^2}\right) \tag{6.9}$$

The surface free energy per projected area g and the surface free energy per area of the surface γ are connected by $g = \gamma\sqrt{1 + h_x^2 + h_y^2}$, see appendix E. For a constant and isotropic γ straightforward differentiation yields

$$(\mu - \mu_1) \; = \; -\Omega\gamma \frac{h_{xx}(1 + h_y^2) - 2h_{xy}h_x h_y + h_{yy}(1 + h_x^2)}{(1 + h_x^2 + h_y^2)^{\frac{3}{2}}} \tag{6.10}$$

$$= \; -\Omega\gamma\kappa \tag{6.11}$$

[1] e.g. $\frac{\partial h_x}{\partial x}\frac{\partial}{\partial h_x} + \frac{\partial h_y}{\partial x}\frac{\partial}{\partial h_y} = \frac{\partial}{\partial x}$

where $\kappa = \frac{h_{xx}(1+h_y^2)-2h_{xy}h_xh_y+h_{yy}(1+h_x^2)}{(1+h_x^2+h_y^2)^{\frac{3}{2}}}$ is the mean curvature of h. The mean curvature is defined as $\kappa = \frac{(\kappa_1+\kappa_2)}{2}$, where κ_1 and κ_2 denote the minimum and maximum of the local curvatures at a given point.

In the simplest approach the driving force for the surface evolution is proportional to the deviation of the chemical potential from its equilibrium values $\mu - \mu_1$. The proportionality constant which connects the propagation speed F_{curve} of the curved interface along its normal with the driving force is a surface mobility ε. A corresponding relaxation time was measured e.g. in [98]. Thus the propagation velocity is described by

$$F_{curve} = \varepsilon(\mu - \mu_1) = c\kappa \tag{6.12}$$

with a constant c.

6.2. Level-set approach

As we are concerned not only with the surface reordering mechanism but will later face the problem of tracking a developer surface moving through the resist, a more general equation for arbitrary surface evolution needs to be derived. This can be achieved by using a level-set approach where the function $h(x, y, t)$ is embedded into a higher dimensional function $\Phi(x, y, z, t)$ as the zero level-set [31]. Thus

$$Front \quad = \quad \{\ x, y, z \mid \Phi(x, y, z, t) = 0\ \} \tag{6.13}$$

This defines a front that needs not to be given by a (unique) function $z = h(x, y, t)$ but also holds in the more general case of an arbitrary surface, e.g. an ellipsoid which cannot globally be defined in the manner $z = h(x, y)$. Thus by the level-set approach it is possible to solve non-planar surfaces with non-unique parametrizations. Therefore the constraint for x, y to be local variables is no longer necessary. The time-evolution of the level set equation can be obtained by starting with

$$\Phi(\vec{\Gamma}(t), t) \quad = \quad 0\ , \tag{6.14}$$

$$\vec{\Gamma}(t) \quad = \quad \begin{pmatrix} x(t) \\ y(t) \\ z(t) \end{pmatrix} \tag{6.15}$$

Differentiation by the chain rule yields

$$\Phi_t \ + \ \nabla\Phi \cdot \vec{\Gamma}'(t) = 0 \tag{6.16}$$

Denoting by F the velocity in the outward normal direction $F = \vec{\Gamma}'(t) \cdot \vec{n}$, where $\vec{n} = \frac{\nabla\Phi}{|\nabla\Phi|}$ is the surface normal, yields

$$\Phi_t = -F\ |\nabla\Phi| \tag{6.17}$$

This equation is an initial value formulation of the surface evolution where only $\Phi(x, y, z, t = 0)$ and the velocity function $F(x, y, z)$ need to be defined for completely determining the time evolution of the surface.

For the resist development case the velocity function F is to include both contributions, the dissolution rate F_{diss} (as obtained from the Mack rate equations in section 3.2, there defined as v) responsible for resist development and the surface reordering contribution F_{curve} in equation (6.12),

$$F = F_{diss} + F_{curve} \tag{6.18}$$

$$= F_{diss} + c\,\kappa \tag{6.19}$$

where c is a constant. The mean curvature of the front κ is directly linked to the time evolution. An expression for the curvature in terms of the level-set function Φ needs now to be defined. In general the mean curvature is given by

$$\nabla \cdot \vec{n} = \kappa \tag{6.20}$$

with $\vec{n} = \frac{\nabla\Phi}{|\nabla\Phi|}$. This yields

$$\begin{aligned}\kappa = ((\Phi_{yy} + \Phi_{zz})\Phi_x^2 \; + \; (\Phi_{xx} + \Phi_{zz})\Phi_y^2 \; + \; (\Phi_{xx} + \Phi_{yy})\Phi_z^2 \\ - \; 2\Phi_x\Phi_y\Phi_{xy} \; - \; 2\Phi_x\Phi_z\Phi_{xz} \; - \; 2\Phi_y\Phi_z\Phi_{yz})/(\Phi_x^2 + \Phi_y^2 + \Phi_z^2)^{\frac{3}{2}}\end{aligned} \tag{6.21}$$

Expression (6.21) is the necessary link to propagate the time evolution of a curved developer-resist interface in the level-set framework.

6.3. Numerical implementation

For propagating the front in the level set framework an explicit Euler scheme with first order in space and time was used as found in [33]. Considering for simplicity the case of a convex velocity function for the one dimensional case, this scheme can be written as

$$\Phi_i^{n+1} = \Phi_i^n - \Delta t[\, \sqrt{max(D_i^{-x}, 0)^2 + min(D_i^{+x}, 0)^2}\; max(F_i, 0) \tag{6.22}$$

$$+ \sqrt{max(D_i^{+x}, 0)^2 + min(D_i^{-x}, 0)^2}\; min(F_i, 0) \; + c\,\kappa\,] \tag{6.23}$$

This equation needs several explanations. First, Φ_i^{n+1} is the level set function at time step $n+1$ at lattice point i. Φ_i^n is the level set function at lattice point i for the previous time step. Δt is the time step. This is depicted in Fig. 6.3. D_i^{-x} and D_i^{+x} are the discretization of the differential operators on the grid for the backward and forward differential operators. Therefore

$$D_i^{-x} := \frac{\Phi_i - \Phi_{i-1}}{\Delta x} \tag{6.24}$$

$$D_i^{+x} := \frac{\Phi_{i+1} - \Phi_i}{\Delta x} \tag{6.25}$$

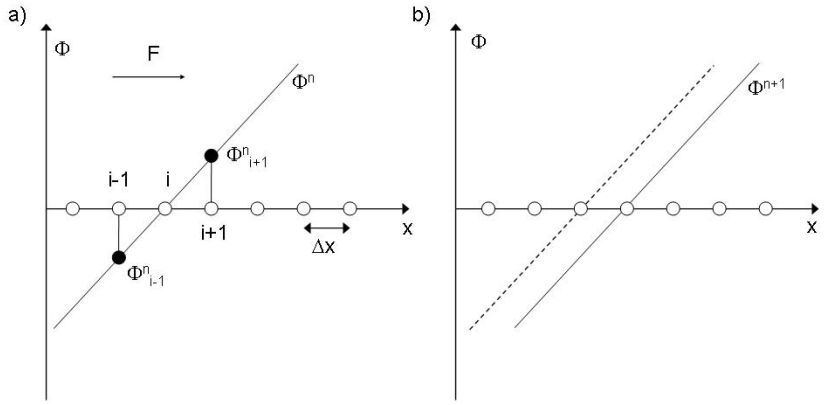

Figure 6.3.: The update of the level set function Φ for a positive velocity function is shown. In a) Φ^n_{i-1} and Φ^n_{i+1} is the level set function at lattice points $i-1$ and $i+1$. Also displayed is the positive velocity function F. In b) the updated level set function Φ^{n+1} for the next time step is shown compared to Φ^n as displayed by a dashed line.

where Δx is the lattice spacing. The reason for distinguishing between forward and backward differential operators lies in the subtle relationship for the solution of the level set equation for a positive or negative value of the velocity function F_i at lattice point i. For a positive velocity function information travels from left to right while it is vice versa for a negative velocity function. This means that for a correct update of Φ_i^{n+1}, D_i^{-x} will yield a positive value for the change of the level set function with respect to the previous lattice point $i-1$. At the same time D_i^{+x} will give a negative contribution such that $\sqrt{max(D_i^{-x},0)^2 + min(D_i^{+x},0)^2}\ max(F_i,0)$ will give the maximum (and correct) contribution to the solution while the second term $\sqrt{max(D_i^{+x},0)^2 + min(D_i^{-x},0)^2}\ min(F_i,0)$ will be zero. For a negative value of F_i this will be vice versa. The so obtained scheme can then run over all lattice points i to update the level set function Φ for the next time step. Also another property can be observed. For simulating the resist dissolution using the outcome of the mesoscopic PEB algorithm the velocity function F will be in general non-smooth and can lead to numerical instabilities. By adding a curvature term $c\,\kappa$ these instabilities are smoothed out. With the derivation in section 6.1 this term was linked to a surface reorder mechanism in terms of a change of the chemical potential of the resist-developer interface close to its equilibrium value.

Material	n	k
TARC	1.552	-0.02
BARC	1.591	-0.512
SiON	1.845	-0.542
Carbon hardmask	1.43	-0.35

Table 6.1.: Real and imaginary part of the complex refraction index $\widetilde{n} = n + ik$ for the different stack layers, namely the top antireflective coating (TARC), bottom antireflective coating (BARC), $SiON$ and the carbon hardmask.

6.3.1. Narrow Band scheme

To speed up computation the updating of the level set function needs not to be done for every lattice point which is very time consuming (especially for 3D simulations). Instead, updating Φ can be limited to regions close to the zero level set as found in [99, 100]. While the region inside the narrow band is updated, the zero level set will move to the borders of the narrow band as it propagates through the resist. Thus after a fixed amount of time the narrow band needs to be rebuild around the zero level set. Thereby a signed distance function $|\nabla\Phi| = 1$ must be maintained for correct propagation as otherwise the propagation time will not match with the zero level set. For reinitialization a fast marching scheme is used here. This was achieved by identifying the zero level set as a starting point for the fast marching scheme such that solving the equation $|\nabla T| = 1$ with $T = \Phi(x = 0, t)$ and a unity velocity function $F = 1$ from section 3.3.1 leads to the desired reinitialization. This reinitialization and rebuild of the narrow band is done after a fixed time interval has been exceeded which can be adjusted. This algorithm then leads to an improvement in computation time by a factor of ~ 10 when compared to a full solution on the grid but remains in the order of minutes for calculating the development step. Note that a fast marching algorithm solves the development step in lithography within seconds but fails to incorporate intrinsic geometric properties of the front like the front normal or curvature into propagation.

6.4. Results: Roughness simulation in contact holes

We start by defining the experimental settings. For the aerial image a half-tone phase shifting mask with 6 % transmission in the dark regions was used. The contact hole was of 130 nm width and 200 nm length with a pitch of 800 nm. Illumination settings were circular illumination with $\sigma = 0.5$ at $193nm$ exposure wavelength. The stack consisted of a carbon hardmask of thickness 200 nm, 60 nm of $SiON$, a bottom anti-reflective coating (BARC) of thickness 40 nm and a top anti-reflective coating (TARC) of thickness 32 nm. In between the BARC and TARC $240nm$ of resist were deposited with $n = 1.699$ and a Dill B value of 1.355. The refractive index and absorption constants n and k for the corresponding layers are displayed in table 6.1. For this type of process a calibrated

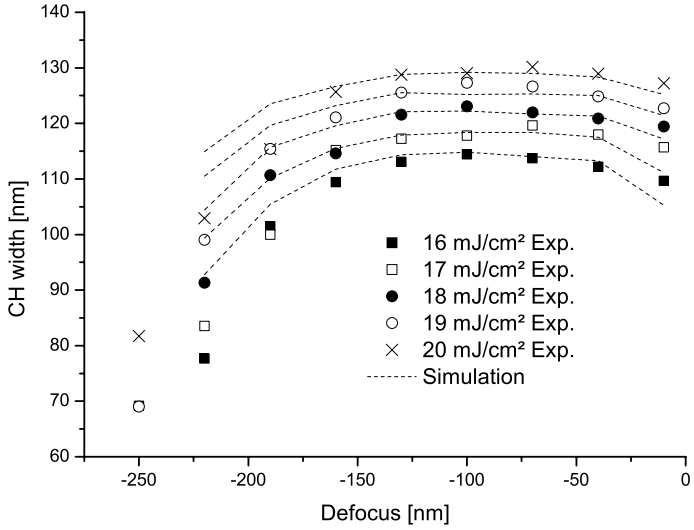

Figure 6.4.: Resulting contact hole (CH) width for the calibrated resist model from macroscopic simulation compared to experimental data.

Module	Name	Continuous	Mesoscopic
PEB	Deprotection k1 $[nm^3/s]$	0.01	0.01
	Spontaneous acid-loss k2 [1/s]	0.0	0.0
	Acid-base neutr. k3 $[nm^3/s]$	Fast ($>> k_1$)	10.0
	Acid diffusion coefficient $[nm^2/s]$	2.2	2.2
	PAG concentration $[1/nm^3]$	Normalized	0.3
	Dill C $[cm^2/mJ]$	0.3	0.3
	Base $[1/nm^3]$	0.06	0.06
	Base diffusion coefficient $[nm^2/s]$	50.0	50.0
Development	R_{max} $[nm/s]$	100	30
	R_{min} $[nm/s]$	0.04	0.01
	m_{th}	0.823	0.83
	n	28	15

Table 6.2.: PEB and development parameters for the macroscopic and mesoscopic model

model in the commercial software *Solid C* was available. The resulting *CD* regarding the contact hole width compared to experiment is shown in Fig. 6.4. To this model the following mesoscopic models are compared in terms of parameter settings. Also the resulting fit to the experimental data is discussed including the description of the measured line edge roughness.

6.4.1. Convergence of mesoscopic PEB with continuous simulation

To check whether the mesoscopic PEB simulation converges with the Solid model an average over 10 simulations in inhibitor concentration was calculated. The parameters for the PEB and development for the continuous model and the macroscopic model are displayed in Table 6.2. For the PEB the normalized parameters of the continuous model

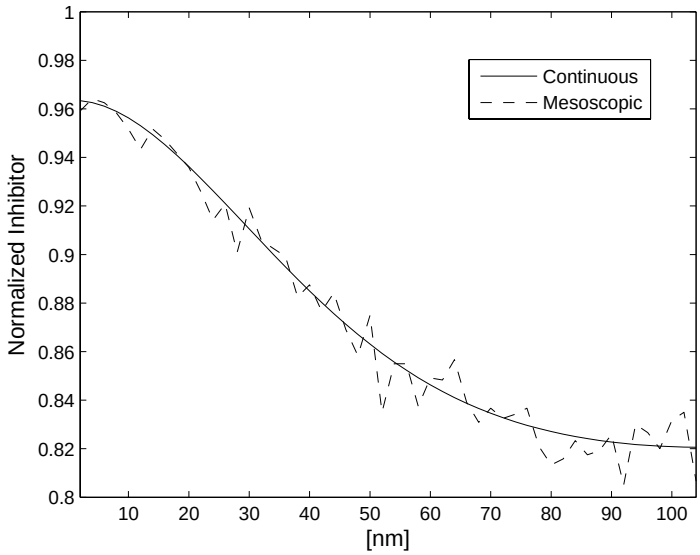

Figure 6.5.: Convergence of mesoscopic and continuous post-exposure bake simulation for the contact hole simulation

were converted into concentration dependent parameters based on the PAG concentration used in the mesoscopic model. Duration of PEB and development was set to 90s and 30s respectively. The averaged inhibitor concentration is displayed in Figure 6.5 compared to the continuous solution showing a good convergence.

6.4.2. Fast marching mesoscopic model

For the fast marching mesoscopic model the same aerial image as for the continuous model was used as input. In the following mesoscopic PEB the resolution was set to 2 nm along the resist plane and 10 nm along the resist height where polymers were now neglected. For the development step the inhibitor concentration from the mesoscopic PEB was again normalized to 1 such that a standard Mack4 model could be used. The resolution was increased for higher accuracy during development by a factor of 2 along each direction thus defining a new resolution of 1 nm along the resist plane and 5 nm along the resist height.

The aerial image as well as the inhibitor concentration and arrival times after development together with the steps made for profile preparation are shown in Fig. 6.6 a) - e) for a dose value of $16mJ/cm^2$ at best focus. Note that a smoothing kernel of size $2 \times 2 \times 10$ nm was applied to the final simulated profile as the SEM for measuring the experimental roughness data has only a resolution of 2 nm. Furthermore the SEM image is only two dimensional, therefore an averaging over the height of the contact hole occurred. These effects were in a first approach modelled by the applied smoothing kernel. The resulting bossung plot compared to the experimental data is shown in Fig. 6.7 while the resulting

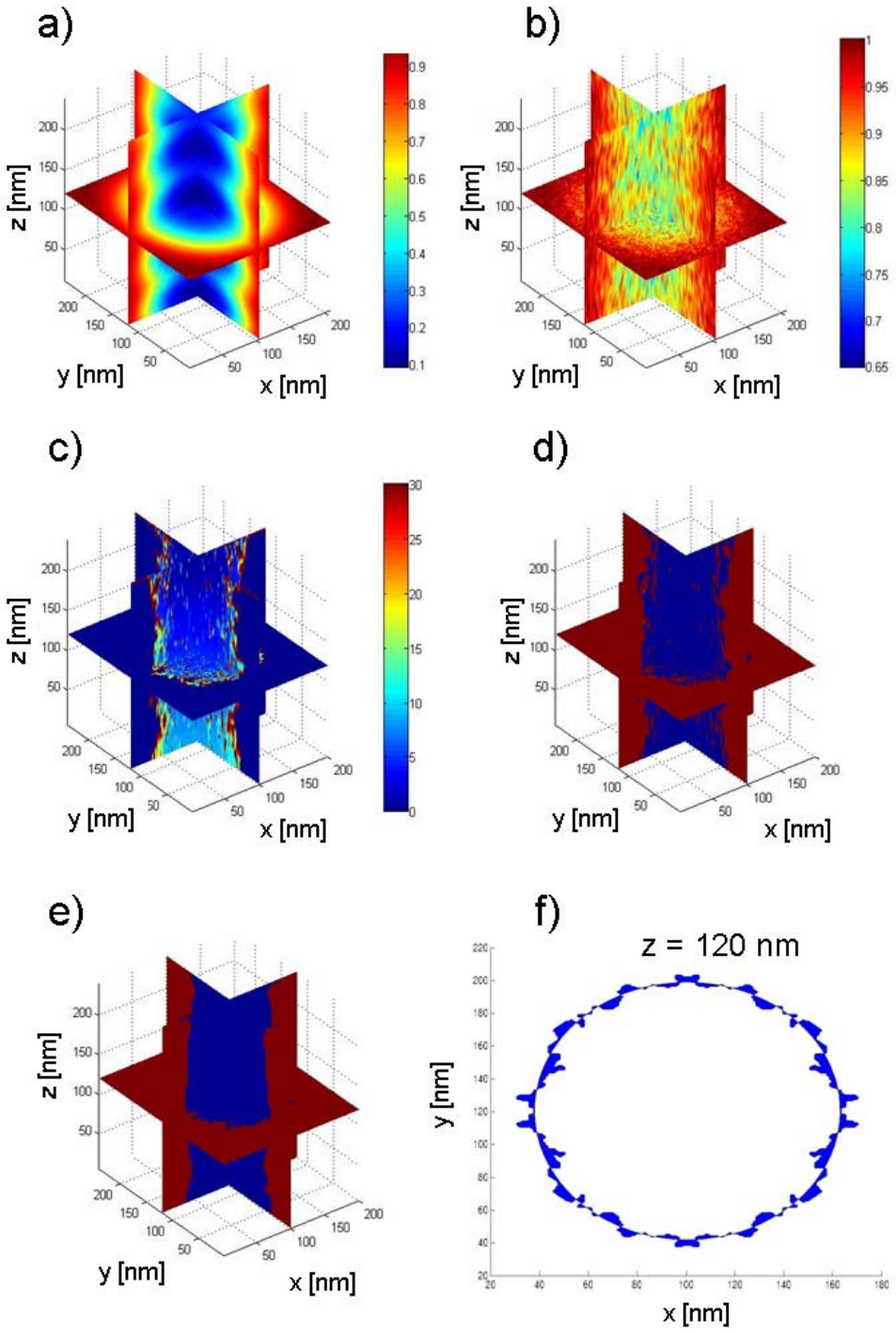

Figure 6.6.: a) Aerial image as input to the mesoscopic PEB. Also shown are three intersection planes at $x = 102\,nm$, $y = 120\,nm$ and $z = 120\,nm$. b) Normalized inhibitor concentration after mesoscopic PEB. c) Arrival times of the front after fast marching development. d) Resulting profile. e) After applying a smoothing filter with a kernel of size $2 \times 2 \times 10\,nm$ and a hoshen-kopelman cluster finding algorithm. f) A cut in the resist plane in a height of $z = 120\,nm$ together with a best fit ellipse is shown. The deviation from the best fit ellipse was defined as roughness.

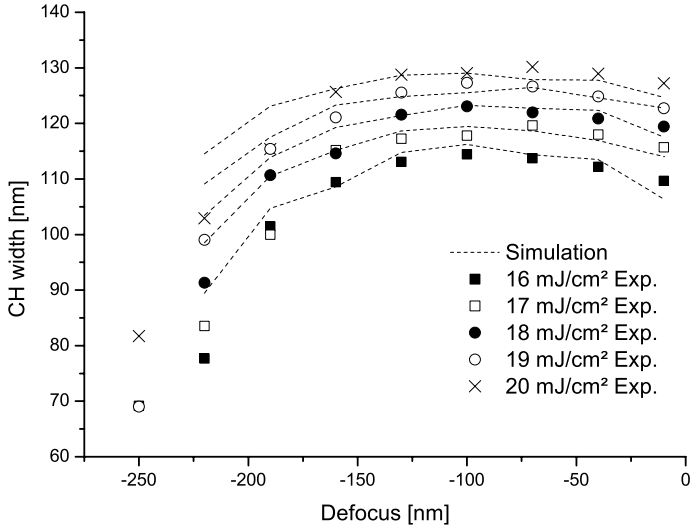

Figure 6.7.: Resulting contact hole (CH) width for the mesoscopic fast marching model (dashed lines) compared to experimental data (symbols).

roughness values are shown in Fig. 6.8. For each point an average over 10 simulations was made. As can be seen the experimental CH widths are described well. For the roughness data an offset exists while the increase in defocus is described correctly. The offset could arise from several contributions. As mentioned before the roughness was measured with a top-down SEM which analyzes a two-dimensional intensity picture showing the amount of scattered secondary electrons. This may lead to considerable smoothing which was here only considered by applying a simple averaging filter to the simulated profile. For a more accurate description the explicit scattering of the incoming electrons must be taken into account where the SEM measurement process must be modelled to account for its effects. This could be achieved by defining a more complex set of edge detection and averaging filters to model the intensity distribution of the detected secondary electrons of the SEM.

6.4.3. Level set mesoscopic model

To investigate another method of reducing the offset between the simulated and measured data the narrow band level set algorithm described in section 6.3 was used. Here the same parameters as for the fast marching development were used where now a curvature term with a prefactor of $\kappa_f = 1.5$ was included for front propagation. This lead to a surface reordering already during development smoothing out many of the high frequency contributions. However, while the computation time for the fast marching mesoscopic model is at around 10s for one simulation it is at around 2 min. for the level set model although the update of the level set function is already restricted to a narrow band. The resulting CH widths and roughness values are displayed in Fig. 6.9 and 6.10. As can be

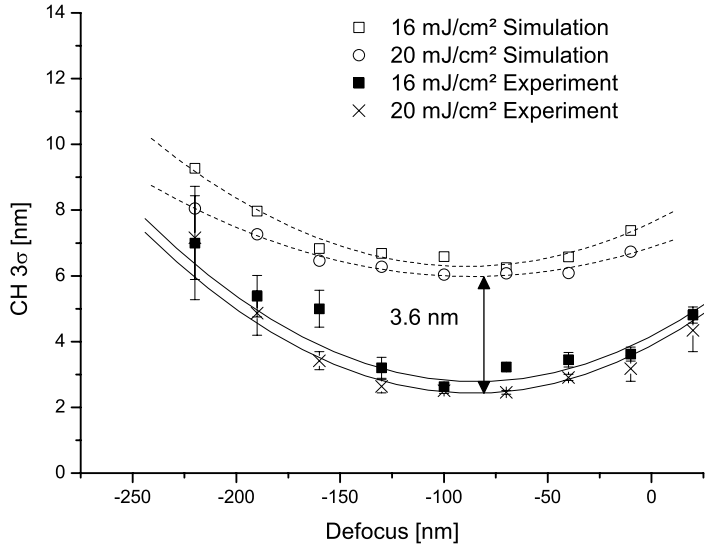

Figure 6.8.: Resulting contact hole edge roughness for fast marching mesoscopic model compared to the experimentally measured roughness with a SEM.

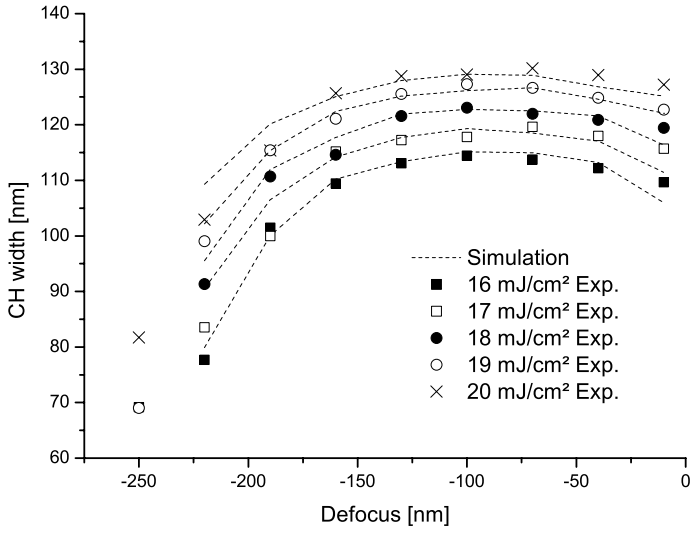

Figure 6.9.: Resulting contact hole (CH) width for the mesoscopic level set model compared to experimental data.

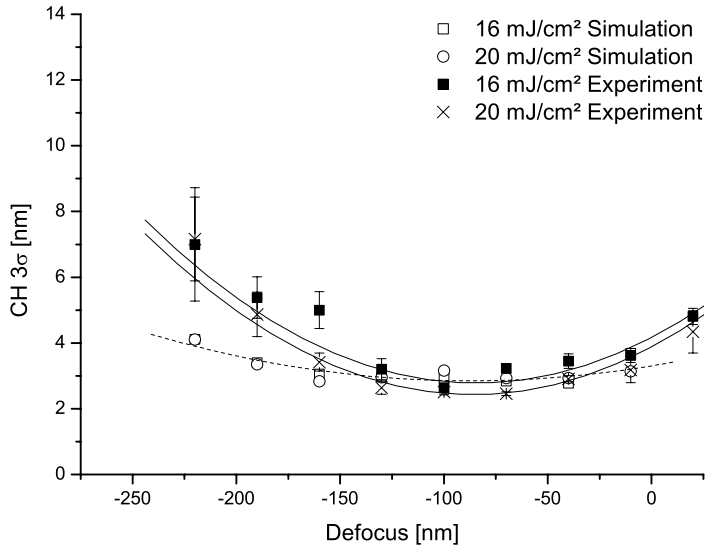

Figure 6.10.: Resulting contact hole edge roughness for the level set mesoscopic model compared to the experimentally measured roughness with a SEM.

seen the offset in roughness could be reduced. However, due to the smoothing the increase of roughness in defocus is not described correctly anymore. Compared to the experimental data the increase of roughness in defocus is underestimated.

6.4.4. Critical ionization model

Finally the critical ionization model as described before was used on the same set of experimental data. The only change was here in resolution, which was set to 2.4 nm along each direction in the mesoscopic PEB. For the development resolution was increased to 0.8 nm again. The polymer size used was 14 $r.u.$ with a critical ionization level of 15%, thus corresponding to a normalized inhibitor threshold during development of $m_{th} = 0.85$. All other parameters remained constant. As can be seen in Fig. 6.11 and Fig. 6.12 a similar CH width as before can be obtained. The resulting roughness values are larger than for the previous models such that the effect of the polymer removal based on the developer percolation can be observed which increases fluctuations. Also more high frequent roughness is present due to the increased resolution of the mesoscopic PEB along the z-direction.

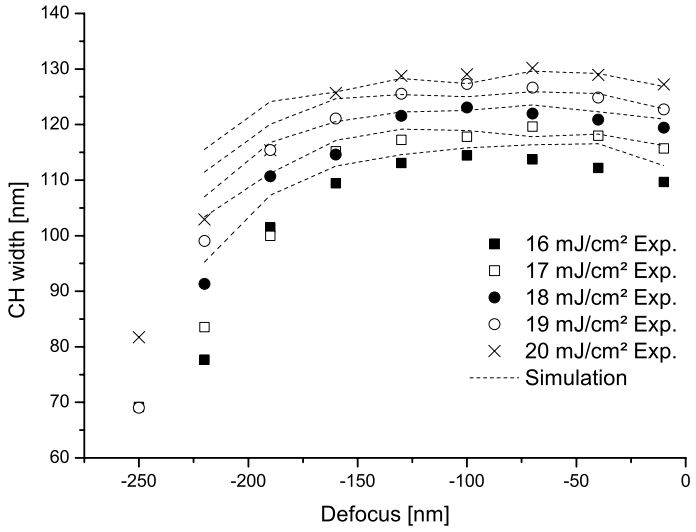

Figure 6.11.: Resulting contact hole (CH) width for the mesoscopic critical ionization model compared to experimental data.

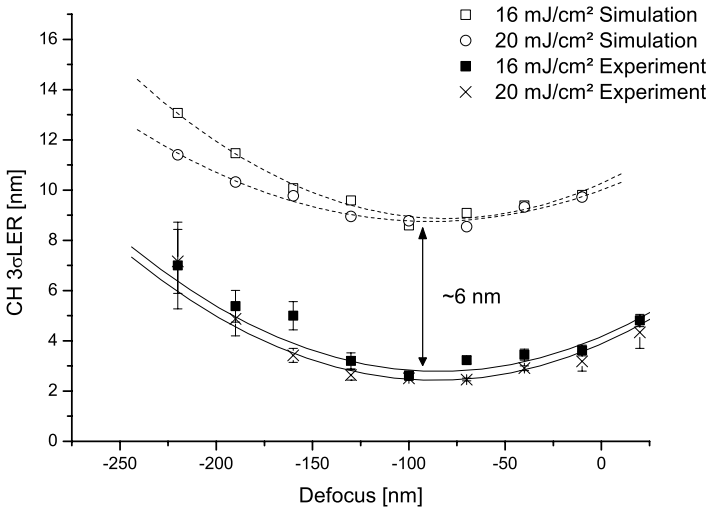

Figure 6.12.: Resulting contact hole edge roughness for the critical ionization model compared to the experimentally measured roughness with a SEM.

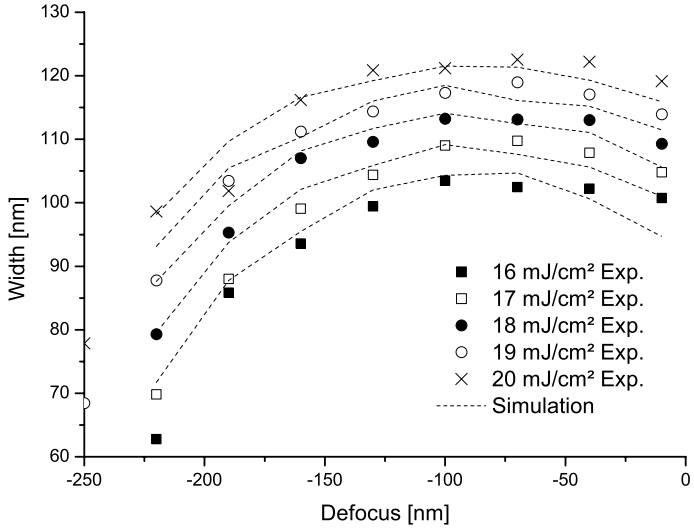

Figure 6.13.: Resulting contact hole (CH) width for the mesoscopic fast marching model compared to experimental data.

6.4.5. Impact of process change on roughness

After convergence of the several simulators to a calibrated continuous model and experimental data has been demonstrated the predictability of the model regarding process changes was investigated. Therefore the fast marching stochastic model was used where the pitch of the contact holes was decreased to 260 *nm*. Furthermore the size of the contact holes was changed to 115 nm width and 210 nm length on the mask. The results are shown in Fig. 6.13 and Fig. 6.14. When comparing the experimental data to the previous process an increase of roughness by about 0.5 *nm* in best focus can be observed which is shown together with the simulated data in 6.15. An increase was predicted by simulation aswell, where here the roughness increased by about 0.7 *nm* when compared to the previous process. Thus the model seems capable, once calibrated, to predict possible changes in roughness correctly. Unfortunately very dense contact holes of pitch 196 *nm* could not be described correctly in resulting contact hole width which may results from several in- and outdiffusion effects at the bottom and top layers of the resist which were not considered yet.

6.5. Conclusion of contact hole simulations

Three different dissolution algorithms were applied to the outcome of a mesoscopic PEB simulation. While in the mesoscopic PEB simulation additionally base diffusion and reactions were incorporated and a convergence with macroscopic simulations verified also the

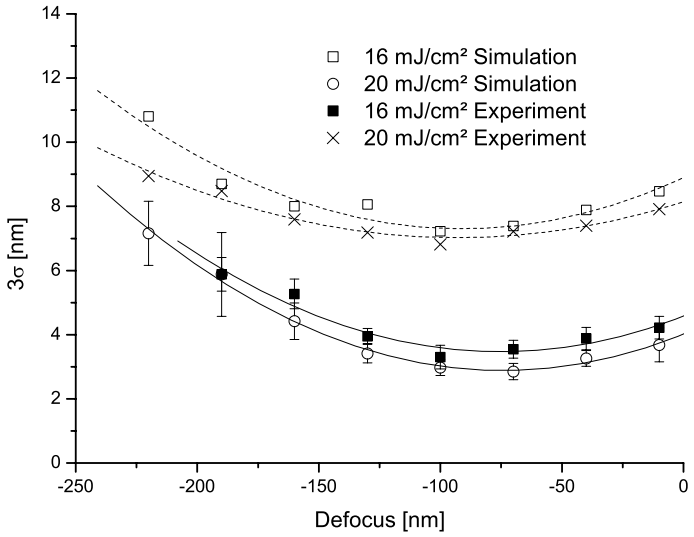

Figure 6.14.: Resulting contact hole edge roughness for the fast marching model compared to the experimentally measured roughness with a SEM.

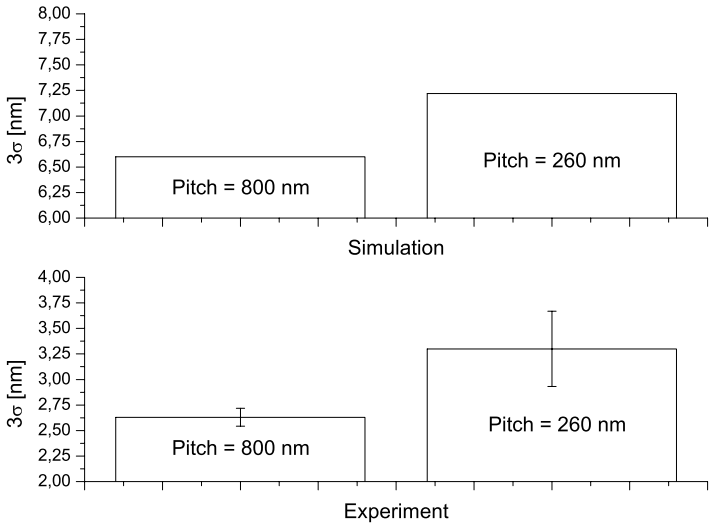

Figure 6.15.: Change of roughness for the two different processes at best focus of -0.1 μm for $16 mJ/cm^2$

three different dissolution algorithms converged in their resulting CD values to the results from a macroscopic simulation.

The fully mesoscopic approach by means of a critical ionization model and polymer removal calculates at the order of the polymer repeat unit (which is at 0.8 nm resolution). This model seems suitable for small critical dimensions as fundamental polymer properties are considered. For the contact hole simulations computation time due to the large number of cells needed was slow while the simulation results were comparable to the other dissolution algorithms. Therefore this model should only be used for investigating CDs below 60 nm as would be the case for immersion or EUV lithography.

The combination of a mesoscopic site density PEB algorithm together with a continuous fast marching approach yielded the best numerical performance for the contact hole simulations. This algorithm is suitable for simulating larger areas at arbitrary resolutions while incorporating roughness. However, as polymer properties are neglected it should only be used for investigating larger features such as a contact hole at resolutions of the order of at least 2 nm. It predicted successfully the different roughness trends observed in experimental data where also the change of roughness when changing the pitch or periodicity of the contact holes was accurately described.

For the level set dissolution algorithm a surface diffusion is incorporated to adjust the magnitude of simulated roughness. This new approach to resist dissolution needs more computation time than the fast marching solution and applies for larger features as well. Its major advantage is to offer a possibility of connecting microscopic polymer properties such as a polymer mobility into a macroscopic framework. However, as roughness in defocus was underestimated further research is necessary for investigating the effects of this new term.

7. Conclusion

In this thesis several algorithm for simulating the photoresist dissolution on a macroscopic and mesoscopic scale were developed. For the macroscopic scale a continuous development algorithm based on a fast marching approach [99] was realized for the resist dissolution. It completes a software for continuous lithography simulation which was for the first time applied to a customized problem where a new double exposure process was investigated.

For simulating on a mesoscopic scale a novel development algorithm based on the Gillespie algorithm was implemented. A developer front is integrated in time taking into account the various fluctuations arising from polymer size, ionization-neutralization reactions and developer percolation. The polymer dissolution is here based on the critical ionization model [60] where polymers are removed as soon as a certain amount of polymer sites are ionized. Additionally base diffusion was incorporated into the mesoscopic post-exposure bake approach from [84] and convergence with a continuous solution of the rate equations verified. To our knowledge the complete description ranging from exposure over post-exposure bake and resist development on a mesoscopic scale by means of Monte Carlo techniques is in its specific implementation unique. In the obtained results it is comparable to previous work from [60, 63, 70, 92]. Especially the development module is the only one incorporating ionization-neutralization reactions of polymers by means of logarithmic classes and von Neumann rejection while at the same time introducing instantaneous nearest neighbour developer diffusion. Also the approach of creating polymers by molecular dynamics simulation to obtain structural information on a microscopic level and incorporating the results back to a mesoscopic level is in its specific implementation unique.

With the mesoscopic software for the first time main-chain scission of polymers in the extreme-ultraviolet regime were studied. Previous experimental results on LER trends for increasing PAG concentration or the dependance of LER on inhibitor contrast at the later forming edge could be verified. Finally the effect of polymer molecular weight on LER for chain-like polymers was discussed.

To allow for a faster simulation a new model for line edge roughness simulation comparable to [63] was developed. This was achieved by combining the previously developed continuous fast marching algorithm with the mesoscopic post-exposure bake simulation where polymer properties were now neglected allowing for simulation at arbitrary resolu-

tions. For verification purposes edge roughness of contact holes were studied. It is shown that similar roughness trends as observed in printing experiments of isolated contact holes can be modelled where an offset between experimental and simulated roughness exists. To reduce this offset a level-set algorithm was implemented where a curvature term was for the first time identified with a surface reordering at the resist-developer interface by means of a surface tension. Its effects were discussed.

With the development of the above algorithms basic roughness effects in resists could be described well but many open questions remain. When arriving at the level of a single polymer repeat unit various resist effects were not considered. E.g. to accurately describe the total magnitude of LER further effects regarding polymer reordering during PEB and development need to be considered. There are complex interactions between the developer solution consisting of a solvent, a strong base, and various surfactants and the photoresist polymers which may go beyond a simple critical ionization model. These effects include the swelling behaviour of photoresists in contact with the developer which might be important when investigating the impact of polymer size on line edge roughness. Regarding the performance of the current approach to LER simulation it is still computational expensive compared to established continuous models. Therefore it might be questionable whether including more fundamental effects is really desired. However, the current kind of mesoscopic models are the only ones able to offer a detailed physical insight into the basic polymer reaction kinetics. They will become advantageous when the length scale of feature sizes approaches the dimensions of single polymers.

The long-term implications of this thesis are that semiconductor industry will face a major issue when coming to smaller feature sizes as LER cannot be reduced below a certain limit. This limitation arises as part of the chemical amplification of photoresist and the finite size of the polymers and cannot be avoided.

8. Zusammenfassung

In dieser Arbeit wurden verschiedene Algorithmen entwickelt um die Entstehung der Kantenrauhigkeit von Photolacken in der Lithograhie zu beschreiben. Dabei wurde speziell für den in der Lithographie vorkommenden Entwicklungsschritt nach der Belichtung und dem "Post-exposure bake"(PEB) verschiedene kontinuierliche und mesoskopische Algorithmen erforscht.

Um die Lackentwicklung auf einer mesoskopischen Skala zu simulieren wurde ein auf dem Gillespie-Algorithmus bzw. auf der kinetischen Monte-Carlo Methode basierender Ansatz implementiert. Eine Front wird dabei in der Zeit propagiert wobei die Rauhigkeit des resultierenden Profils von der Polymergrösse und der Perkolation des Entwicklers abhängt. Das Herauslösen einzelner Polymere basiert dabei auf dem Critical-Ionization Modell bei dem eine bestimmte Anzahl von funktionellen Gruppen innerhalb eines Polymers ionisiert sein müssen, damit es in einer wässrigen Base gelöst werden kann. Kombiniert mit einem bereits existierenden mesoskopischen PEB Modell wurden dabei fundamentale Auflösungsgrenzen von Photolacken untersucht. Dabei wurde in Übereinstimmung mit bereits bekannten experimentellen veröffentlichten Trends eine Abhängigkeit der Rauhigkeit vom Schutzgruppenkontrast gefunden. Ebenso führt eine Erhöhung der Säure erzeugenden "Photoacid generators"(PAG) zu einer Verringerung der Rauhigkeit. Der Einfluss der Polymergrösse auf die Rauhigkeit wurde dabei im Modell untersucht. Dabei wurde auch ein neuer Ansatz entwickelt in dem die Polymerstruktur mittels Molekulardynamik-Simulationen auf einer mikroskopischen Skala beschrieben und die Strukturinformation in dem mesoskopischen Modell eingebaut wurde.

Da dieses Modell aufgrund des fundamentaleren Ansatzes im Vergleich zu kontinuierlichen Simulatoren eine wesentlich höhere Rechenzeit benötigt wurde das mesoskopische PEB Modell mit einem kontinuierlichen Fast-Marching Ansatz kombiniert wobei der Einfluss einzelner Polymere vernachlässigt wurde. Der Fast-Marching Ansatz ist bereits seit 1995 als ein Standardansatz zur Frontpropagation bekannt. Der hier entwickelte Algorithmus wurde dabei anhand von analytischen Lösungen und einem Level-Set Algorithmus verifiziert. Der so entwickelte Ansatz erlaubt eine Simulation bei beliebiger Auflösung die nicht mehr darin limitiert ist eine funktionelle Gruppe innerhalb eines Polymers aufzulösen. Dieses Modell wurde anhand von experimentell gemessenen Kontaktlochdaten im Vergleich zum Critical-Ionization und einem Level-Set Modell verifiziert.

Zusammenfassend war durch die in dieser Arbeit entwickelten Algorithmen eine Beschreibung des Photolackes auf einer mesoskopischen Skala möglich wobei bereits bekannte experimentelle und simulatorische Ergebnisse in der Literatur erklärt und reproduziert werden konnten.

A. Maxwell equations

For the case of a source free and homogeneous medium for the electric and magnetic field $\vec{E}$ and $\vec{B}$ the maxwell equations are

$$\vec{\nabla} \cdot \vec{B} = 0 \tag{A.1}$$

$$\vec{\nabla} \times \vec{E} + \frac{\partial \vec{B}}{\partial t} = 0 \tag{A.2}$$

$$\vec{\nabla} \cdot \vec{D} = 0 \tag{A.3}$$

$$\vec{\nabla} \times \vec{H} - \frac{\partial \vec{D}}{\partial t} = 0 \tag{A.4}$$

where $\vec{D} = \varepsilon \vec{E}$ and $\vec{B} = \mu \vec{H}$ with $\varepsilon = \varepsilon_0 \varepsilon_r$ being the susceptibility and $\mu = \mu_0 \mu_r$ the permeability. For a non-absorbing medium as will be assumed here ε and μ are real. Transforming into Fourier space for solutions of the form $e^{-i\omega t}$ with ω being the frequency of the wave leads to the set of Helmholtz wave equations

$$(\vec{\nabla}^2 \ + \ \mu\varepsilon\omega^2) \ \vec{E} = 0 \tag{A.5}$$

$$(\vec{\nabla}^2 \ + \ \mu\varepsilon\omega^2) \ \vec{B} = 0 \tag{A.6}$$

A.0.1. Scalar diffraction

To derive the imaging equations a simplification will be made where only one component of the electric field $\psi(\vec{x})$ will be considered. This approximation leads to the scalar diffration theory such that

$$(\vec{\nabla}^2 + k^2)\psi(\vec{x}) = 0 \tag{A.7}$$

where $k = \omega/c$ is the wave vector of the electric field and $c = \frac{1}{\sqrt{\mu_0 \varepsilon_0}}$ is the velocity of light. The corresponding Green's function $G(x)$ is then given by the equation

$$(\Delta^2 + k^2)G(\vec{x}, \vec{x'}) = -\delta(\vec{x} - \vec{x'}) \tag{A.8}$$

Defining now several regions depicted in Fig. A.1 diffraction occurs at an interface A which separates region 1 containing the sources from the remaining volume in region 2. The interface B which encloses together with interface A region 2 is usually located at infinity and the total surface is $S = A \cup B$. Inside this volume Green's theorem can be

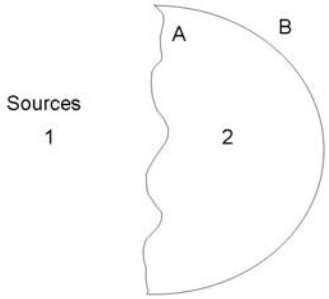

Figure A.1.: Regions and boundaries for calculating diffraction.

applied such that

$$\psi(\vec{x}) = \oint_S [\psi(\vec{x}')\vec{n}' \cdot \vec{\nabla}' G(\vec{x}, \vec{x}') \; - \; G(\vec{x}, \vec{x}')\vec{n}' \cdot \vec{\nabla}' \psi(\vec{x}')] da' \tag{A.9}$$

where $\vec{n}'$ denotes the inner normal of S. Outside of V the left side vanishes. Taking as the Green's function G solutions of the form $\frac{e^{ikR_o}}{4\pi R_o}$ where $\vec{R_o} = \vec{x_o} - \vec{x'}$ is the distance of the observation point from A the fields described by ψ must fulfill the requirements for outgoing spherical waves, namely

$$\psi \to f(\Theta, \Phi)\frac{e^{ikr}}{r} \; \frac{1}{\psi}\frac{\partial \psi}{\partial r} \to (ik - \frac{1}{r}) \tag{A.10}$$

such that contributions arising from B vanish as r reaches infinity. Therefore the resulting field only depends on integrating over the interface A such that

$$\psi(\vec{x_o}) = \oint_A [\psi(\vec{x}')\vec{n}' \cdot \vec{\nabla}' G(\vec{x_o}, \vec{x}') \; - \; G(\vec{x_o}, \vec{x}')\vec{n}' \cdot \vec{\nabla}' \psi(\vec{x}')] da' \tag{A.11}$$

Above equation is also called the integral theorem of Kirchhoff and Helmholtz. Considering now the diffraction of a wave omitted from a point source with unit amplitude in front of a slit as depicted in Fig. A.2 ψ_s and G on the screen can be defined as

$$\psi_s(x') = \frac{e^{ikR_s}}{R_s} \tag{A.12}$$

$$G(x') = \frac{1}{4\pi}\frac{e^{ikR_o}}{R_o} \tag{A.13}$$

$$\tag{A.14}$$

where $\vec{R_s} = \vec{x_s} - \vec{x'}$. To solve integral (A.9) further boundary conditions need to be defined, namely the Kirchhoff boundary conditions stating that

- on the slit A': $\psi(x') = \psi_s(x')$
- on the diffraction screen A: $\psi(x') = 0$ and $\frac{\partial \psi(x')}{\partial n'} = 0$

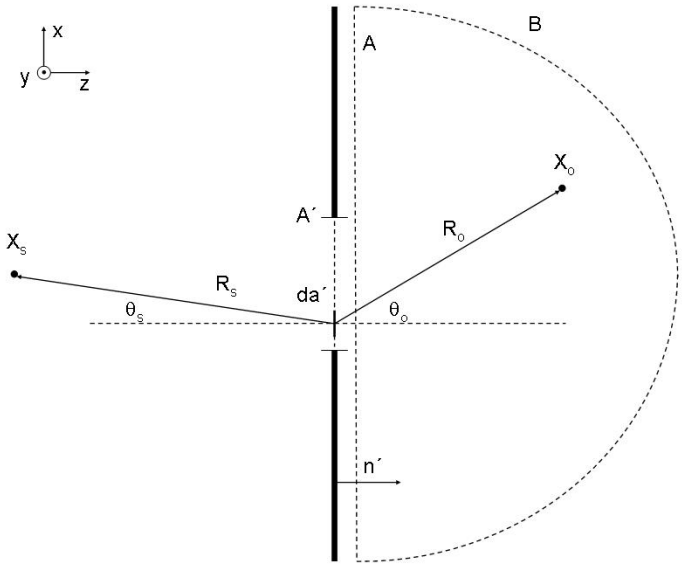

Figure A.2.: Diffraction of a spherical wave from a slit

The derivative along the screen normal of ψ is then approximated by

$$\frac{\partial \psi_s}{\partial \vec{n}'} = \vec{n}' \cdot \vec{\nabla} \psi_s(\vec{x}') \tag{A.15}$$

$$= -\cos\Theta_s \; (ik - 1/R_s) \frac{e^{ikR_s}}{R_s} \tag{A.16}$$

$$\approx -\cos\Theta_s \; ik \frac{e^{ikR_s}}{R_s} \tag{A.17}$$

and similar for G

$$\frac{\partial G}{\partial \vec{n}'} = \vec{n}' \cdot \vec{\nabla} G(\vec{x}') \tag{A.18}$$

$$\approx \cos\Theta_o \; ik \frac{e^{ikR_o}}{4\pi R_o} \tag{A.19}$$

When inserted into (A.9) this yields

$$\psi(\vec{x_o}) = \frac{ik}{2\pi} \oint_{A'} \frac{e^{ikR_s}}{R_s} \; \frac{e^{ikR_o}}{R_o} \; \frac{\cos\Theta_s + \cos\Theta_o}{2} \; da' \tag{A.20}$$

where $\frac{\cos\Theta_s + \cos\Theta_o}{2} e^{ikR_o}$ is called the obliquity factor. Now approximations can be made depending on the distance of the observation point relative to the screen where a Taylor series expansion of the exponent ikR_o is applied such that

$$kR_o = k\sqrt{(x_o - x')^2 + (y_o - y')^2 + z_o^2} \tag{A.21}$$

$$= kz_o(1 + \frac{1}{2}(\frac{x_o - x'}{z_o})^2 + \frac{1}{2}(\frac{y_o - y'}{z_o})^2 \mp \ldots) \tag{A.22}$$

$$= kz_o(1 + \frac{x_o^2 + y_o^2}{2z_o^2} + \frac{x'^2 + y'^2}{2z_o^2} - \frac{x'x_o + y'y_o}{z_o^2} \mp \ldots) \tag{A.23}$$

The Fresnel approximation truncates the Taylor approximation after the first term. Denoting by w the width of the slit this approximation remains valid as long as $z_o \gg w$. For the case of Fraunhofer diffraction additionally the square dependance upon the integration variables x', y' is neglected which yields

$$kR_o \approx kz_o + \frac{k}{2z_o}(x_o^2 + y_o^2) - \frac{k}{z_o}(xx' + yy') \tag{A.24}$$

This approximation holds for $z_o \gg w^2/\lambda$. For simplification on-axis illumination will be assumed, thus the obliquity factor reduces to 1 as $\cos\Theta_s \approx \cos\Theta_o \approx 1$ while $R_s = z_s$. The final Kirchhoff integral in the Fraunhofer approximation then yields

$$\psi(\vec{x_o}) = \frac{ik}{2\pi} \frac{e^{ik(z_o+z_s)}}{z_o z_s} e^{i\frac{k}{2z_o}(x_o^2+y_o^2)} \oint_{A'} e^{-ik(x'x_o+y'y_o)}\, da' \tag{A.25}$$

which is a constant times the Fourier transform of the slit.

B. Imaging of periodic structures

For the case of optical lithography the light sources are in the focal plane of a condenser lens which is needed for uniformly illuminating the mask pattern as previously shown. This arrangement is called Köhler illumination. Based on this setup in the following a different view on the imaging equation for periodic patterns will be derived. This view results from considering the spatial frequencies in Fourier space. Then the numerical aperture will be introduced.

Assuming an outgoing wave $\psi_s = A_s e^{i\vec{k}\vec{x}}$ from a single coherent source point on the optical axis, here being a plane wave with an additional amplitude A_s, the object image immediately behind the mask is given by

$$\psi_o(x,y) = A_s e^{ik(s_x x + s_y y)} t(x,y) \tag{B.1}$$

where $t(x,y)$ is the mask transmission funtion and s_x and s_y are normalized wave vectors such that $s_z = \sqrt{1 - s_x^2 - s_y^2}$ and therefore $|\vec{s}| = 1$. The mask transmission function will be assumed to be real and one in the bright regions and zero in the dark regions. Furthermore $t(x,y)$ is periodic such that

$$t(x + a/M, y + b/M) = t(x,y) \tag{B.2}$$

where M is the magnification factor used in the projection optics. Expressing $t(x,y)$ in terms of its Fourier coefficients T_{nm} leads to

$$t(x,y) = \sum_{nm} T_{nm} e^{i2\pi M(n/a\ x + m/b\ y)} \tag{B.3}$$

The image behind the mask enters the projection optics where phase transformation properties of the lens will be neglected (e.g. the image on the wafer is at zero defocus with no aberrations or apodisations) such that the final image is given by

$$\psi(x,y) = \frac{ik}{2\pi} A_s \int t(x',y') e^{ik(S_x x' + S_y y')} dx' dy' \tag{B.4}$$

where a new normalized wave vector $\vec{S} = \vec{s} \cdot \vec{x}$ has been defined. Due to the Fourier decomposition of $t(x,y)$ and the orthogonality relation of the Fourier functions only spatial frequencies where

$$S_x = nM\lambda/a \tag{B.5}$$

$$S_y = mM\lambda/b \tag{B.6}$$

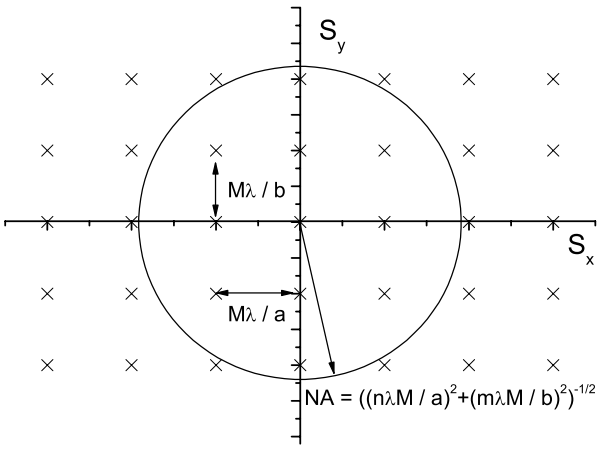

Figure B.1.: Spatial frequencies of a single source point in the object plane. The circle denotes the points outside the NA of the projection optics.

contribute to the final image. This leads to

$$\psi(x,y) = \frac{ik}{2\pi} A_s \sum_{nm} T_{nm} e^{ikM(n\lambda/a\ x\ +\ m\lambda/b\ y)} \tag{B.7}$$

But the summation cannot be extended over an infinite amount of frequencies as this is band-limited by the finite extent of the projection lens. The maximum angle α captured by the projection optics (as defined in Fig. 2.2 a) determines its numerical aperture (NA), where

$$NA = \sin\alpha \tag{B.8}$$

in air. This in turn determines the maximum frequency which can be used for imaging which is typically described by a pupil function $P(n,m)$,

$$P(n,m) = \begin{cases} 1 \text{ if } \sqrt{(nM\lambda/a)^2 + (mM\lambda/b)^2} \leq NA \\ 0 \text{ else} \end{cases} \tag{B.9}$$

such that

$$\psi(x,y) = \frac{ik}{2\pi} A_s \sum_{nm} T_{nm} P(n,m) e^{ikM(n\lambda/a\ x\ +\ m\lambda/b\ y)} \tag{B.10}$$

All these results are depicted in Fig. B.1 where the frequency contributions of a single source point are shown. As in general a source consists of many source points, the final intensity can be calculated by summing up over the contribution of each individual source point where an off-axis position simply leads to a shift in frequency space.

C. Fast marching source code references

The source code is written in *C*. In the following a list of all functions used in the computation will be given. Furthermore a flow chart is included showing the main computation steps and the function calls involved. A detailed description of the input parameters of each function is included as well.

C.1. fm.cpp File Reference

Functions

- double **find_root (double a, double b, double c, double T)**

  The maximum root of the eikonal equation.

- **void chk_bnd (int p_sphere[3], double lat_xzy[3])**

  The boundary conditions.

- **void up_or_down (long int n, double **daten, long int k, long int **front_part)**

  Rearrange the heap including promotion and demotion.

- **void adv_dgl (double lat_xzy[3], int i, int j, double *latt_arr, double b_par[7], int k, double *old, int x, int y, int z, double **front, long int front_l_n, double *parm, long int **front_part)**

  Recalculates the nearest neighbour.

- **int stochml (double *latt_arr, double *corner1, double *corner2, double *lat_xzy, double *dglgrid_old, double *parm)**

  Main routine.

- **void mexFunction (int nlhs, mxArray *plhs[], int nrhs, const mxArray *prhs[])**

  Matlab interface function.

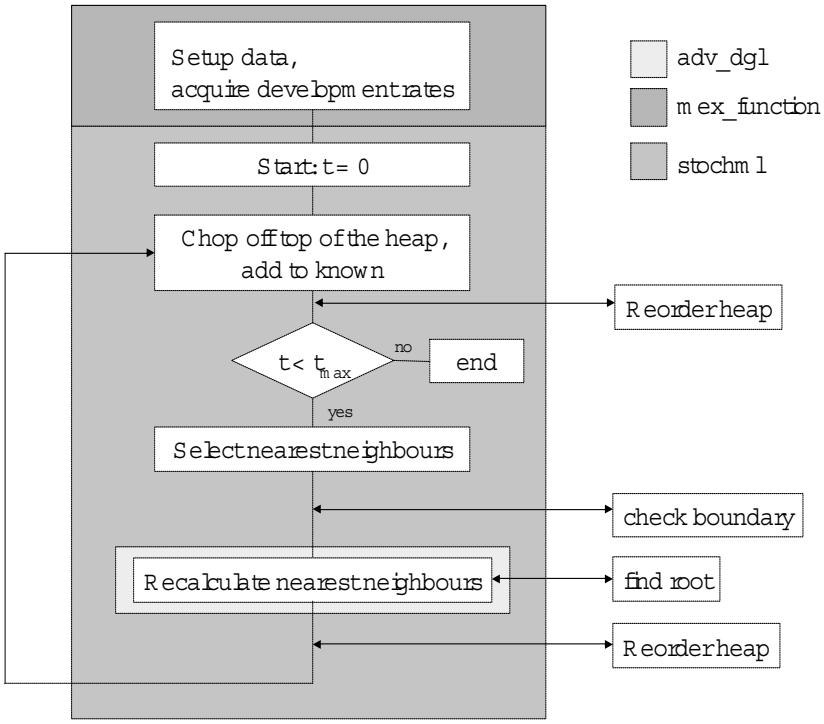

Figure C.1.: Flow chart showing the basic calculation steps and the functions involved

Table C.1.: Input variable explanation

function	variable	explanation
find_root	a	Constants from the solution to the quadratic equation $ax^2 + bx + c$
	b	Constants from the solution to the quadratic equation $ax^2 + bx + c$
	c	Constants from the solution to the quadratic equation $ax^2 + bx + c$
	T	Maximum known time value of n.n.
chk_bnd	p_sphere[3]	x,y,z coordinates for one n.n.
	lat_xzy[3]	lattice dimensions
up_or_down	n	length of the heap
	daten	backpointer matrix (bpm), 1. col.: cell value, 2. col.: cell index
	k	heap position of n.n. after recalculation
	front_part	bpm, 1.col: cell status (0: far, 1:trial, 3:known), 2.col: heap position
stochml	latt_arr	1D array containing the development rates
	corner1	as in solid
	corner2	as in solid
	dglgrid_old	array on which the solution is calculated and returned
	parm	array containing the values from the devpro m-file, see devpro.m
adv_dgl	i	current x coordinate
	j	current y coordinate
	k	current z coordinate
	b_par	array containing the lattice constants in x,y,z
	x	x coordinate of known value with maximum time
	y	y coordinate of known value with maximum time
	z	z coordinate of known value with maximum time

D. Molecular modelling details

The fully protected polymer poly(4-tert-butoxycarbonyloxystyrene) (PBOCST) was created within a large volume with a cubic unit cell of around 500 Å box length and periodic boundary conditions. Depending on the length of a single polymer between 6 and 24 further polymers with their center of mass set at random positions were added such that a total of 240 r.u. was contained within the box. These numbers result from the fact that the MD box was slowly compressed to a length of 43 Å, allowing the molecules to relax at least 1000 fs between successive compression steps. Then a density of approximately 3 r.u. per nm^3 was reached. Note that 60 r.u. polymers were tried to be simulated as well, but as only 4 polymers were contained within the 43 Å box effects from periodically extending the MD box for the later PEB step yielded results which differ strongly from the results when polymers were distributed by a self-avoiding random walk. Thus a sufficient number of polymers must be modelled within a single MD box. Further settings for the MD simulation regarding the bond energies and distances between the different molecules were taken from literature, and those bond energies missing were approximated. These were bond energies between carbon atoms in tetrahedral and sp2-hybridized configurations which were set to similar values as in the tetrahedral case. All hydrogen atoms were neglected. An amber force field with a cutoff between 5.0 to 10.0 Å was used for the dynamics simulation. Although the cutoff is quite small larger cutoffs were inapplicable due to a large increase in computation time. The temperature for the dynamics simulation was set to $400°K$. The polymers were then allowed to reorder for 100 ps, with the translation remover set to 75 fs. When the simulation was finished a *.pdb* file was created containing the position of every atom.

E. Surface Element

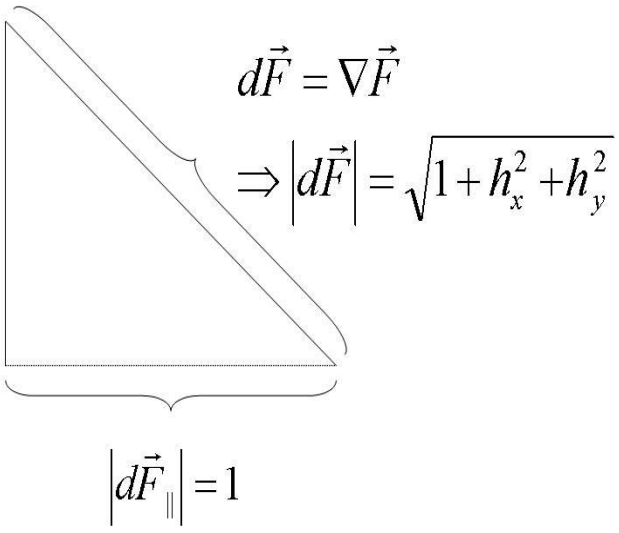

Figure E.1.: Sketch of the relation betweent projected area $\left|d\vec{F}_{||}\right|$ and surface area $\left|d\vec{F}\right|$.

As depicted in Fig. E.1 the given relation between the surface elements leads to a relation between the surface free energy per projected area g and the free energy per surface area γ

$$\gamma \cdot dF = g \cdot dF_{||} \tag{E.1}$$

$$\gamma\sqrt{1+h_x^2+h_y^2} = g \tag{E.2}$$

F. List of publications

- A. Philippou, T. Mülders and E. Schöll, Impact of photoresist composition and polymer chain-length on line edge roughness probed with a stochastic simulator, J. Micro/Nanolith. MEMS MOEMS, to be published
- A. Philippou, C. Nölscher and E. Schöll, Three-dimensional simulation of photoresist edge roughness in contact holes, Conference Micro- and Nanoelectronic Engineering, Kopenhagen, 2007, Poster
- A. Philippou and T. Mülders, Method for determining the edge profile of a volume of a photoresist after a development process, Patent US020070212624A1, 2007
- C. Nölscher, A. Philippou, K. Elian and T. Mülders, Double lithography with Single Layer Resist (SLR) process, Qimonda internal invention disclosure #1703, 2007, Patent pending
- S. Trogisch, M. Bender, W.-D. Domke, A. Philippou, M. Rößiger and Y. Wei, EUV printing of contact holes for the sub-40 nm node, Conference SPIE Photolithography, San Jose, 2007, Poster

Bibliography

[1] G. E. Moore, *Cramming more Components onto Integrated Circuits*, *Electronics* **38**, 8 (1965).

[2] G. E. Moore, *Lithography and the Future of Moore's Law*, *Proc. SPIE Optical/Laser Microlithography VIII* **2440**, 2 (1995).

[3] C. Windeck, *Merk-Zellen*, *c't Magazin, Heise Zeitschriften Verlag* , 6 (2006).

[4] R. Rosenkranz et al., *Gesamtprozess-Schulung 256M D11 DRAM*, *Infineon* (2004).

[5] T. Ytterdal, Y. Cheng, and T. A. Fjeldly, *Device Modeling for Analog and RF CMOS Circuit Design*, *John Wiley & Sons* (2003).

[6] Ji-Young Lee, Jangho Shin, Hyun-Woo Kim, Sang-Gyun Woo, Han-Ku Cho, Woo-Sung Han, and Joo-Tae Moon, *Effect of line edge roughness (LER) and line width roughness (LWR) on Sub-100 nm Device Performance*, *SPIE Proceedings* **5376** (2004).

[7] P. Oldiges, Q. Lin, K. Petrillo, M. Sanchez, M. Ieong, and M. Hargrove, *Modelling line edge roughness effects in sub 100 nm gate length devices*, *SISPAD Conference Proceedings, IEEE Publishing* , pp. 131 (2000).

[8] M. Born, E. Wolf, and A.B. Bhatia, *Principles of Optics: Electromagnetic Theory of Propagation, Interference and Diffraction of Light*, *Cambridge University Press, 7th Edition* (1999).

[9] R.M.A. Azzam and N.M. Bashara, *Ellipsometry and polarized light*, *Elsevier, 5th Edition* (1996).

[10] K. H. Schuster, *Reduction projection objective lens for microlithography*, *Patent EP 1006 388 A2* (1998).

[11] A. Sommerfeld, *Lectures on Theoretical Physics IV. Optics*, *Academic Press* (1964).

[12] J. D. Jackson, *Klassische Elektrodynamik*, *de Gruyter, 3rd Edition* (2002).

[13] M.D. Levenson, N.S. Visnawathan, and R.A. Simpson, *Improving Resolution in Photolithography with a Phase Shifting Mask*, *IEEE Trans.Electron Devices* **ED-29**, 12 (1982).

[14] A.K.-K. Wong, *Resolution enhancement techniques in optical lithography*, *SPIE Press* (2001).

[15] H.J. Levinson, *Principles of lithography*, *SPIE Press, 2nd Edition* (2005).

[16] B.J. Lin, *Deep UV lithography*, *J.Vac.Sci.Technol.* **12**, 6 (1975).

[17] H. Ito, C.G. Willson, and J.M.J. Frechet, *New UV resists with negative or positive tone*, *Digest of Technical Papers of the Symposium on VLSI technology* (1982).

[18] R.T. Kerth, K. Jain, and M.R. Latta, *Excimer Laser Projection Lithography on a Full-Field Scanning Projection System*, *IEEE Electron Device Lett.* **EDL-7**, 5 (1986).

[19] O. Nalamasu et al., *193 nm single layer resist strategies, concepts, and recent results*, *J.Vac.Sci.Technol. B* **16**, pp. 3716 (1998).

[20] R. Sze, *Physics of Semiconductor Devices*, *John Wiley and Sons, 2nd Edition* (1981).

[21] S. Kawada, Y. Tamai, S. Omae, and T. Ohmi, *Effect of surfactant-added developer on development of chemically amplified resists*, *SPIE Proc.* **3999**, pp. 717 (2000).

[22] *www.synopsys.com/products/tcad/acqmr/sgmc/solideuv.html* .

[23] A. B. Bortz, M. H. Kalos, and J. L. Lebowitz, *A new algorithm for Monte Carlo simulation of Ising spin systems*, *J. Comp. Phys.* **17**, 10 (1975).

[24] D. T. Gillespie, *A General Method for Numerically Simulating Stochastic Time Evolution of Coupled Chemical Reactions*, *J.Comp.Physics* **22**, 403 (1976).

[25] R.A. Ferguson, *Modeling and Simulation of Reaction Kinetics in Advanced Resist Processes of Optical Lithography*, *Dissertation, University of California, Berkeley* (1991).

[26] T. Mülders, *Post-exposure bake simulation: A fast, accurate and unconditionally stable method*, *Qimonda Internal Report* (2007).

[27] C.A. Mack, *Inside PROLITH: A Comprehensive Guide to Optical Lithography Simulation*, *Finle Technologies Inc., Austin, Texas, USA* (1997).

[28] E.W. Scheckler, N.N. Tam, A.K. Pfau, and A.R. Neureuther., *An Efficient Volume-Removal Algorithm for Practical Three-Dimensional Lithography Simulation with Experimental Verification*, *IEEE Trans.Computer-Aided Design* **12**, 9 (1993).

[29] W. Noh and P. Woodward, *A Simple Line Interface Calculation*, *Proceedings of the 5th International Conference on Fluid Dynamics, Springer* (1976).

[30] C. W. Hirt and B. D. Nichols, *Volume-of-Fluid (VOF) method for the Dynamics of Free Boundaries*, *Jour. Comp. Phys.* **39**, 201 (1981).

[31] J. A. Sethian, *Fast marching level set methods for three-dimensional photolithography development*, *SPIE 1996 International Symposium on Microlithography, Santa Clara, California* (1996).

[32] S. Osher and J.A. Sethian, *Fronts propagating with curvature dependent speed: Algorithms based on Hamilton-Jacobi*, *Jour. Comp. Phys.* **28** (1988).

[33] J. A. Sethian, *Level Set Methods and Fast Marching Methods*, *Cambrige University Press, 2nd Edition* (1999).

[34] L. Mandreoli, J. Neugebauer, R. Kunert, and E. Schöll, *Adatom Density kinetic Monte Carlo: A hybrid approach to perform epitaxial growth simulations*, *Phys. Rev. B* **68**, 155429 (2003).

[35] C. Ratsch, M. F. Gyure, R. E. Caflisch, F. Gibou, M. Petersen, M. Kang, J. Garcia, and D. D. Vvedensky, *Level-set method for island dynamics in epitaxial growth*, *Phys. Rev. E* **65**, 195403 (2002).

[36] K. Binder, *Monte Carlo Simulation in Statistical Physics*, *Springer, 4th Edition* (2002).

[37] W.H. Press, S.A. Teukolsky, W.T. Vetterling, and B.P. Flannery, *Numerical Recipes in C*, *Cambridge University Press, 2nd Edition* (1992).

[38] N. Metropolis, A.W. Rosenbluth, M.N. Rosenbluth, and A.H.Teller, *Equation of state calculations by fast computing machines*, *J. Chem. Phys.* **21**, 6 (1953).

[39] M. Meixner, *Simulation of self-organized growth kinetics of quantum dots*, *PhD thesis* , TU Berlin (2002).

[40] F. Elsholz, *Kinetic Monte Carlo simulations of thin film growth*, *PhD thesis* , TU Berlin (2006).

[41] R. Kunert, *Monte Carlo Simulation of stacked Quantum Dot Arrays*, *PhD thesis* , TU Berlin (2006).

[42] M. Block, *Analysis and control of complex growth phenomena in physics and biology*, *PhD thesis* , TU Berlin (2006).

[43] E. Schöll and S. Bose, *Kinetic Monte Carlo simulation of the nucleation stage of the self-organized growth of quantum dots*, *Sol. State El.* **42**, 1587 (1998).

[44] M. Meixner, E. Schöll, V. A. Shchukin, and D. Bimberg, *Self-assembled quantum dots: Crossover from kinetically controlled to thermodynamically limited growth*, *Phys. Rev. Lett.* **87**, 236101 (2001).

[45] M. Meixner, E. Schöll, M. Schmidbauer, H. Raidt, and R. Köhler, *Formation of island chains in SiGe/Si heteroepitaxy by elastic anisotropy*, *Phys. Rev. B* **64**, 245307 (2001).

[46] M. Meixner, R. Kunert, and E. Schöll, *Control of strain-mediated growth kinetics of self-assembled semiconductor quantum dots*, *Phys. Rev. B* **67**, 195301 (2003).

[47] M. Meixner and E. Schöll, *Kinetically enhanced correlation and anticorrelation effects in self-organized quantum dot stacks*, *Phys. Rev. B* **67**, 121202 (2003).

[48] F. Elsholz, M. Meixner, and E. Schöll, *Kinetic Monte Carlo simulation of self-organized pattern formation in thin film deposition*, *Nucl. Instruments and Methods B* **202C**, 249 (2003).

[49] M. Block, R. Kunert, E. Schöll, T. Boeck, and Th. Teubner, *Kinetic Monte Carlo simulation of formation of microstructures in liquid droplets*, *New Journal of Physics* **6**, 166 (2004).

[50] M. Block and E. Schöll, *Time delayed feedback control in growth phenomena*, *J. Crystal Growth* **303**, 30 (2007).

[51] M. Block, B. Schmittmann, and E. Schöll, *Controlling surface morphologies by time-delayed feedback*, *Phys. Rev. B* **75** (2007).

[52] F. Elsholz and E. Schöll, *Kinetic Monte Carlo simulations of amorphous thin-film growth*, *phys. stat. sol. (b)* **244**, 3639 (2007).

[53] M. Block, E. Schöll, and D. Drasdo, *Classifying the expansion kinetics and critical surface dynamics of growing cell populations*, *Phys. Rev. Lett.* , in print (2007).

[54] B. J. Alder and T. E. Wainwright, *Phase Transition for a Hard-sphere System*, *J. Chem. Phys* **27**, pp. 1208 (1957).

[55] A. R. Leach, *Molecular Modelling*, *Pearson Prentice Hall, 2nd Edition* (2001).

[56] W. D. Cornell, P. Cieplak, C. I. Bayly, I. R. Gould, K. M. Merz Jr, D. M. Ferguson, D. C. Spellmeyer, T. Fox, J. W. Caldwell, and P. A. Kollman, *A Second Generation Force Field for the Simulation of Proteins, Nucleic Acids and Organic Molecules*, *J. Am. Chem. Soc.* **117**, pp. 5179 (1995).

[57] P. C. Tsiartas, L. W. Flanagin, C. L. Henderson, W. D. Hinsberg, I. C. Sanchez, R. T. Bonnecaze, and C. G. Willson, *The Mechanism of Phenolic Polymer Dissolution: A New Perspective*, *Macromolecules* **30**, 16 (1997).

[58] G. M. Schmid, V. K. Singh, L. W. Flanagin, M. D. Stewart, S. D. Burns, and C. G. Willson, *Recent advances in molecular level lithography*, *Proc. SPIE* **3999**, pp. 675 (2000).

[59] S. D. Burns, G. M. Schmid, P. C. Tsiartas, and C. G. Willson, *Advancements to the Critical Ionization Dissolution Model*, *J. Vac. Sci. Technol. B* **20**, 2 (2002).

[60] G. M. Schmid, M. D. Stewart, S. D. Burns, and C. G. Willson, *Mesoscale Monte Carlo Simulation of Photoresist Processing*, *J. Electrochem. Soc.* **151**, 2 (2003).

[61] T. Yoshimura, H. Shiraishi, J. Yamamoto, and S. Okazaki, *Correlation of Nano Edge Roughness in Resist Patterns with Base Polymers*, *Jpn. J. Appl. Phys.* **32**, 6065 (1993).

[62] Y. Ma, J. Shin, and F. Cerrina, *Line Edge Roughness and Photoresist Percolation Development Model*, *J. Vac. Sci. Technol. B* **21**, 1 (2003).

[63] L. E. Ocola, *Soluable site density model for negative and positive resists*, *J. Vac. Sci. Technol. B* **21**, 1 (2003).

[64] L. E. Ocola, P. A. Orphanos, W.-Y. Li, W. Waskiewicz, A. E. Novembre, and M. Sato, *Roughness study of a positive tone high performance SCALPEL resist*, *J. Vac. Sci. Technol. B* **18**, 6 (2000).

[65] G. M. Gallatin, *Resist blur and line edge roughness*, *Proc. SPIE* **5754**, 38 (2005).

[66] V. Constandoudis, E. Gogolides, G.P. Patsis, A. Tserepi, and E.S. Valamontes, *Characterization and simulation of surface and line-edge roughness in photoresists*, *J. Vac. Sci. Technol. B* **19 (6)**, 2694 (2001).

[67] G.P. Patsis and E. Gogolides, *Simulation of Surface and Line-Edge Roughness Formation in Resists*, *Micoel. Eng.* **57**, pp. 563 (2001).

[68] G.P. Patsis and E. Gogolides, *Material and process effects on line-edge-roughness of photoresists probed with a fast stochastic lithography simulator*, *J. Vac. Sci. Technol. B* **23 (4)**, 1371 (2005).

[69] T. Schnattinger, E. Bär, and A. Erdmann, *Three-dimensional Resist Development Simulation with Discrete Models*, *J. Vac. Sci. Technol. B* **24**, 6 (2006).

[70] T. Schnattinger, *Mesocopic simulation of photoresist processing in optical lithography*, *PhD thesis* , FAU Erlangen (2007).

[71] G. W. Reynolds and J. W. Taylor, *Factors contributing to sidewall roughness in a positive-tone, chemically amplified resist exposed by x-ray lithography*, *J. Vac. Sci. Technol. B* **17**, 334 (1999).

[72] A. R. Pawloski, A. Alcheta, H. J. Levinson, T. B. Michaelson, A. Jamieson, Y. Nishimura, and C. G. Willson, *Line Edge Roughness and Intrinsic Bias for two Methacrylate Polymer Resist Systems*, *J. Microlith. Microfab. Microsyst.* **5**, 023001 (2006).

[73] D. Van Steenwinckel, J. H. Lammers, T. Koehler, R. L. Brainard, and P. Trefonas, *Resist effects at small pitches*, *J. Vac. Sci. Technol. B* **24**, 316 (2006).

[74] P.M. Dentinger, L.L. Hunter, D.J. O'Connell, S. Gunn, D. Goods, T.H. Fedynyshyn, R.B. Goodman, and D.K. Astolfi, *Photospeed considerations for extreme ultraviolet lithography resists*, *J. Vac. Sci Tech. B* **20 (6)**, 2962 (2002).

[75] M. Yoshizawa and S. Moriya, *Study of the acid-diffusion effect on line edge roughness using the edge roughness evaluation method*, *J. Vac. Sci. Technol. B* **20**, 1342 (2002).

[76] M. Yoshizawa and S. Moriya, *Comparative study of resolution limiting factors in electron beam lithography using the edge roughness evaluation method*, *J. Vac. Sci. Technol. B* **19**, 6 (2001).

[77] I. M. Mitchell and J. A. Templeton, *A Toolbox of Hamilton-Jacobi Solvers for Analysis of Nondeterministic Continuous and Hybrid Systems*, *Springer Lecture Notes in Computer Science (LNCS)* **3414**, pp. 480 (2005).

[78] R. Kool, C. Wagner, and R. Garreis, *Stepping and scanning into the Na > 1 immersion exposure era*, *Solid State Technology* **48**, 8 (2005).

[79] T.B. Chiou, A.C. Chen, S.E. Tseng, M. Eurlings, E. Hendrickx, and S. Hsu, *The magnitude of potential exposure-tool-induced critical dimension and overlay errors in double dipole lithography for the 65-nm and 45-nm technology nodes*, *Jpn. J. Appl. Phys.* **43**, 6B (2004).

[80] A. Philippou, T. Mülders, and E. Schöll, *Impact of photoresist composition and polymer chain length on line edge roughness probed with a stochastic simulator*, *J. Micro/Nanolith. MEMS MOEMS* **to be published** (2007).

[81] K. Hinsen, *The molecular modeling toolkit: A new approach to molecular simulations*, *J. Comp. Chem.* **21(2)**, 79 (2000).

[82] W. D. Hinsberg F. A. Houle and M. I. Sanchez, *Kinetic Model for Positive Tone Resist Dissolution and Roughening*, *Macromolecules* , 8591 (2002).

[83] A. Dalke W. Humphrey and K. Schulten, *VMD - Visual Molecular Dynamics*, *J. Molec. Graphics* **14**, 33 (1996).

[84] T. Mülders, W. Henke, K. Elian, C. Nölscher, and M. Sebald, *New Stochastic Post-exposure Bake Simulation Method*, *J. Microlith. Microfab. Microsyst.* **4**, 043010 (2005).

[85] J. Elf, A. Doncic, and M. Ehrenberg, *Mesoscopic reaction-diffusion in intracellular signaling*, *Proc. of the SPIE's First International Symposium on Fluctuations and Noise* (2003).

[86] J. Schnakenberg, *Algorithmen in der Quantentheorie und Statistischen Physik*, *Verlag Zimmermann-Neufang* (1995).

[87] C. W. Gardiner, *Handbook of stochastic methods*, *Springer, 2nd Edition* (1985).

[88] N. G. Van Kampen, *Stochastic processes in physics and chemistry*, *North Holland, 3rd Edition* (2007).

[89] H. Meiling, R. Groeneveld, H. Meijer, U. Mickan, H. J. Voorma, N. Harned, and J. Zimmerman, *Progress in the realisation of EUV lithography*, *EUV Symposium, Barcelona* (2006).

[90] F. Elsholz, E. Schöll, and A. Rosenfeld, *Control of surface roughness in amorphous thin film growth*, *Appl. Phys. Lett.* **84**, 4167 (2004).

[91] F. Elsholz, E. Schöll, C. Scharfenorth, G. Seewald, H. J. Eichler, and A. Rosenfeld, *Roughness evolution in thin film growth of SiO_2 and Nb_2O_5*, *J. Appl. Phys.* **98**, 103516 (2005).

[92] G. P. Patsis, V. Constantoudis, and E. Gogolides, *Effects of photoresist polymer molecular weight on line-edge roughness and its metrology probed with Monte Carlo simulations*, *Microel. Eng.* **75**, 297 (2004).

[93] M. Ercken, L. H. A. Leunissen, I. Pollentier, G. P. Patsis, V. Constantoudis, and E. Gogolides, *Effects of different processing conditions on line edge roughness for 193nm and 157nm resists*, *Proc. SPIE* **5375**, 266 (2004).

[94] J.M.J. Fréchet, F. Bouchard, E. Eichler, F.M. Houlihan, T. Iizawa, B. Kryczka, and C.G. Willson, *Thermally Depolymerizable Polycarbonates V. Acid Catalyzed Thermolysis of Allylic and Benzylic Polycarbonates: A New Route to Resist Imaging*, *Polym. J.* **19**, 31 (1987).

[95] C. Eschbaumer, N. Heusinger, M. Kern, A. Jutgla, C. Hohle, and M. Sebald, *Chemically amplified Main Chain Scission: Chopping the influence of polymer dimensions on line edge roughness*, *J. Photo. Sci. Tech.* **16**, 13 (2003).

[96] H. A. Stone and D. Margetis, *Continuum Descriptions of Crystal Surface Evolution*, *Handbook of Materials Modelling* **1**, 1 (2005).

[97] H. Spohn, *Surface Dynamics Below the Roughening Transition*, *J. Phys. I France* **3**, 69 (1993).

[98] J. A. Forrest, C. Svanberg, K. Revesz, M. Rodahl, L. M. Torell, and B. Kasemo, *Relaxation Dynamics in Ultrathin Polymer Films*, *Phys. Rev. E* **58**, R1226 (1998).

[99] A. Adalsteinsson and J. A. Sethian, *A fast level set method for propagating interfaces*, *J. Comp. Phys.* **118**, 2 (1995).

[100] Y. C. Chang, T. Y. Hou, B. Merriman, and S. J. Osher, *A level set formulation of eulerian interface capturing methods for incompressible fluid flow*, *Jour. Comp. Phys.* **124**, pp. 370 (1996).

List of Figures